

Nuclear excitation functions for medical isotope production:  
Targeted radionuclide therapy via natIr(d,2n)<sup>193m</sup>Pt

Hannah Lovise Okstad Ekeberg

June 2020



# Contents

<b>1 Abstract</b>	<b>5</b>
<b>2 Targeted radionuclide therapy</b>	<b>7</b>
2.1 Particle interaction in tissue . . . . .	9
2.2 Production of radionuclides . . . . .	13
2.3 $^{193m}\text{Pt}$ as a potential therapeutic agent . . . . .	13
<b>3 General nuclear reaction theory</b>	<b>17</b>
3.1 Nuclear reactions and reaction cross sections . . . . .	17
3.1.1 Constraints in nuclear reactions . . . . .	19
3.2 Nuclear reaction models . . . . .	22
<b>4 Experimental setup</b>	<b>23</b>
4.1 The stacked target activation method . . . . .	23
4.2 Characterization of the target foils . . . . .	24
4.3 Lawrence Berkeley National Laboratory's 88" Cyclotron . . . . .	25
4.4 High purity Gerganium detector . . . . .	27
4.4.1 Obtaining a spectrum . . . . .	28
4.4.2 Turning the number of counts in a gamma-ray peak to an activity . . . . .	30
4.4.3 Energy and peakshape calibration . . . . .	31
4.4.4 Efficiency calibration . . . . .	31
4.5 The irradiation . . . . .	33
<b>5 Analysis</b>	<b>45</b>
5.1 Analyzing the gamma-ray spectra . . . . .	45
5.1.1 Background subtraction . . . . .	47
5.2 Estimating the end of beam activities . . . . .	48
5.3 Monitor reactions . . . . .	49
5.4 Deuteron beam current and energy assignment . . . . .	53
5.4.1 Variance minimization for the deuteron energy assignments . . . . .	54
5.5 Cross sections . . . . .	62
<b>A Statistics</b>	<b>63</b>
<b>B Tables</b>	<b>65</b>
B.1 Product nuclei, Q-values and gammarays . . . . .	65
B.2 Production cross sections . . . . .	72
B.2.1 $^{nat}\text{Ir}(d,x)$ . . . . .	72

## CONTENTS

---

# Chapter 1

## Abstract

In this thesis work, a stack of ten natural irridium (99.9%) foils were irradiated with a 33 MeV incident deuteron beam at the Lawrence Berkeley National Laboratory's 88-Inch Cyclotron, yielding ten cross section measurements from ca. 5 to 30 MeV in the activated foils as the energy decreases as the deuterons traverses through the foils. The motivation behind this experiment was to measure the  $^{nat}Ir(d,x)$  reactions which have lack of data..., with a special emphasis on finding the energy-window inwhich optimizes the production of the auger-emitting radionuclide  $^{193m}Pt$  which can have potential in targeted radionuclide therapy. In addition, ten monitor foils of nickel, copper and iron were placed within each compartment of irridium, to measure the deuteron current in each compartment, via the well-characterized monitor reactions  $^{nat}Ni(d,x)^{61}Cu$ ,  $^{56,58}Co$ ,  $^t ext{nat}Cu(d,x)^{62,63,65}Zn$  and  $^{nat}Fe(d,x)^{56}Co$ .

The cross sections were estimated using the analogy to the activation equation for thin targets,  $A_0 = N_T \cdot \Phi(E_d)\sigma(E_d)(1 - e^{-\lambda t_{irr}})$ , where the energy of the deuteron beam was weighted-averaged over each foil. Prior to radiation, the number of target nuclei of each foil was characterized measuring the length across each foil and the mass. The deuteron-induced activity in each foil as a function of time since end of beam was obtained using gamma-ray spectroscopy on pre-calibrated high purity germanium detectors. The measured activities were fitted to decay curves to find the activity at the end of beam. Along with the weighted averaged beam current estimated from the monitor reactions, the flux weighted cross sections were estimated. This work along with previous experimental data suggests an energywindow from ca. 11 to 15 MeV which maximises the production of  $^{193m}Pt$ . The highest measured cross section in this work was  $148.98 \pm 5.54$  mb at 13.51 MeV. For irridium, the independent measurements of  $^{188,190m2,194m2}Ir$  and  $^{188,189,191,193m}Pt$ , and the cumulative cross sections  $^{188,189,190,192,194}Ir$  are reported. From the monitor foils, the first observed measurements of cumulative cross sections of  $^{61}Co$  from copper, cumulative cross sections of  $^{48}V$ ,  $^{51}Cr$ ,  $^{53}Fe$  from iron, the cumualative cross sections of  $^{59}Fe$  and the independent cross sections of  $^{56,57,57}Co$  are also reported in this work, along with the other products produced. The results are compared to experimental data from the EXFOR database, along with the nuclear reaction modelling codes TALYS, TENDL, CoH, ALICE and **EMPIRE**, using the default parameters to aid improvements of the codes, **which did not match the experimental data very well in general, in particular in magnitude.**



## Chapter 2

# Targeted radionuclide therapy

Today, multiple options for treatment of cancerous tissue are available, such as chemotherapy, surgery, immunotherapy, external beam therapy, brachytherapy and targeted radionuclide therapy. The latter three are treatment types utilizing ionizing particles to induce damage to the DNA. In external beam therapy X-rays, high-energetic gamma-rays, or accelerated particles like protons and heavier ions are focused externally towards the tumor, and in brachytherapy an unsealed radioactive source (usually a wire or pellet containing for instance a  $\beta^-$ -emitter), is placed in proximity to tumor ([1], p.2180). Targeted radionuclide therapy is an emerging alternative, which can deliver a cytotoxic level of dose to the site of disease ([1], p. 2180). It offers a patient-specific treatment dependent on choice of radiopharmaceutical which targets a type of tumor or cell. A radiopharmaceutical consists of a radionuclide and a cell-targeting molecule called a tracer. Meanwhile brachytherapy and targeted radionuclide therapy are limited by the cancer location and the existence of metastasis, along with required knowledge of the tumor to maximise the dose over the tumor and minimizing the dose to healthy tissue ([1], p.2180), targeted radionuclide therapy utilizes radiopharmaceuticals which are typically injected intravenously and utilized the biochemical pathways in the body. thus with an appropriate tracer, targeted tissue with a high uptake of the radiopharmaceutical will receive a high dose, and healthy tissue can be spared [2].

A therapeutic agent needs to have the two components of the radiopharmaceutical optimized for the radiation from the radionuclide to have a high probability of being deposited in the tumor, and ideally deliver a cytotoxic dose to all cancerous cells within a tumor while sparing all healthy cells. For instance, a high uptake-rate of the tracer suggests a shorter half-life of the radionuclide than slow uptake and long retention in tumor. The decay mode and radiation range need to be in coherence with the size and location, as well as the geometry of the tumor. Ranges from multi-cellular, cellular and sub-cellular are typically accomplished with  $\beta^-$ -particles,  $\alpha$ -particles and auger electrons, respectively ([1] p. 2180-2182). Figure 2.1 shows how the ranges of  $\beta^-$ ,  $\alpha$  and auger electrons differ on the cellular scale, where low energetic auger electrons have ranges on the scale of the cellular nucleus, while high energetic  $\beta^-$ -particles have ranges of up to several hundred cell diameters.

For the tracer, properties such as a rapid blood clearance and transport ([4] p. 145) and high uptake and retention in the tumor [3] p. 2) are important characteristics, along with tissue-targeting [2]. It can target the desired cells by for instance a specific receptor, enzyme, membrane, transporters or antigens ([4], p. 145). Radiometals are also used, which consists of a bifunctional chelator, which is a molecule containing molecules which can donate a lone pair of electrons, like nitrogen, oxygen or sulfur. If the radiometal has an oxidation state of  $3^+$ , it will be tightly bound by the chelator, and can be transported to the tumor [5]. Figure 2.2 shows an illustration of how an example of how a radionuclide can be transported into the desired cell attached to a chelator, via a specific peptide.

For the radionuclide, along with range and decay mode, the half-life, production method, chemistry and biological behavior are important characteristics ([1], p. 2181).

In nuclear medicine, the effective half-life of the radiopharmaceutical is important as it takes both

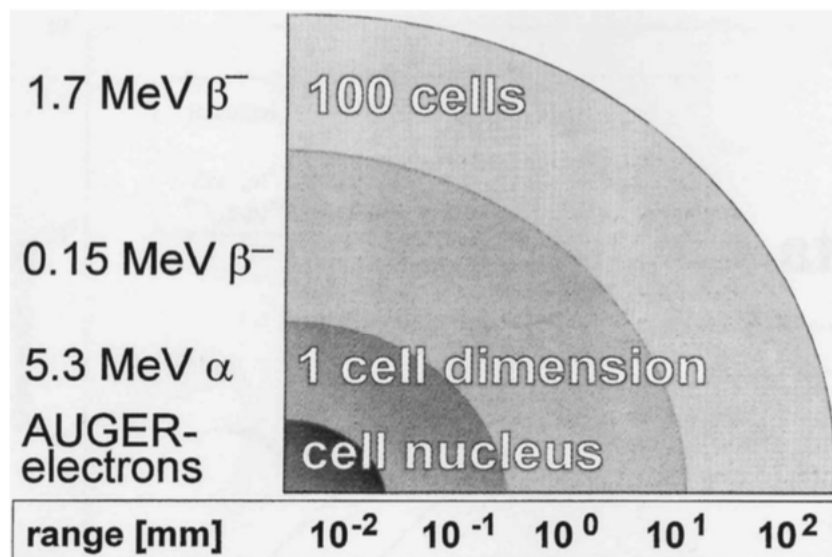


Figure 2.1: The figure illustrates the ranges of auger electrons, 5.3 MeV alpha particles and low and high energetic  $\beta^-$  particles. Figure is from [3], p. 2

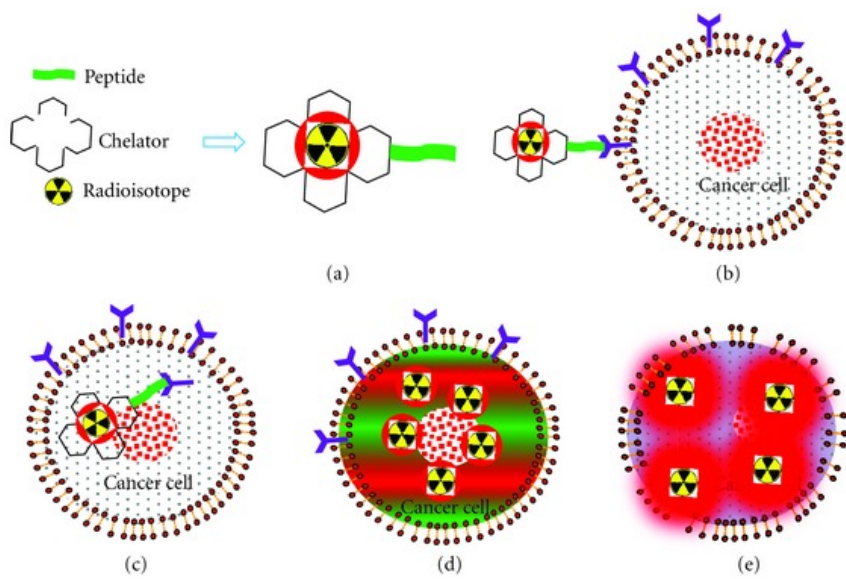


Figure 2.2: A radionuclide is bound to a chelating agent, and with a peptide, the radiopharmaceutical targets the cancer cells. Figure is from [6].

the physical half-life and the time it takes for the radiopharmaceutical to be cleared or excreted from the body [2]. The physical half-life must be long enough to permit radiosynthesis and quality control ([1], p. 2185). However, in therapy, high radiation dose is desired, which is easier to achieve with shorter half life, so that should also be compensated for. The choice of radionuclide should match the uptake rate and the retention of the cell-targeting molecule, to avoid radioactive waste handling and dose to healthy tissue [2]. Therapeutic radionuclides typically have half-lives in order of a few hours to several days ([3], p. 1). In addition, knowledge about the decay product is important, for instance whether it is toxic or if it takes place in natural processes in the body, or if contributes to an additional undesired dose. The chemical-biological properties are also relevant, as it must be chemically possible to attach radionuclide to the targeting molecule, and the binding must stay stable in the body, over a time period which is stable as long as the physical half life ([1], p. 2185).

Along with the ability to use radionuclides in therapy, radionuclides can also be used for diagnostic purposes with imaging, either with positron emitters (positron emission tomography) in which annihilates with atomic electrons close to the site of decay, and sends out two observable 511 keV photons, or emission of a strongly fed gamma-energy which is detected (single photon emission tomography). The combination of a diagnostic and a therapeutic agents with similar properties so that the biochemical uptake in the body is the same, is a new approach in which can give information of how the uptake is distributed in the body, and can image the state of disease after therapies [7]. This is called theranostics.

## 2.1 Particle interaction in tissue

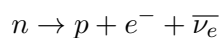
Ionizing radiation are particles with sufficient energy to cause ionizations along the particle track, thus separating an atom and one or more electrons. The free electron(s) can ionize further, and the positive ion can cause undesired reactions. DNA is a large molecule with two strands bound in a double helix structure. Each strand is composed of sugar and phosphate groups, and nitrogenous bases which bind the two strands ([8] p. 11). These bases are called adenine & guanine and cytosine & thymine (always bound pairwise), and are bound through weak hydrogen bonds which are exposed for strand breaks. The cell is equipped with an impressive repair mechanism, and unless both strands of the DNA are damaged, called a double stranded break (DSB), most damages are repaired. Radiation damages in the DNA can be caused directly by the ionizing particle or indirectly via free radicals, which are subject to other ionizations. Since the body contains large amounts of water, ionization of water molecules giving for instance  $H^\bullet$  or  $OH^\bullet$  are important damaging factors. Damages induced in the DNA can be lethal to the cell and either cause apoptosis or mutation in which can cause cancer. In therapy, the goal is to make malignant cells to undergo apoptosis, thus DNA is referred to as the target ([8], p. 9). Choosing a particle with a high probability of inducing damage will induce multiple double stranded breaks if passing near by.

Linear energy transfer (LET) describes the energy absorbed by the medium, and is defined as the average energy deposited per unit length of the density material ([8], p. 101).

$$\text{LET} = \frac{dE}{dx} \quad (2.1)$$

To maximise the chances of inducing damages in the DNA and minimizing exposure of healthy tissue, choosing a particle with a high linear energy transfer is important in targeted radionuclide therapy. Figure 2.3 illustrates how  $\beta^-$ -particles, alpha-particles and auger electrons deposit energy on the scale of DNA.

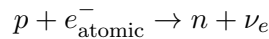
$\beta$ -decay occurs whenever there is an overweight in number of neutrons/protons, where the former transforms a neutron into an electron, proton and an antineutrino ( $\beta^-$ -decay):



The contrary  $\beta^+$  decay transforms a proton into a positron, neutron and a neutrino ( $\beta^+$ -decay):



Since the neutron mass is higher than proton mass with  $2m_e \text{ MeV}/c^2$ , there is an energy threshold for the reaction to occur. If the reaction is below the energy threshold, electron capture occurs instead, which is an electromagnetic interaction between an atomic electron (creating a vacancy in the atomic shells) and a nuclear proton that transform into a neutron and a neutrino



For  $\beta$ -decay, the energy is distributed between three particles, thus the energy of the  $\beta$ -particle is not discrete.

$\alpha$ -decay occurs when the nuclear radius is so large that it is affected by the Coulomb barrier. Thus emission of an alpha particle lowers the binding energy as the alpha particle carries a large amount of binding energy. The  $\alpha$ -energy are discrete values which can be detected using spectroscopy.

Auger electrons are result from electron capture or internal conversion, which happens when a gamma-ray interacts electromagnetically with an atomic electron which is emitted. The vacancy in the atomic shell can lead to a cascade of X-rays and auger electrons with energies in the X-ray range. These energies are discrete, as the X-ray energy is discrete. From  $\beta$  and sometimes  $\alpha$  decay, the daughter nucleus is left in an excited state and decays by gamma-emission (all from special curriculum [5]) [9] (chapters 8,9,10).

A medium consists of positively charged nuclei and negatively charged electrons. Charged particles have a short range in a medium compared to neutral particles, as the Coulomb force forces the particle to interact continuously along the path either by scattering inelastic with the atomic electrons or scattering elastic with the nuclei. Figure 2.4 shows how various particles such as X-rays, gamma-rays, electrons and protons deposit energy (y-axis) as a function of depth. Elastic scattering is the less dominant process, where the energy loss is small, as long as the nuclei in the medium are larger than the incoming particle [10], p. 21. **Inelastic collisions dominates where the atomic electrons are either excited or ionized (which citation???? Instrumentation book?).** Under the assumption that the collision is elastic, the collision is head-on and the particle has high energy, the maximum energy transfer can be calculated using conservation of momentum and energy

$$Q_{\max} = \frac{4m_e M}{m + M} E \quad (2.2)$$

where  $m_e$  is the mass of an atomic electron,  $M$  is the mass of the incoming charged particle and  $E$  is the kinetic energy of the incoming charged particle <sup>1</sup>. While LET describes the energy transferred per unit length, the stopping power describes the energy loss of a charged particle per unit distance. The collision loss for heavy charged particles (protons and heavier ions) at high energies is therefore low. The stopping power for heavy charged particles is described by Bethe-Block:

$$-\frac{dE}{dx} = 2\pi N_a r_e^2 m_e c^2 \rho \frac{Z}{A} \frac{z^2}{\beta^2} \left[ \ln \left( \frac{2m_e \gamma^2 v^2 W_{\max}}{I^2} \right) - 2\beta^2 - \delta - 2\frac{C}{Z} \right] \quad (2.3)$$

where

$r_e$  : classical electron radius

$m_e$  : electron mass

$N_a$  : Avogadro's number

$I$  : mean excitation energy

$Z$  : atomic number of absorbing material

$A$  : atomic weight of absorbing material

$\rho$  : density of absorbing material

$z$  : charge of incident particle

$\delta$  : density correction

$C$  : shell correction

$W_{\max}$  : maximum energy transfer in each collision

$\beta = v/c$  : incident velocity of the particle

$\gamma = \frac{1}{\sqrt{1-\beta^2}}$  : Lorentz factor

<sup>1</sup>To see calculation , see: <https://ocw.mit.edu/courses/nuclear-engineering/22-55j-principles-of-radiation-interactions-fall-2004/lecture-notes/energydeposhcp.pdf>

( [10], p. 24)

As the particle slows down, the more energy per unit length will be deposited, as the charged particle picks up electrons. This is known as the Bragg peak, which can be seen as the red curve on figure 2.4. Most of the energy is deposited near the end stop. The stopping power of heavy charged particles are proportional to the charge of particle and the inverse velocity squared. Therefor, particles with a higher charge will have a higher more specific Bragg-peak and a shorter range in tissue, with the same initial energy. This behaviour of heavy charged particles is especially useful in external beam therapy and is utilized to have a very specific dose over tumor as the dose before is low and the dose after Bragg peak is approximately zero ( [10], p. 27-28). In addition, to increase the width of the Bragg peak, a spread-out Bragg-peak is obtained by accelerating the particle in a spectrum of energies, which is the blue curve on figure 2.4.

Electrons can experience energy loss either from collisions, or via the electromagnetic radiation that arises when electrons are loosing energy (bremsstrahlung), due to the small mass. However, for energies up to a few MeV, the collision energy loss dominates ( [10], p. 37). For electrons, the maximum energy transfer per collision is half of the initial energy, which means that electrons lose energy fast via collisions. Electrons scatters rapidly, and changes direction continuously due to the equal mass of the atomic electrons. The energy loss of electrons fluctuates much more than heavy charged particles which is due to much greater energy transfer per collision and to the emission of bremsstrahlung. To absorb major part of the electron's energy, is a few collisions, and results in greater range straggling. ( [10] p. 42). From figure 2.4, the 22 MeV electrons are loses energy exponentially, **due to bremsstrahlung??**

Photons and neutrons however are neutral particles and are not energy-degraded. Instead neutral particles are attenuated as a function of distance traversed  $x$  and the absorption coefficient  $\mu$  of the material

$$I = I_0 e^{-\mu x} \quad (2.4)$$

where  $I$  is the intensity as a function of distance and  $I_0$  is the intensity at  $x=0$  ( [10], p. 53). X-rays produced from a X-ray tube and gamma-rays degrades exponentially, and are thus more penetrating than charged particles. As gamma-emitters are not directly used in targeted radionuclide therapy, the dose from gamma-radiation following alpha or beta decay, or X-rays following electron capture or internal conversion needs to be taken into account.

For high energetic X-rays there is a build up effect, where the photons induce ionizations, and the free electrons contribute to a higher dose. This can be seen for the 22 MV X-rays in figure 2.4. This is utilized in external beam therapy, maximizing the dose over the tumor. For gamma-rays, the energy is not sufficiently high, so instead the curve follows an exponential form as the dotted line in figure 2.4.

In general,  $\beta^-$ -particles have relatively low LET and are thus suited for treating large tumors, but the dose to healthy tissue may be hard to avoid.  $\alpha$ -particles have short range in tissue, typically one to a few cells in diameter. Has a high LET-value, radiation with  $LET=100 \text{ keV}/\mu\text{m}$  has the distance between ionizing events is nearly identical to that between DNA strands increasing the probability of creating highly cytotoxic double strand breaks [1], chapter "Targeted radionuclide therapy". One of the major problems with  $\alpha$ -emitters is the decay products, as a typical  $\alpha$ -decay chain results in multiple emission of  $\alpha$  and  $\beta$ -particles. For low energetic electron emitters such as auger emitters, the range is so low that in order to deposit energy in the DNA, it must be incorporated into the cellular nucleus. Thus, it will only affect the cell targeted, and as we can see in figure 2.3 when incorporated into DNA, can induce many damages in the DNA.

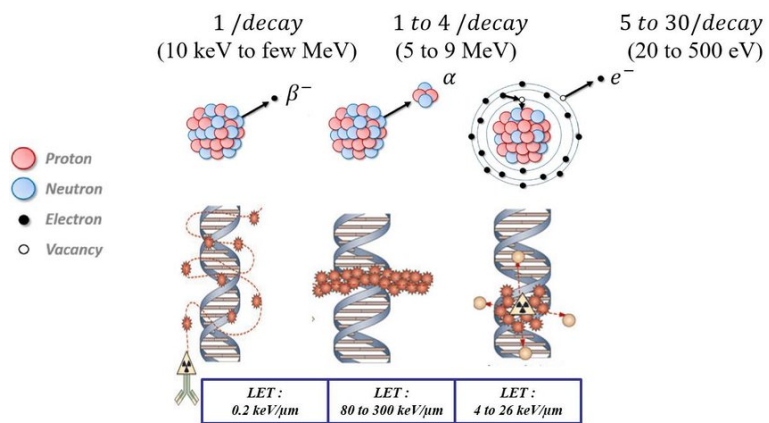


Figure 2.3: The figure illustrates how  $\beta^-$ -particles,  $\alpha$ -particles and auger electrons deposit their energy on the scale of DNA. The figure is assembled from [11], where the upper figure is from [12], and the lower figure is from [13].

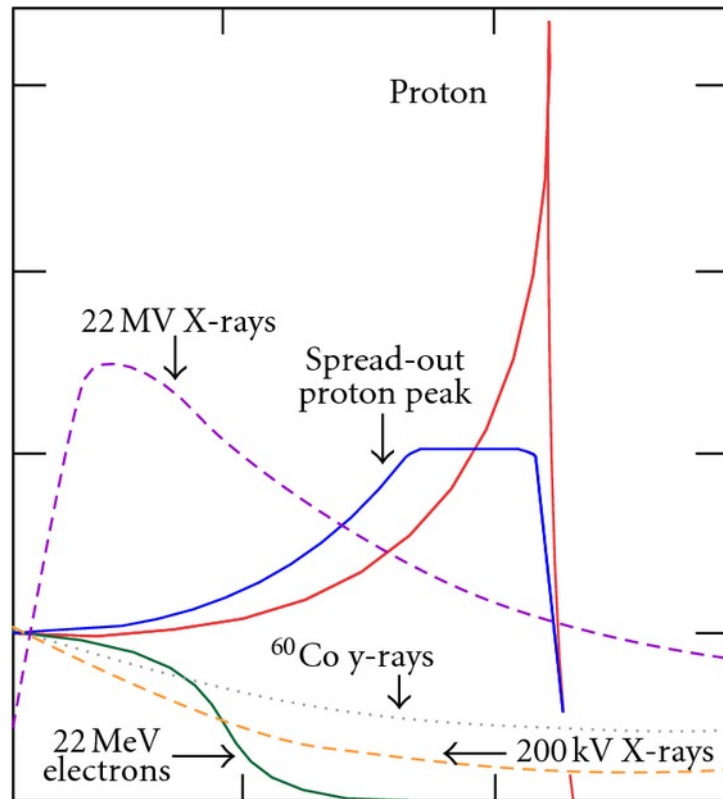


Figure 2.4: Medium depth along x-axis, energy deposition in tissue (or dose?) on y-axis. The figure is from [14].

## 2.2 Production of radionuclides

The radionuclide availability is an important factor in targeted radionuclide therapy. Reactors, cyclotrons and natural decay chains have traditionally been used as radionuclide sources [1], p. 2185. Proton rich nuclei are typically produced in accelerators/cyclotrons using positively charged particles, and neutron rich nuclei are typically products of fission or produced in the neutron flux resulting from fission in a reactor. Thus therapeutic radionuclides producing  $\beta^-$ -emitters need neutrons, which are the main source of reactors. With research reactors today aging [2], alternative production routes to produce critically medical radionuclides are important.

There are many different production routes available for a single radionuclide, dependent on choice of target, particle beam and beam energy. The production route has an associated reaction cross section which is dependent on the beam energy. The nuclear cross section data is very important in optimization of production processes, achieving the maximum yield of the desired radionuclide combined with the minimum level of radionuclidic impurities [3]. A high degree of radionuclidic purity is required for therapeutic radiopharmaceuticals depending on the nature of the molecule that will be labelled, specific activity (GBq/mmol) may also be important consideration. It is impossible to chemically separate isotopes of the same element [15]. We want to be sure that what is injected into the patient does not have isotopic impurities which gives undesired dose to the tissue, nor will we have isotopes with no therapeutic effect. This is to yield effective treatment, but especially in cases where the body does not excrete the element from the body, the result can lead to toxicity effects. Carrier-free production which are molecules which exclusively contain the desired radionuclides is desired because it gives the highest specific activity. The only option to minimize impurities is to choose an appropriate energy window which minimizes the production of co-products. There already exists large amounts of information on neutron induced reactions. However the information on charged particle induced reactions is not as strong so we need more data on this behalf [15]. Production of medical radionuclides should be cheap and available for everyday medical purposes. Accelerators can be small in size and handled easily by medical personnel. Many hospitals which performs nuclear medicine even have a cyclotron facility on site, which is advantageous as its practical to avoid travelling logistics and to have medical radionuclide supply in proximity of examination/treatment site [5].

## 2.3 $^{193m}$ Pt as a potential therapeutic agent

$^{193m}$ Pt ( $t_{1/2}=4.33$  days) is an auger-emitting isomer which decays by isomeric transition (100%) to the long-lived  $^{193g}$ Pt groundstate ( $t_{1/2}=50$  years) [16]. Radionuclides produced from deuterons on natural iridium such as  $^{191}$ Pt,  $^{193m}$ Pt,  $^{192}$ Ir and  $^{194}$ Ir are believed to have potential in medicine, like chemotherapy, brachytherapy, radioimmunotherapy and imaging [17]. Platinum radionuclides are of special interest, as platinum is the main element in chemotherapeutic agents such as cisplatin, which is a drug which is used clinically in treatment of testicular and ovarian cancer mainly, but also to treat esophagus, head and neck and bladder cancer [18]. Cisplatin (cis-dichlorodiammine platinum(II)) is an inorganic molecule which contains one stable platinum atom surrounded by two chlorine atoms and two ammonia molecules ( $\text{NH}_3$ ). The cisplatin-molecule enters the cell nucleus, and binds to the DNA, example-wise shown in figure 2.6, where the chlorine-atoms are de-attached and the platinum-atom binds through covalent bonds to the DNA base guanine (and in some cases adenine, **is that correct?**), and breaks the bonds between the DNA nitrogenous bases. Cisplatin thus targets the DNA. One of the major challenges with cisplatin is the chemical toxicity. However, when auger-emitters such as  $^{193m}$ Pt or  $^{195m}$ Pt replace the stable platinum atom, the local auger-damage effect increases the chemical damage of cisplatin, suggesting that a smaller amount of the drug is required, and the toxicity-limitations can be avoided [19] p. 493.

As  $^{191}$ Pt is an electron-capture emitter, can be used in imaging, with for instance 129.4 keV (38.0%) or 172.19 keV (43.2%). Combining  $^{191}$ Pt with a therapeutic agent might be possible for theranostic pair with either  $^{193m}$ Pt or  $^{195m}$ Pt? Can be combined with therapy as it releases auger electrons?

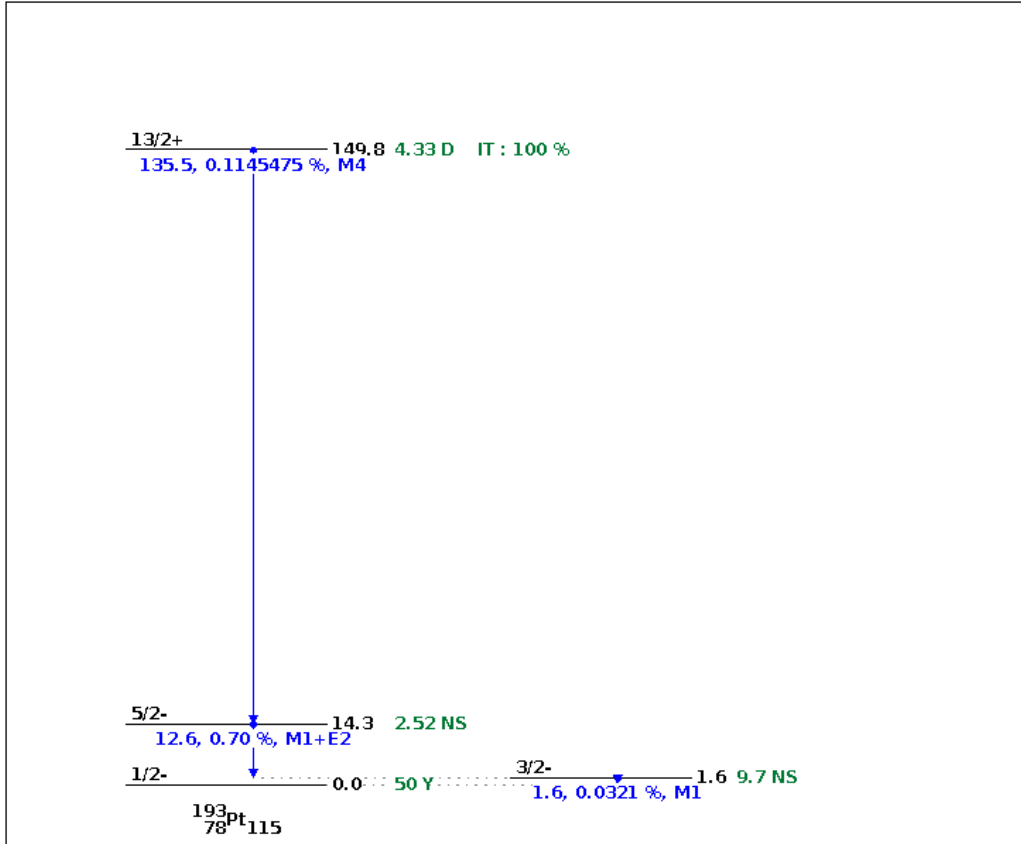


Figure 2.5: The decay scheme of  $^{193m}Pt$ . From (<https://www.nndc.bnl.gov/nudat2/replotdec.jsp>). Figure from Nudat 2.8 database [20].

Gamma-decay is a result of de-excitation of a nucleus with the release of a photon equal to the energy difference between the two states. The typical half-life of a populated excited state is less than  $10^{-9}$  seconds, and states with longer half-lives are called isomeric states ([9] p. 175). This isomer decays by isomeric transition. In all decays, there are certain quantities which needs to be conserved; angular momentum, parity. A multipole of order  $\ell$  transfers angular momentum  $\ell\hbar$  per photon ([9] p.333). A nuclear state has a definite angular momentum  $\ell$  (ang mom + spin?) and parity, and if a gamma transition is to happen between two states the photon must connect the two states by conserving angular momentum and parity. In order for the quantity  $\ell$  to be conserved, the angular momentum can be integers between

$$|I_i - I_f| \leq \ell \neq I_i + I_f \quad (2.5)$$

where i is initial spin and f is final spin. I is the total spin (angular momentum and spin). The parity decides whether the radiation is electric multipole or magnetic multipole (equations [9] p.311)

$$\pi(ML) = (-1)^{\ell+1}, \quad \pi(EL) = (-1)^\ell \quad (2.6)$$

There are three populated states for this nuclide, the isomer state at 149.8 keV, with nuclear spin  $13/2^+$  (4.33 d), a state at 14.3 keV with nuclear spin  $5/2^-$  (2.52 ns), a state at 1.6 keV with nuclear spin  $3/2^-$  (9.7 ns) and the ground state at 0.0 keV with nuclear spin  $1/2^-$  (50 y) [16]. The decay scheme can be seen in figure 2.5.

For the decay of  $^{193m}Pt$  (E level=149.8 keV) to the excited state (E level=14.3 keV), the spin and parity changes from  $13/2^+$  to  $5/2^-$ , which gives possible values for  $\ell = 4, 5, 6, 7, 8, 9$ . The electric decays have even parity when  $\ell=\text{even}$ , and magnetic has even when  $\ell = \text{odd}$ . If parity is unchanged in the decay ( $\Delta\pi=\text{no}$ ), the electric multipoles are even and magnetic multipoles are odd. If the parity does change ( $\Delta\pi=\text{yes}$ ) there would be odd electric and even magnetic multipoles. Hence for the possible transitions between  $13/2^+$  to  $5/2^-$  are whenever  $\Delta\pi=\text{yes}$  and  $\ell = 4, 5, 6, 7, 8, 9$ , which gives

possible M4, E5, M6, E7, M8 and E9 transitions.

In general, the lowest possible multipole dominates, and the emission of a multipole of one order higher ( $\ell + 1$  than  $\ell$ ) is reduced by a factor ca.  $10^{-5}$  ([9], p. 335). Thus a multipole of order 4 or 5 has a low probability of occurring and thus the isomer has a long half-life. In comparison, the decay from  $5/2^-$  to  $3/2^-$  gives possible radiation  $\ell = 1, 2, 3, 4$ ,  $\Delta\pi=\text{no}$ , gives possible M1, E2, M3, E4 and the same for decay from  $3/2^-$  to  $1/2^-$ .

The gamma-lines emitted from  $^{193m}\text{Pt}$  are very weak (figure 2.5). Whenever gamma-decay is possible, another process called internal conversion is competing. It is an electromagnetic process where the nucleus electromagnetically with the atomic electrons, and an atomic electron is emitted instead of the photon ([9], chapter 10, p. 341). The kinetic energy of the emitted electron is the transition energy minus the electron binding energy

$$T_e = \Delta E - B \quad (2.7)$$

where B is the binding energy. The emitted electron is called a conversion electron, and the energy is comparable to the gamma-ray energy. The conversion electron varies with the atomic orbital ([9], p.??), and the electrons following internal conversion are in a spectrum of different discrete energies. The transition energy must be higher than the electron binding energy, and as a consequence the electron is labelled with the shell it was emitted from (remember that atomic shells are labelled with n: n=1=K, n=2=L, n=3=M, n=4=N, etc).

For  $^{193m}\text{Pt}$ , internal conversion is highly favoured before gamma-decay, thus the observed gamma in gamma-ray spectroscopy is weak. The total probability is the summed decay probability for gamma-decay and internal conversion

$$\lambda = \lambda_\gamma + \lambda_{\text{IC}} \quad (2.8)$$

and the internal conversion coefficient  $\alpha$  can be defined as

$$\alpha = \frac{\lambda_{\text{IC}}}{\lambda_\gamma} \quad (2.9)$$

High values for  $\alpha$  indicates high probability of internal conversion relative to the probability of gamma emission but the coefficient diverges towards infinity when  $\lambda_\gamma$  reaches towards zero, which for instance is when the gamma transition is zero. In general, the coefficient increases  $Z^3$ , which will give a much greater coefficient for heavy nuclei than for lighter nuclei. In addition the coefficient decreases rapidly (ca.  $E^{-2.5}$ ) with increasing transition energy. The multipole order also affects the coefficient, where a higher multipole order indicates a higher value. For higher atomic shells than the K shell (n=1) the coefficient decreases like  $n^{-3}$  ([9] chapter 10, p. 346).

From a therapeutic point of view, the most important process is the process which occurs after the release of the conversion electron. There is a vacancy in the shell following the emission of the atomic electron, and an electron from a higher shell or subshell fills this vacancy. Radiative or non-radiative processes can take place after to conserve energy [21]. To conserve energy, an X-ray with the energy equal to the difference between the atomic states can be emitted, or that X-ray can interact electromagnetically with atomic electrons in same subshell, a higher subshell or shell (remember shell: n=1,2.., subshell: spdf.). Dependent on where the ejected electron originated from, the electrons are called super Coster-Kronig, Coster-Kronig or auger electrons respectively. In practice the vacancy moves up to higher atomic shells and the result is a cascade of electrons and Auger electrons, until the reaction "fades out". Due to the low energies, they need to be located close to the cellular nucleus or incorporated into the DNA to induce damage ([1], p. 2203). When incorporated into DNA has they are equally almost effective as  $\alpha$ -emitters [22] ([1], p. 2203).

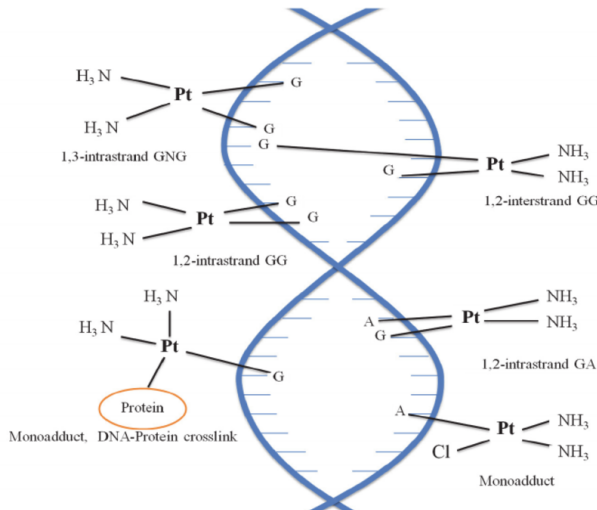


Figure 2.6: The figure shows how cisplatin binds to DNA bases. Try to find new figure, protein is not a part of this, but is a DNA repair protein which is a potentially molecular target for anticancer platinum drug cisplatin. Figure is from [26].

The cellular nucleus is approximately  $6 \mu\text{m}$  in diameter, while the thickness of DNA is approximately 2 nm. According to a simulation done by Howell (1992) [21], the ranges of the electrons from the decay are between 3.29 nm- 231  $\mu\text{m}$ , which implies that the ranges are shorter than the cellular nucleus. According to this simulation, the isomer emits 26.4 Coster-Kronig and Auger electrons (energy released per decay is 10.353 keV) and 3 internal conversion electrons (energy released per decay is 126.738 keV). In addition, X-ray energy deposition of 12.345 keV adds to the total energy deposition. The conversion electrons, contributes to dose?. In this energy region, the energy loss is due to collisions and not bremsstrahlung. The electrons are deflected frequently due to the low mass, and the maximum energy loss is up to half of its kinetic energy per collision as described in equation 2.2.

There are multiple ways that this isomer can be produced, either in a neutron field in a reactor, or in a charged particle accelerator like a cyclotron, via the reactions  $^{192}\text{Pt}(n, \gamma)$  [15] or  $^{192}\text{Os}(\alpha, 3n)$  [23]. One of the issues with production is that  $^{193m}\text{Pt}$  is difficult to produce with high specific activity [15], and the routes are not well investigated either. As described above, with reactors aging, there is a clear benefit of producing in a cyclotron. Otherwise, neutron induced reactions using for instance the UC Berkeley High Flux Generator [24] can be investigated. To work with the highly toxic and difficult material Osmium is not desired, and in addition, the need of enriched target complicates the production [?]. This work is a contribution to an investigation of a new production route, and the data obtained in this work is compared to previous experimental [17, 25].

By itself, not useful for imaging.  $^{191}\text{Pt}$  and  $^{195m}\text{Pt}$  can. Can replace stable N with  $^{13}\text{N}$ , but the half life is so short that the radionuclide can not image the distribution it self, so not as a theranostics pair?? or does cisplatin distribute so fast within the body?

Energy loss of low E auger electrons. In this energy region, is due to collision loss, not bremsstrahlung. Deflects frequently due to low mass, and the max energy loss is  $T_e/2$  per collision, as described in equation 2.2.

## Chapter 3

# General nuclear reaction theory

### 3.1 Nuclear reactions and reaction cross sections

A nuclear reaction occurs when a collision between two nuclei or a nucleus and a subatomic particle takes place. A nuclear reaction is denoted as

$$X(a, b)Y \quad (3.1)$$

where X is the target, a is the incoming projectile, b is the outgoing decay channel and Y is the product of the nuclear reaction ([9], chapter 11.1). There are multiple processes which can occur, radiative capture is the process where a particle is captured and a  $\gamma$ -ray is emitted in a  $(x, \gamma)$  process. If the incoming and outgoing particle is the same, it is a scattering process, where elastic scattering leaves the target nucleus in the energy same state, and inelastic if the target nucleus is in an excited state. In addition, fission can occur, but not for the reactions in this work. In these types of experiments however, we are interested absorption of the incoming particle, and emission of particles to create products in which we can measure the reaction cross section.

In a nuclear reaction, the total energy and linear momentum, proton and neutron number, angular momentum and parity are conserved quantities (assuming no meson formation) ([9], p.380). A nuclear reaction can result can be a compound-reaction, pre-equilibrium-reaction or direct-reaction [27]. The compound nucleus model (Bohr, 1936) [28] is a model which describes the formation of a compound nucleus by absorption of an incoming projectile by a nucleus close enough to interact with the strong nuclear force, and the decay of the compound nucleus. The kinetic energy shared between the incoming projectile and the nucleon which was struck leads to multiple collisions with other nucleons and rapid exchange of energy. The energy is distributed throughout the nucleus, leaving the original nucleus in an highly excited state. There is a statistical probability that enough energy will be concentrated on one single nucleon or group of nucleons such as protons, neutrons and alpha-particles, and escape the potential barrier of the nucleus (also referred to as evaporation), which lowers the excitation energy [9], chapter 11.10, p. 416). Compound nuclear reactions have an interaction time of ca.  $10^{-18}$  seconds, achieving thermal equilibrium [27]. Since the nucleons collides rapidly, the information regarding the initial energy and the direction of the incoming particle is lost, and the outgoing decay channel depends only on conservation of the energy and angular momentum. As shown in figure 3.1, where a  $^{10}\text{B}$  nucleus interacts with a deuteron ( $^2\text{H}$ ), compound nuclear reactions can be divided into two stages; fusion of incoming particle and target nucleus, and evaporation of nucleons or groups of nucleons. This is decay of the compound nucleus, and this will lower the excitation energy. Compound nuclear reactions dominates in the low energy region (below 10 MeV) cant find a citation on this.. Andrew: you said that direct reactions take place above 200 MeV, but [27] says that direct reactions dominates over 10 MeV and compound under 10 MeV.

The contrary, direct reactions have interaction time of ca.  $10^{-22}$  seconds, and dominates at high energies, above 10 MeV. The reaction involves interaction with single nucleons, and can be elastic, transfer or break up, as shown in figure 3.1. Since the incoming particle interacts with a single nucleon, the exit channel depends heavily on conservation of spin and parity, in addition to energy and mass.

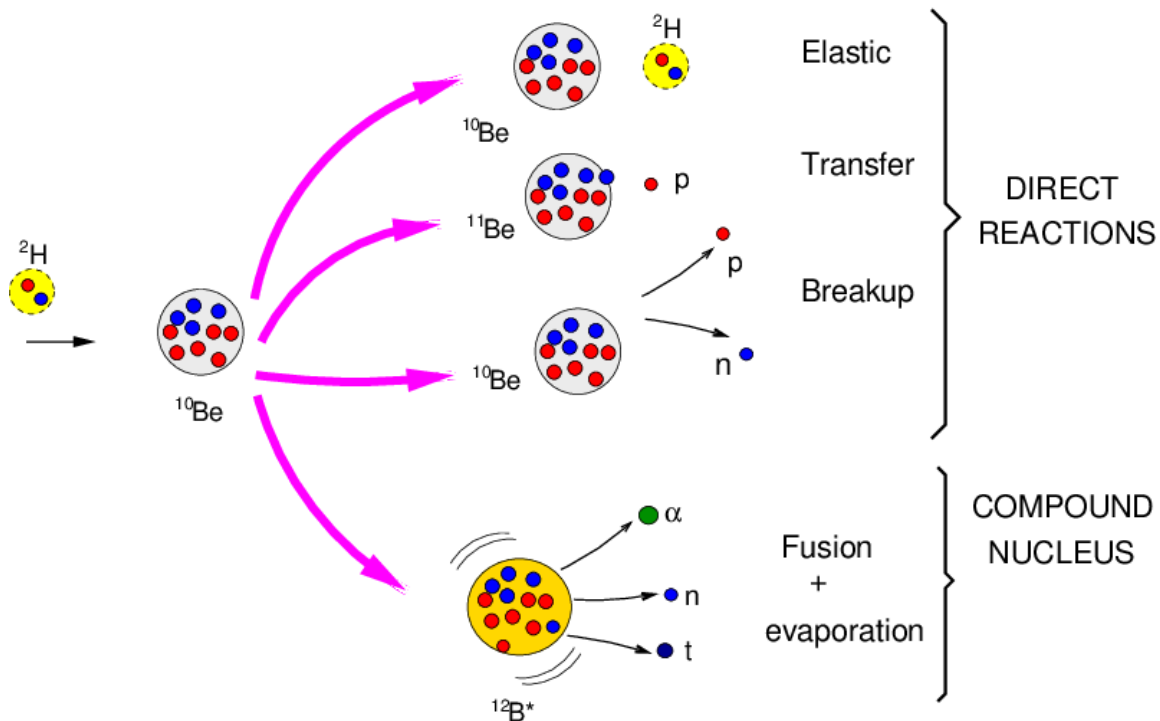


Figure 3.1: The figure shows how direct and compound nuclear reactions differ. Figure is from [29].

An intermediate reaction between compound and direct reactions are the pre-equilibrium reactions, where the incoming particle does not lead to a thermal equilibrium, but the information of initial energy and direction is lost. This is an important contribution for energies between 10 and more than 200 MeV [27]. In this work, compound nuclear formations and pre-equilibrium are observed, with a compound peak where one more reactions contributes to a peak, and the pre-equilibrium tail of the high energy side of the compound peak.

A Nuclear reaction cross section represents the total probability that a compound nucleus will be formed and that it decays by a certain decay channel with particle emission. A way to visualize a nuclear reaction cross section is by imagining the incoming particle and the target nucleus as spheres, and if they overlap, the reaction will occur. The total reaction cross section is therefore proportional to the cross-section area of the two spheres

$$\sigma_R = \pi r_0^2 (A_X^{1/3} + A_a^{1/3})^2 \quad (3.2)$$

where  $r_0$  is a constant ( $\approx 1.6$  fm),  $A_X$  and  $A_a$  are the atomic mass number of target A and incoming particle a, and the radii of the nuclei are connected via  $r_0 A^{1/3}$ . The unit of a cross section is therefore in a unit of area, typically in millibarn ( $1 \cdot 10^{-27} \text{ cm}^2$ ) [30], p. 8. The total reaction cross section between the incoming particle and the target nucleus is a more or less constant value, with the summation of the various nuclear reactions which can take place

$$\sigma_{\text{tot}} = \sum_b \sigma(a, b) \quad (3.3)$$

The outgoing decay channel can be inelastic and elastic scattering  $X(a,a)Y$  and  $X(a,a^*)Y$ , radiative capture  $X(a,\gamma)Y$  and absorption and compound nucleus formation  $X+a \rightarrow C^* \rightarrow Y+b$ .

([3], p. 23). The cross section for a nuclear absorption reaction to occur via the formation of the compound nucleus by the collision of a projectile with a target nucleus, and the decay of the compound nucleus via decay channel b can be expressed as

$$\sigma(a, b) = \frac{\sigma_c P_b}{\sum_b P_b} \quad (3.4)$$

where a is incoming projectile and b is decay channel,  $\sigma_c$  is the formation of compound nucleus CS, and  $P_b$  is the probability of compound nucleus decaying into channel b. In general, product produced via emission of neutrons and protons has the highest probability, but particles such as alpha, tritons, deuterons and  $^3\text{He}$  can occur before because of the lower binding energy per nucleon, which will be described in the next section.

The cross section of a certain reaction (in a thin target) to take place can be estimated based on the production rate, the number of target nuclei, the beam flux or beam current ([9], chapter 6)

$$\sigma(E) = \frac{R}{N_T \cdot \Phi} \quad (3.5)$$

Based on the induced activity in the target, the irradiation time and decay product nuclei during irradiation, the cross section can be found experimentally, with gamma-ray spectroscopy, which is used in this work:

$$\sigma(E) = \frac{A_0 \cdot t_{\text{irr}}}{N_T \cdot \Phi(E)(1 - e^{-\lambda t_{\text{irr}}})} \quad (3.6)$$

where  $A_0$  is the end of beam activity of the resulting product nucleus (Y),  $t_{\text{irr}}$  is the irradiation time,  $N_T$  is the number of target nuclei (X),  $\Phi(E)$  is the projectile flux or current (a), and  $\lambda$  is the decay constant of the product nucleus.

For each possible decay channel of the compound nucleus, there is an associated probability or cross section, which is dependent on the energy of the incoming projectile. A function which evaluates the various cross sections at different energies is called an excitation function. In figure 3.2, the excitation function of the reaction channels for the platinum isotopes  $^{188,189,191,193m}\text{Pt}$  resulting from deuterons on natural iridium is plotted (using TENDL-2019 nuclear reaction code [cite](#)). Natural iridium consists of two stable isotopes,  $^{191}\text{Ir}$  (37.3% abundance) and  $^{193}\text{Ir}$  (62.7% abundance).  $^{193m}\text{Pt}$  can only be produced from  $^{191}\text{Ir}$ , ejecting 2 neutrons in the process, which can be denoted as  $^{193}\text{Ir}(\text{d},2\text{n})^{193m}\text{Pt}$  ( $^{193}\text{Pt}$  is the compound nucleus formation of deuteron on  $^{191}\text{Ir}$ , which has a low production cross section). The other platinum isotopes can be produced as  $^{191}\text{Ir}(\text{d},2\text{n})^{191}\text{Pt}$  or  $^{193}\text{Ir}(\text{d},4\text{n})^{191}\text{Pt}$ ,  $^{191}\text{Ir}(\text{d},4\text{n})^{189}\text{Pt}$  or  $^{193}\text{Ir}(\text{d},6\text{n})^{189}\text{Pt}$  and  $^{191}\text{Ir}(\text{d},5\text{n})^{188}\text{Pt}$  or  $^{193}\text{Ir}(\text{d},7\text{n})^{188}\text{Pt}$ . For each reaction route possible, there is a resulting compound peak, hence,  $^{193m}\text{Pt}$  has only one peak, and the other platinum isotopes have two. In addition, the long exponential tail which can be seen for  $^{193m}\text{Pt}$  is the pre-equilibrium reaction. The desired particle emission is energy dependent, and the higher energy provided to the compound nucleus, the probability that more particles will be emitted is higher ([9], chapter 11.10, p. 419). When a specific isotope is desired, the excitation function can tell us which energy window that maximizes the production and most importantly minimizes particularly other isotopes of the same element, due to the difficulty of separating same chemical elements. This is why it is important to find which window that maximizes the production.

tally 1.9 in reader can contain important info!

### 3.1.1 Constraints in nuclear reactions

The potential energy of a nucleus is the sum of the attractive well from the strong nuclear force and the repulsive Coulomb barrier which acts repulsive between charged particles and the nucleus, acting long range (p. 152, [1]). The radius of the potential well is up to a few femtometer. For a positively charged particle induced nuclear reaction, the energy of the particle should exceed the barrier, or there will be an elastic scatter. However, there is a chance of tunneling, which drops with a factor  $1/r$  where  $r$  is the distance from the center of the nucleus ([1], chapter 3 - Nuclear Reactions, section, 3.2.3). The barrier also constraints the emission of particles for a decay channel of the compound nucleus, as the energy for an outgoing decay channel of positive particles must exceed the barrier.

The height of the Coulomb barrier is dependent on the radius and charge of the incoming or outgoing particle a and the target nucleus X.

$$U_{\text{Coulomb}} = \frac{1}{4\pi\epsilon_0} \frac{e^2 Z_X Z_a}{r_X + r_a} \quad (3.7)$$

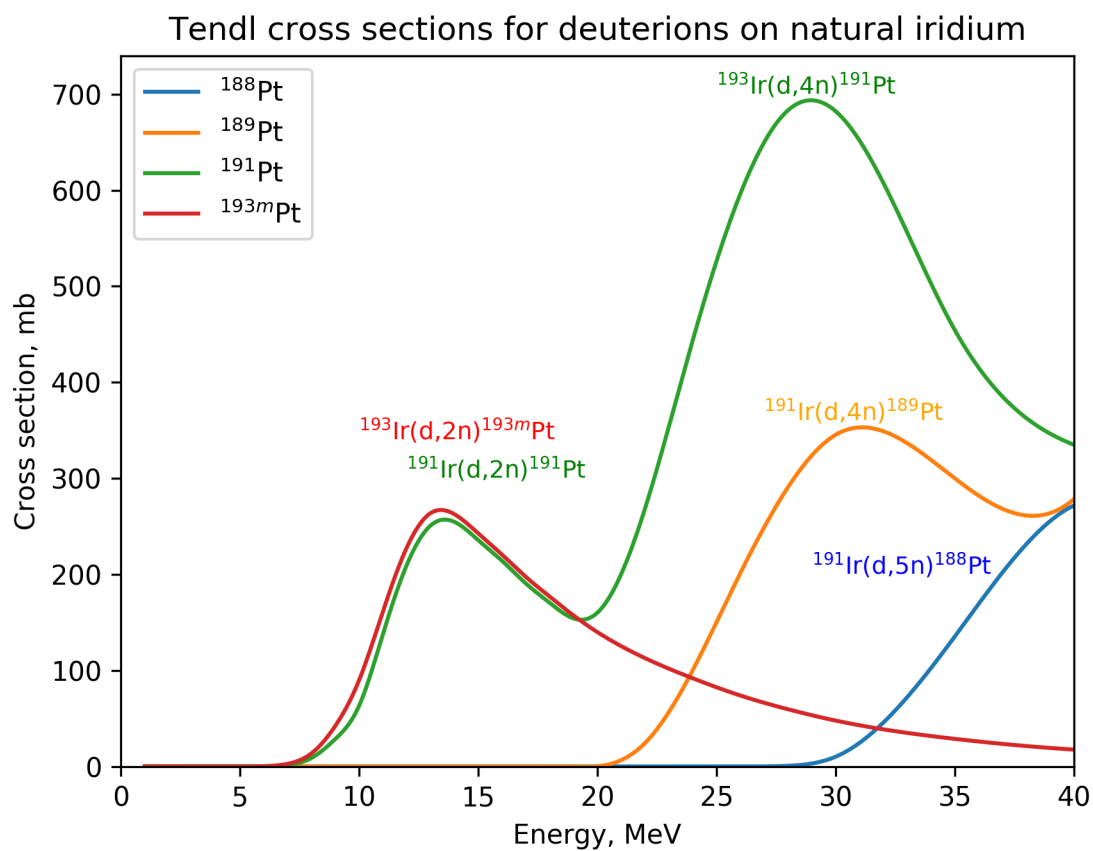


Figure 3.2: Reaction cross sections provided by Tendl for the reactions  ${}^{\text{nat}}\text{Ir}(\text{d},\text{x})^{188,189,191,193m}\text{Pt}$

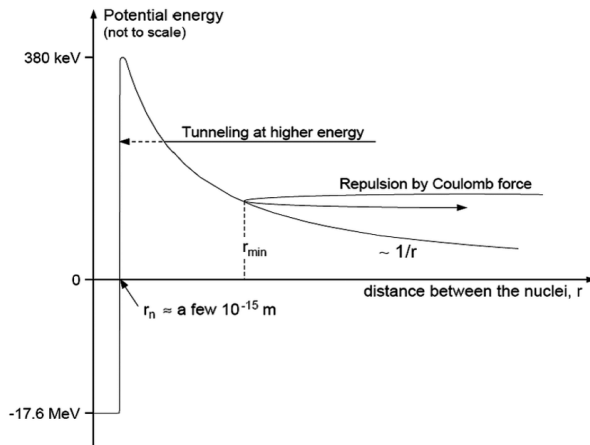


Figure 3.3: The Coulomb barrier decreases exponentially, and contributes to a constraint in a nuclear reaction, since the energy of the particles must have a certain energy to interact. Figure is from [31].

In addition, there is a centrifugal barrier, which can constraint some of the incoming particle energy in rotational energy, **which depends on the angular momentum of the incoming particle and and the nucleus???** ([1] p. 155.).

$$U_{\text{centrifugal}} = \frac{\hbar\ell(\ell+1)}{r^2} \quad (3.8)$$

The sum of the barriers are the total barrier but the Coulomb barrier is the most important.

In a nuclear reaction, the mass-energy is conserved, which is denoted as the Q-value. The reaction Q-value is the difference in masses between before and after the nuclear reaction occurred ([9], chapter 11.2). It is defined as

$$Q = (m_i - m_f)c^2 = (m_X + m_a - m_Y - m_b)c^2 \quad (3.9)$$

where  $m_i$  is the initial mass,  $m_f$  is the final mass and  $c$  is the speed of light. If  $Q > 0$ , then the reaction is exoergic, which means that energy is released in the reaction. There is no threshold energy of the projectile required for the reaction to occur, if only the projectile is present the reaction can occur. If  $Q < 0$ , then the reaction is endoergic, which means that the kinetic energy of the incoming projectile is converted into nuclear mass or binding energy. For endoergic reactions to occur, there is a minimum threshold energy of the projectile in order for the reaction to happen, which is defined as ([9], 11.2, p. 382)

$$E_{\text{threshold}} = (-Q) \cdot \frac{m_Y + m_b}{m_Y + m_b - m_a} \quad (3.10)$$

The energy threshold thus depend on the Q-value, the Coulomb barrier can constrain charged particle-reactions, and the centrifugal barrier can constrain reactions if angular momentum  $\ell \neq 0$ . **The parity though depend, even numbers of  $\ell$  mix with even, and odd with odd ([1], chapter 3Nuclear Reactions, section, 3.2.3)??** This gives an indication on when a reaction can energetically occur, but does not tell us how probable the reaction is.

The binding energy is the mass-difference between the nucleus as a whole, and the number of protons and neutrons added

$$B = c^2(z \cdot m_p + n \cdot m_n - m_N) \quad (3.11)$$

where  $z$  is the number of protons,  $n$  is the number of neutrons,  $m_p$  is the proton mass,  $m_n$  is the neutron mass,  $M_N$  is the mass of the nuclide, which is the number of nucleons  $A$  minus the number of electrons,  $M_P = m_A - z \cdot m_e$  (the electronic binding energy per electron is excluded). From Krane's derivation of the nuclear binding energy ([9], chapter 3.3, p. 65).

From equation 3.9, the larger the mass of the outgoing decay channel, the more negative the Q-value will be. Protons ( $q=+1$ ) and neutrons ( $q=0$ ) are the simplest decay channels of the compound nucleus, each carry a spin of  $1/2$ , with masses  $m_p = 938.28 \text{ MeV}/c^2$ , and  $m_n = 939.57 \text{ MeV}/c^2$  respectively. Combinations like deuterons ( $d=1p+1n$ ,  $q=+1$ ) has a mass difference of  $\Delta = 2.2 \text{ MeV}/c^2$  from realising 1 proton and 1 neutron separately, a triton ( $t=2n+1p$ , charge +1) with  $\Delta = 8.5 \text{ MeV}/c^2$ ,  $^3\text{He}=1n+2p$ , charge +2 with  $\Delta = 7.7 \text{ MeV}/c^2$  and alpha-particle ( $\alpha=2n+2p$ , charge +2) with  $\Delta = 28.3 \text{ MeV}/c^2$ . Thus, Q-values are higher in value, the lighter the particle is. However, in this work, we can clearly see that protons, neutrons and alpha-particles are strongly fed decay channels, while the other decay channels does occur but are mostly not observed due to the low cross section.

## 3.2 Nuclear reaction models

The optical model (proton/neutron, and alpha/deuteron), gamma strength function. **talys 1.9 in reader can contain important info! p. 525**. Optical, gamma-ray strength, compound and preequilibrium. Also read the introduction.

Theoretical nuclear reaction models are important, for both the general understanding of the physics in the data, and to estimate the required cross sections in cases where the data does not make sense or is not available( [3], p. 23). In addition, can weight contradictive measurements.

**EMPIRE 3.2.3**

**CoH 3.5.3**

**ALICE 2017**

**TALYS 1.9**

**TENDL 2019**

# Chapter 4

## Experimental setup

This chapter intends to give a overview of the experimental set-up which was used to obtain the cross section measurements. The stacked target method is described in section 4.1, and the foil characterization is described in 4.2. The facility of the Lawrence Berkeley National Laboratory's 88-Inch cyclotron is described in section 4.3. Gamma-ray spectroscopy with high purity Germanium detectors including energy and efficiency calibration is described in section 4.4. The analysis is described in chapter 5.

### 4.1 The stacked target activation method

In this experiment, the stacked target activation method was used to measure multiple cross sections using one single incident charged-particle beam on a stack of thin targets. The incident beam energy is degraded as it traverses the stack of targets, and each foil is activated at a different energy. The cross sections are estimated based on the activation of each product in each foil, resulting in multiple cross section measurements at multiple energies. This method originates from Graves et. al. (2016) [32] using an incident 90 MeV proton beam on thin iron, copper and aluminum foils. Multiple similar experiments have taken place at the 88-Inch Cyclotron over the past years [33–35]. This method involves well-characterized foils with accurately measured areal density, and the use of monitor foils in each target compartment, where reactions with well-characterized cross sections are used to estimate the beam current in each compartment.

If a target of stable nuclei is assumed, which is exposed to a particle beam which induces various nuclear reactions, the constant rate of production,  $R$ , of a specific reaction is dependent on the number of target nuclei,  $N_T$ , the current or flux of the particle beam,  $\Phi$ , and the reaction cross section,  $\sigma$ .

$$R = N_T \Phi \sigma \quad (4.1)$$

In the assumption of the production rate being a constant value, the number of transformed target nuclei is small in comparison to the total number during the irradiation time. The number of produced nuclei from a specific reaction per unit time is thus the produced nuclei minus the decayed nuclei

$$dN = Rdt - \lambda Ndt \quad (4.2)$$

which has the solution

$$N(t) = \frac{R}{\lambda} (1 - e^{-\lambda t}) \quad (4.3)$$

where  $\lambda$  is the decay constant of the nucleus. The activity of a product is defined as the desintegration rate

$$A = \frac{dN}{dt} = \lambda N \quad (4.4)$$

Equation 4.3 can be rewritten to

$$A(t) = R(1 - e^{-\lambda t}) = N_T \Phi \sigma (1 - e^{-\lambda t}) \quad (4.5)$$

At the end of beam, the activity is denoted as  $A_0$ , and  $t$  is the irradiation time:

$$A_0 = N_T \Phi \sigma (1 - e^{-\lambda \Delta t_{\text{irr}}}) \quad (4.6)$$

Solving this equation, the cross section can be estimated via

$$\sigma = \frac{A_0}{N_T \Phi (1 - e^{-\lambda t_{\text{irr}}})} \quad (4.7)$$

(From [9], chapter 6)

The stack consisted of ten natural iridium (99.9%), ten natural nickel (..), ten natural copper (..) and ten natural iron (..) from Goodfellow Corporation, Corapolis, PA 15108, USA. Deuteron-induced products from iridium was the main motivation behind this experiment, primarily because of the potential medically valuable  $^{193m}\text{Pt}$ -isomer, and the contribution of nuclear reaction data of the natural iridium ( $d, x$ ) reactions. For the latter three targets, the well-characterized cross section reactions  $^{\text{nat}}\text{Fe}(d, x)^{56}\text{Co}$ ,  $^{\text{nat}}\text{Ni}(d, x)^{61}\text{Cu}^{56, 58}\text{Co}$  and  $^{\text{nat}}\text{Cu}(d, x)^{62, 63, 65}\text{Zn}$  from the IAEA monitor database [36] were used to estimate the weighted average beam current throughout each compartment of foils. The full stack design can be seen in table 4.1. In addition to the target foils, two 316 stainless steel foils were placed in the front and the back of the stack, and a 6061 aluminum alloy which works as a proton degrader along with a nickel neutron monitor foil to measure broken up deuterons (protons+neutrons) and see if flux can affect the production??. Since the number of targets in the stack worked as a beam degrader, the need of additional energy degraders in the stack was not necessary. The stainless steel worked as a beam profile monitor, as the activated foils could be used to develop Gafchromic films (radiochromic films) which contains a material changing color when exposed to ionizing radiation which can be used to build confidence in the spatial beam profile in the front and in the back of the stack. The number of target nuclei in each foil was measured with a thorough characterization of each foil, measuring the width, the length across each side and the mass. The activities as a function of time since end of beam were measured with gamma-ray spectroscopy with pre-calibrated high purity germanium detectors, and the end of beam activities were estimated by backpropagating back in time fitted to the appropriate decay curve, from the Bateman equations [37]. The beamcurrent was estimated using the activation of the monitor reactions and the well-characterized cross sections. For energy assignments, the NPAT (Nuclear physics analysis tool) Monte-Carlo based code which is based on the stoppingpower formalism of Anderson & Ziegler [38, 39] estimated the flux-averaged energy distribution over each foil, and the energy assignments for each single foil. In addition, the full stack design was decided upon the energy-degradation of the stack with NPAT's Ziegler simulation, so that all the foils were activated. The weighted average beam current in each compartment was estimated based on each single measurement. Finally, the flux-averaged cross section was estimated.

For a thin foil, the beam degradation is small in comparison to thick targets, and the uncertainty in beam energy is thus small. In addition, the use of thin foils with a thickness of a few  $\mu\text{m}$  allows for low activation in each foil, which reduces dead time of the detector, along with lower dose to workers which is advantageous for isotope production and cross section measurement [15].

Targets were ca. 25 by 25 mm and 25  $\mu\text{m}$  thick. The beam was ca. 1 cm in diameter, so the beam was underfilling the targetfoils. Why was it important that the beam was underfilled. On how was this related to the areal densities?

## 4.2 Characterization of the target foils

The iridium foils were bought in 25 by 25 mm squares, and the copper, iron and nickel foils were cut into approximately 25 by 25 mm squares, where each foil was cut from the same sample. The length of

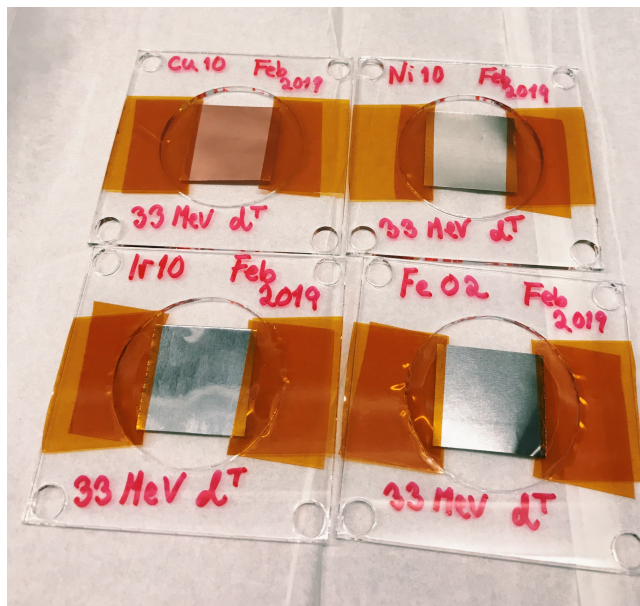


Figure 4.1: The figure shows the four different targets mounted on plastic frames with a hollow center with kapton tape attached along the edges of the foils.

each foil along each side and the thickness was measured with a caliper (Mitutoyo Absoule Digimatic) and a gauge caliper (Mitutoyo IP65 Coolant Proof) respectively. An analytical balance weight (Mettler Toledo) was used to measure the mass of each foil which was prewashed with isopropanol to clear the foils from surface contamination. Each unit was measured four times, and the values listed in table 4.1 are the averaged measurements. The mass density was calculated for each foil which was calculated using the average mass of each foil, divided by the averaged area. The uncertainty in the areal density was calculated as the standard deviation of the data described in equation A.2. The areal densities were later in the analysis converted to number of nuclei per  $\text{cm}^2$ , which was done numerically multiplying the mass density with Avogadro's number, and dividing by the mol-mass of the target atoms. The measured thicknesses were not used in the analysis, but was a confirmation that the foils were ca.  $25 \mu\text{m}$  in thickness. The measured values varied from  $24.3 \mu\text{m}$  (Ir03) to  $34.8 \mu\text{m}$  (Cu02), which were within accepted values.

After the characterization, each foil was mounted on ca.  $1.6 \text{ mm}$  thick plastic frames over a hollow center and attached with **3M 5413-Series Kapton polyimide film??** tape along the edges. From previous experiments, the Kapton tape has been used to seal the foils into airtight pockets for foil containment, but has appeared to have an impact on the proton stopping power [33]. Therefore it was not placed over the activation surface. The target frames with the attached foils can be seen in figure 4.1. For irradiation, the foils were placed in a target holder which was a 6061 aluminum alloy with a hollow center in the front for the beamline to pass through. A hollow spring was used to keep the foils stable during the irradiation. The target holder can be seen in figure 4.11 (left).

### 4.3 Lawrence Berkeley National Laboratory's 88" Cyclotron

Lawrence Berkeley National Laboratory (LBNL) [40] is a national research laboratory on behalf of the U.S. Department of Energy through its Office of Science, and is operated by University of California, Berkeley. LBNL was founded by Ernest Orlando Lawrence, the inventor of the cyclotron, in 1931 [41]. The 88-Inch Cyclotron has a cyclotron number of  $K=140$ , and can accelerate both light and heavy ions up to Uranium. [42]. The cyclotron has many purposes, The researchgroup which does isotope production at the facility works with development of nuclear reaction data, along with researching production methods of medically valuable radionuclides. There are multiple other programs that take place in the facility which include chip testing and space effects testing, super heavy element searches, fundamental nuclear structure measurements, novel scintillation characterization, fission yield and

CHAPTER 4. EXPERIMENTAL SETUP

Table 4.1: Characterization of each foil, along with calculated mass density. Each length is measured in mm, and mass in grams. \*: measured from previous experiments

Foil	Length1 (mm)	Length2 (mm)	Thickness (mm)	Mass (g)	Mass density (mg/cm <sup>2</sup> )
SS1					
Ni01	25.228	25.293	0.0285	0.1453	22.772 ± 0.138
Ir01	24.943	24.968	0.0295	0.3436	55.174 ± 0.053
Cu01	25.553	24.883	0.0341	0.1420	22.338 ± 0.048
Fe01	24.400	26.068	0.0278	0.1274	20.030 ± 0.110
Ni02	25.288	25.428	0.0295	0.1487	23.118 ± 0.096
Ir02	24.923	25.005	0.0278	0.3465	55.601 ± 0.238
Cu02	25.443	25.550	0.0348	0.1451	22.325 ± 0.028
Fe02	25.525	23.800	0.0274	0.1216	20.017 ± 0.034
Ni03	25.295	25.210	0.0270	0.1425	22.338 ± 0.066
Ir03	24.885	24.983	0.0243	0.3459	55.643 ± 0.121
Cu03	25.560	25.508	0.0343	0.1455	22.313 ± 0.043
Fe03	26.113	25.235	0.0310	0.1315	19.948 ± 0.114
Ni04	25.303	24.888	0.0273	0.1304	20.704 ± 0.068
Ir04	24.960	24.833	0.0261	0.3471	56.000 ± 0.109
Cu04	25.153	25.603	0.0333	0.1435	22.284 ± 0.027
Ni05	25.325	25.495	0.0263	0.1406	21.768 ± 0.045
Ir05	24.948	24.958	0.0256	0.3435	55.161 ± 0.081
Cu05	25.213	25.573	0.0334	0.1447	22.443 ± 0.028
Ni06	25.530	25.195	0.0285	0.1471	22.861 ± 0.123
Ir06	24.760	24.960	0.0240	0.3444	55.731 ± 0.088
Cu06	25.343	25.513	0.0340	0.1448	22.396 ± 0.012
Ni07	25.338	25.278	0.0268	0.1479	23.092 ± 0.078
Ir07	24.955	25.008	0.0278	0.3538	56.685 ± 0.085
Cu07	25.625	25.248	0.0326	0.1444	22.320 ± 0.014
Ni08	25.205	24.950	0.0256	0.1409	22.409 ± 0.124
Ir08	24.723	24.985	0.0281	0.3585	58.030 ± 0.130
Cu08	25.370	24.885	0.0333	0.1414	22.401 ± 0.033
Ni09	25.220	25.378	0.0257	0.1392	21.741 ± 0.073
Ir09	24.670	24.993	0.0273	0.3494	56.669 ± 0.043
Cu09	25.390	26.455	0.0331	0.1506	22.425 ± 0.041
Ni10	25.285	24.405	0.0271	0.1425	23.093 ± 0.024
Ir10	24.973	24.980	0.0270	0.3435	55.065 ± 0.055
Cu10	25.470	25.338	0.0355	0.1440	22.314 ± 0.047
SS2					
P-degrader					
Ni neutron monitor					

neutron inelastic scattering measurements (GENESIS).

A cyclotron is a device that accelerates positively charged particles. It is operated by an alternating (radiofrequency) electric field, and a perpendicular magnetic field, which by the Lorentz Force forces the particle to accelerate in an outward spiral. The 88-Inch cyclotron is an isochronous cyclotron, with a magnetic field that increases with radius. The ions which are accelerated are produced by ECR ion sources and injected into the cyclotron. The facility is figured in 4.2, and consists of a cyclotron vault and experimental caves, where cave 01/02 is where the irradiation of the target stack took place. Cave 4C is today used for gamma-ray spectroscopy, where 6 of a total of 7 high purity germanium detectors which were used in this work were located. Faraday cups can measure the beam current at different steps along the beamline. In total there are six electrically isolated beamlines which can be used for irradiation. From the cyclotron vault, the beam is directed and focused to the correct beamline with bending magnets and quadrupole magnets in the cyclotron vault. From de-acceleration of the beam particles, some particles are lost and the transmission efficiency can be calculated by comparing the current at the Faraday cup right after (BS-02) the particles have gained the desired energy, and

current at the Faraday cup right before the particles are in the end of the beamtube of cave 01/02 (FC-01) can be measured.

## 4.4 High purity Gerganium detector

For the gamma-ray spectroscopy, seven different high purity germanium detectors with coaxial right cylinder geometry were used. Six mechanically cooled p-type IDM Ortec detectors (detectors 1-6) with detector diameter 85 mm, detector length 30 mm, hole depth 15 mm and hole diameter 9 mm. The detector volume was  $169.996 \text{ cm}^3$  (assuming detector hole cylindrical). The outside contact layer was doped with lithium, and the hole contact layer with boron. In addition one liquid-nitrogen cooled n-type ORTEC GMX series (mode: GMX-50220-S) Germanium detector which also had a thin beryllium window for improved x-ray efficiency (detector 7), with detector diameter 64.9 mm, detector length 57.8 mm, hole diameter 9.4 mm and hole depth 48.6 mm. The detector volume was  $190.365 \text{ cm}^3$ . The outside contact layer was doped with boron and the hole contact layer was doped with lithium. Detectors 1-6 were measuring gamma-ray spectroscopy from a horizontal point of view, while detector 7 measured gamma-rays from vertically.

The high purity Germanium detector is a type of semiconductor, which is a material where the energy required to remove an electron from the valence band (in the outer atomic shell) to the conduction band is small. The germanium atom has atomic number 32, and 4 valence electrons in the outer p4 shell (need citation?). The atoms in the detector are bound through covalent bonds in a crystal structure. The main mechanism of a semiconductor is creation of electron-hole pairs after energy deposition of an ionizing particle in the crystal. If an electron is excited to the conduction band, a hole is left. This hole can move as a neighboring electron fills this spot, leading to a chain reaction, as the hole will move in the crystal. Both the electron in the conduction band and the hole in the valence band contributes to an electric current ([10], p. 215-216).

The major advantage with semiconductor detector is that the average energy to create an electron-hole pair is very low, which results in a superior energy resolution in comparison to other detectors like gas and scintillation detectors. At 77K, the average energy is 2.96 eV to create an electron-hole pair ([10], p. 228). High energy resolution is important, dependent on the energy difference of two close lying gamma-peaks and the resolution, the two peaks can be distinguished. For 1000 keV, the resolution of a Germanium detector is 0.1%, which means that it is possible to separate two gamma-ray peaks within ca. 1 MeV ([10], p. 117).

The detectors are doped to create an imbalance in the number of holes and electrons in the conduction band in a pure crystal ([10], p. 220), either by creating an excess of holes by adding a an acceptor of electrons (p-type) or by adding a donor of electrons so there is an excess of electrons (n-type). In reality, both dopants are present (so there is a p-n junction), but the dopant with the highest occurrence has the highest probability of interacting with radiation. The n-type material will have more electrons which will move toward the p-type material, and visa versa. Therefor, an imbalance arises due to the p-type having an access electrons, and the n-type having an access of holes near the equilibrium. The region where there is an imbalance is called the depletion zone, and a potential across the junction of donors and acceptors) arises. When electrons from p-type or holes from n-type comes near the depletion zone (which diffuses towards the side with the opposite charge), will be swiped back due to the equal charge on the depletion zone. This will create a voltage current which is assigned to a channel number as a count. The gap is quite narrow, but when a bias voltage voltage is applied between the inner and outer radii of the detector cylinder, the depletion zone width increases. With this diffusion of electrons and holes process, the surface layer becomes heavily doped. The consequence is a thick dead layer which can attenuate or stop radiation before entering the detector volume ([10], p. 233). Figure 4.3 is shows the principle of a n-type coaxial cylinder detector. Where the inner hole as an overweight in positive charges, and the electrons resulting from an incident ionizing particle diffuses towards the hole.

The efficiency of a detector is the number of events registered divided by the events emitted by the source. The absolute efficiency can be divided into intrinsic and geometrical efficiency, where the intrinsic efficiency is the number of events registered by the number of events hitting the detector. The intrinsic efficiency thus depends on the interaction cross section between the incident particle and the detector material, **and as described above, the IDM's having a larger surface, the geoemtrical efficiency is larger**. For neutral particles like photons, the size affects the intrinsic efficiency, as the probability of interaction gets larger. The geometrical efficiency is based upon the shape, and is the radiation emitted by the source which hits the detector ([10], p. 121-122), and is therefor dependent on the solid angle. The detector volumes were comparable in size. However, due to the former being broader and shorter (higher surface area, and higher solid angle), the relative efficiency of the IDM-detectors are lager (ca. 52%) than the germanium detector (ca. 20%). Therefor, the IDM-detectors are more sensitive to background radiation. The IDM-detectors were located in cave 4C (see figure 4.2), which have previously been used as radiation chamber. Thus, background radiation was present. Detectors 1-6 were used for high efficiency counting of foils. For detector 7, there was led shielding around the detector. In addition, the detector had a slightly higher resolution, and was therefor used for precision measurementsThe resolution of a detector is defined as the the fwhm of the peak divided by the true gamma-line. Using the 661.657 keV (85.10%) gamma-line of  $^{137}\text{Cs}$ , the resolution of detector 1 at 10 cm was 0.28% while it was 0.25% for detector 7 at 10 cm.

The duration of a voltage pulse signal takes to construct is important, because other events that occurs meanwhile cannot be registered. This leads to a dead time, which is time where nothing is recorded ([10], p. 120). The time that a detector registers an event is called the live time, which is the real time minus the dead time. Ideally, a system that does not add dead time to the existing (non-paralyzable) is preferred to reduce the amount of time where the detector is not detecting. In order to visualize the signal from the detector, Maestro (Multichannel Analyzer Emulation Software<sup>1</sup>) was used.

#### 4.4.1 Obtaining a spectrum

The electrical signal (voltage pulse) registered in a detector has a net-electrical charge which is proportional to the amount of gamma-ray energy which was registered in the detector ([44], p. 61). The electrical signal is assigned a channel number, which is in accordance with the charge collected. To obtain a spectrum, the number of registered events in each channel is counted, and the well-known peaks of the gamma-ray spectrum rises. Ideally, the peaks would appear as step functions, as the gamma-ray energies are discrete. The counts in the channel close to the channel representing the true peak appears in a histogram which follows a Gaussian shape ([44], p. 186). Due to incomplete charge collection (ie. that electrons or holes are not collected), moves counts from the center of the distribution to lower channels, creating a low energy tail of the peak ([44], p. 135). **The shape of the peaks are represented in the following equation as a function of the channel number**

$$\text{peak}(x) = A \cdot \left[ e^{-\frac{(x-\mu)^2}{2\sigma^2}} + R \cdot e^{\frac{i-\mu}{\alpha\sigma}} \left( \frac{1-\mu}{\sqrt{2\sigma}} + \frac{1}{\sqrt{2\alpha}} \right) \right] \quad (4.8)$$

where blablabal.... John papers. Maybe not include because cannot describe.... SHPOULD ALSO INCLUDE HOW THE COUNTS ARE CALCULATED, are those within

The observed gamma-peaks in the spectra obtained in this work are results of beta-decay where the observed gamma-rays are from the decay of the excited daughter nucleus, or gamma-rays from decay of isomeric states. If two nuclei feeds into the same daughter nucleus, the possibility of populating the same energy level is present.

In a detector, the main interactions of gamma-rays and X-rays are via the photoelectric effect, Compton scattering and pair production ([10], p. 53). As described in section 2.1, photons are attenuated

---

<sup>1</sup><https://www.ortec-online.com/products/application-software/maestro-mca>

exponentially as a function of depth of medium and the absorption coefficient of the medium, but not degraded in energy (equation 2.4). Therefor, the gamma-radiation is highly penetrating, and some gamma-rays will also escape the detector volume. Therefore, large detector volumes are desired, to increase chances of all radiation being deposited in the detector ([44] p. 32). The attenuation coefficient is the sum of all the possible interactions (including Raleigh and Klein-Nishina scattering). In a detector, photopeaks are desired, where all the photon energy is deposited within the detector. Photoelectric effect occurs when a photon is completely absorbed by an atomic electron, and this effect dominates at low photon energies. This effect is desired in gamma-ray spectroscopy, as all the total energy of the gamma-ray will be registered in one photopeak. The probability of photoelectric effect is proportional to the  $Z^4$  or  $5$ , and inversely proportional to the gamma-ray energy. Therefor, a high Z-material is desired to increase the probability

$$\tau \propto \frac{Z^n}{E_\gamma^{3.5}}, \quad n = 4, 5 \quad (4.9)$$

In Compton scattering, the photon transfers parts of its energy to an assumed electron at rest, and is scattered with an angle  $\theta \in (0^\circ, 180^\circ)$ . Dependent on the angle, the energy of the deflected photon will vary, and give a spectrum of different energies, where higher scattering angle transfers more energy to the recoil electron. If the final photon escapes the detector, the count will not appear close to the photopeak, but instead contribute to a Compton continuum. The probability of Compton scattering is proportional to the detector Z-value

$$\sigma \propto Z \quad (4.10)$$

In pair production, the photon is transformed into an electron-positron pair in a nuclear or electric field. Because of this, the energetic threshold is two electron restmasses, of 1.022 MeV. The electron will be registered as an event, and the positron will quickly annihilate with an atomic electron. If both are registered, the peak will appear at the initial gamma-ray energy, if not, we will have a single escape peak at  $E_\gamma - 511$  keV or double escape peak at  $E_\gamma - 1022$  keV. Probability increases with Z of detector material squared

$$\kappa \propto Z^2 \quad (4.11)$$

In addition, interaction via detector shielding occurs, which can lead to emission of characteristic X-rays from the absorbing medium (typically led). Also, since the shielding material is dense, most gamma-rays from Compton scattering are backscattered, and if scattered by more than  $120^\circ$  appears as a broad peak within 200-300 keV. In addition, an annihilation peak at ca. 511 keV is often present, and appears as either a result of pair production in the shielding, where only one gamma-ray will be detected (since they are emitted in opposite directions), or the possibility of annihilation of the positron of a  $\beta^+$ -emitter ([44] p. 34-35). Pileup is an effect which appears due to random summing which is due to possibility of two gamma-rays being detected simultaneously ([44] p. 33). Figure 4.4 shows an example of a gamma-ray spectrum for Ir05 ( $E_d \approx 21$  MeV) approximately 35 hours after end of beam on a logarithmic scale. The background at low energies is higher due to the multiple Compton continuum which are added together. In addition, the pileup effect can be seen on the high-end side of the spectrum.

Ionizing radiation statistics is based upon Poisson statistics, where the probability of observing N events is a discrete value

$$P(N) = \frac{\mu^N e^{-\mu}}{N!} \quad (4.12)$$

where  $\mu$  is the mean value, which is equal to the variance ( $\mu = \sigma^2$ ). This distribution is valid when the probability is small (decay probability small?) and the number of trials (number of decays?) are large ([10], p. 85). The distribution is not symmetric, but as the mean value increases, the peak approximates a Gaussian shape. Therefor the peak is assumed Gaussian with an exponential skew

towards lower energies which is caused by incomplete charge collection, along with a step function which takes the background into account. The area of the whole peak is net net number of counts which is necessary to obtain an activity in the foil. The statistical uncertainty arises from the Poisson statistics, and is large if net number of counts are low:

$$\sigma N_i = \sqrt{N_i} \quad (4.13)$$

Therefor, to reduce the statistical uncertainty, a relative uncertainty of less than 1% is preferred ( $\frac{\sigma N_i}{N_i} \frac{1}{\sqrt{N_i}} = 1\%$ ) The systematic uncertainty is in the detector, caused by a process called annealing. **write about it??**

In this work, the gamma-ray spectra were analyzed in FitzPeaks [45]. The mathematical algorithm inwhich Fitzpeaks in based on is SAMPO80 [46]. **Peak searching (SAMPO) using first and second order derivatives to search for peaks [44] (p.185)** In this algorithm, the peaks are assumed Gaussian joined with an exponential tale on both sides of the peak, so that the function and first derivative are continuous (**refer to Johns equation above if uncluding..**). The peak search utilizes the smooth second difference **derivative?**, which makes it a good algorithm for detecting small peaks on low background [46]. The peak areas are calculated by fitting the precalibrated modified Gaussian to the data with a weighted least squares formula using a parabolicbackground (**same citation but which page?**). Fitting intervals are determined automatically by the program. Peaks separated by less than 4 times the average fwhm are fitted together.

#### 4.4.2 Turning the number of counts in a gamma-ray peak to an activity

In general, the activity as a function of time takes the exponential form

$$A(t) = A_0 e^{-\lambda t} \quad (4.14)$$

where  $A_0$  is the activity at a reference time, and  $\lambda$  is the decay constant of a nucleus.

(From [24]) If a spectrum is counted at a delay time  $\Delta t_d$  after end of beam with a counting time  $\Delta t_c$  the total number of decayed products are

$$N_D = \int_{\Delta t_a}^{\Delta t_d + \Delta t_c} A(t) dt \quad (4.15)$$

Using equation 4.14 for  $A(t)$ , the solution to the above equation is

$$N_D = \frac{A_0}{\lambda} e^{-\lambda \Delta t_d} (1 - e^{-\lambda \Delta t_c}) \quad (4.16)$$

which again is equal to

$$N_D = \frac{A(t)}{\lambda} (1 - e^{-\lambda \Delta t_c}) \quad (4.17)$$

We can only know the number of decayed products which are detected. This is dependent on the efficiency of the detector, the intensity of the gamma-rays and the true number of decayed products

$$N_C = N_D \epsilon I_\gamma \quad (4.18)$$

where  $N_C$  is the number of observed/counted gamma-rays,  $\epsilon$  is the efficiency of the detector and  $I_\gamma$  is the gamma-ray intensity.

Thus, we can obtain an expression for  $A(t)$  after a delay time  $t$ :

$$A(t) = \frac{N_C \lambda}{\epsilon I_\gamma (1 - e^{-\lambda \Delta t_c})} \quad (4.19)$$

Since the activity as a function of time equals  $A(t) = A_0 e^{-\lambda t}$ , the above expression can be rewritten using  $A_0$  and the delay time  $\Delta t_d$

$$A_0 = \frac{N_C \lambda}{\epsilon I_\gamma (1 - e^{-\lambda \Delta t_c}) e^{-\lambda \Delta t_d}} \quad (4.20)$$

#### 4.4.3 Energy and peakshape calibration

Since the channel number is not necessarily analogous to the gamma-ray energy, the detectors needed to be calibrated. The gamma-ray calibration pointsources  $^{137}\text{Cs}$  ( $t_{1/2} = 30.08$  years [47]),  $^{133}\text{Ba}$  ( $t_{1/2} = 10.551$  years [48]) and  $^{152}\text{Eu}$  ( $t_{1/2} = 13.517$  years [49]) which were used can be seen in figure 4.5. The calibration sources are standard calibration sources, with precisely known gamma-energies and intensities, and by comparing the shift in the centroid of the peak in the spectrum to the true gamma-ray peak, a relationship can be developed. The gamma-lines which were used in the calibration are listed in table 4.2. The sources were counted so that the counting statistics were good, and that the strongest gamma-lines (which had more than 1% intensity) had a statistical uncertainty of less than 1%. Some of the detectors were also calibrated at multiple energies, which are listed in table 4.3. The relationship between channel number and energy fits a straight line quite well, using two calibration points, **but whether this is a good approximation is dependent on the integral linearity of the gamma spectroscopy system**

$$E = a + b \cdot c \quad (4.21)$$

where  $a$  is the slope of the line,  $b$  is the intercept and  $c$  is the channel number at that energy. ([44] p. 145, for both statements)

In FitzPeaks, peak shape and energy calibration was done, by first fitting the calibration spectra taken for each detector, and supplying energy and peak shape source files for the gamma-rays listed in the table for the specific source. This way, each detector was calibrated. For the peak shape, the program optimizes seven parameters; two background peaks, the peak height and location, the peak width, the distance from the peak centroid to the starting point of the exponential tail on either side ([46], p. 90). For the energy calibration, linear interpolation (**with two optimizing parameters, a,b**) on a linear scale was used. The minimization of the optimized parameters are performed using an iterative gradient method. **include more?? Calibration errors were added to the peak location and intensity errors to give the final result(???)** ([46], p. 94).

In addition to calibration spectra, long counts of the background for each detector was taken prior to irradiation, which was later used in the analysis, to verify if gamma-lines were background contaminated.

#### 4.4.4 Efficiency calibration

The efficiency of the detector is dependent on the shape and density of the detector ([44], p. 144), and is a very important parameter in the calculation of the end of beam activities from equation 4.20. The calibration was done using empirical data, and the same calibration point sources which were used in the energy calibration were used in the efficiency calibration, with the same gammas which are listed in table 4.2. The reference date for the sources is January 1st 2009, and the  $^{137}\text{Cs}$  measured 38.55 kBq,  $^{133}\text{Ba}$  measured 39.89 kBq and  $^{152}\text{Eu}$  measured 39.29 kBq, which can also be seen on figure 4.5. Solving Equation 4.20 for efficiency,  $\epsilon$ , the analytical efficiency as a function of gamma-ray energy and intensity is

$$\epsilon(E_\gamma) = \frac{N_C \lambda}{A_0 I_\gamma (1 - e^{-\lambda \Delta t_c}) e^{-\lambda \Delta t_d}} \quad (4.22)$$

where  $\lambda$  is the decay constant and  $N_C$  is the number of counts in the measured spectra, and  $\Delta t_d$  is the delay time since the reference date. The analytical efficiency gives one single value for the efficiency at energy  $E_\gamma$ , but a continuous function which gives the efficiency at any gamma-energy was desired. Several non-linear functions represents the efficiency as a function of energy in a gamma-ray detector. A model based upon Gallagher, W. J., Cipolla, S.J. (1974) which was developed for

Table 4.2: The calibration point sources along with gamma lines used in the calibration of the detectors. \* indicates that the value has been averaged over two peaks with similar energy, less than 1 keV. For the intensity its just added together.

$^{137}Cs$		$^{133}Ba$		$^{152}Eu$	
$E_\gamma$	$I_\gamma$	$E_\gamma$	$I_\gamma$	$E_\gamma$	$I_\gamma$
32.005*	5.63*	53.1622	2.14	121.7817	28.53
36.3405*	1.02*	80.9979	32.9	244.6979	7.55
661.657	85.10	160.6120	0.638	295.9387	0.440
		223.2368	0.453	344.2785	26.5
		276.3989	7.16	367.7891	0.859
		302.8508	18.34	411.1165	2.237
		356.0129	62.05	444.4853*	3.125*
		383.8485	8.94	503.467	0.1524
				586.2648	0.455
				678.623	0.473
				688.670	0.856
				719.353*	0.345*
				778.9045	12.93
				810.451	0.317
				867.380	4.23
				963.712*	14.65*
				1112.076	13.67
				1212.948	1.415
				1299.142	1.633
				1408.013	20.87

efficiency calibration of Si(Li) X-ray detectors [50, 51] was applied which takes the probability of penetration through the deadlayer of the detector and the probability of interaction in the detector volume into account

$$\epsilon(E_\gamma) = B_0 \cdot \underbrace{(e^{-B_1 E_\gamma^{B_2}})}_{\text{dead layer}} \underbrace{(1 - e^{-B_3 E_\gamma^{B_4}})}_{\text{interacting with volume}} \quad (4.23)$$

where  $B_i$  are optimization parameters. The Scipy Optimize Curvefit function [52] takes in the analytically calculated efficiencies and uncertainties calculated from equation 4.22, fits the values to the function represented in equation 4.23, and returns the optimal parameters  $B_i$  and the estimated covariance matrix, minimizing the  $\chi^2$ . The fit is uncertainty weighted, which means that data with low uncertainty will be weighted higher as "true" value. **The efficiency curve was optimized with gamma-ray energies from 30 MeV to 2500 MeV to broad range of gamma-ray energies. Since the lowest energy used is 32.005 keV and strongest one is 1408.013 keV, the energies down to 30 keV and up to 2500 keV are extrapolated, and has thus very large uncertainties in comparison to energies where the data optimizes the curve.** According to Mathew et. al. (2020), the use of canonical logarithmic polynomial gamma-ray efficiency calibration forms results in significant biases in efficiency for both the interpolated and extrapolated energies [51], which was the motivation behind using this model for efficiency. Since the optimizing parameters are highly correlated, the uncertainty in efficiency was estimated according to equation A.6. Figure 4.6 shows two different efficiency curves. The top figure shows the efficiency curve for detector 1 at a distance 30 cm from the detector surface, and the bottom figure shows the efficiency curve for detector 7 at a distance 5 cm from the detector surface. For the former, the curve follows the points around the peak very well. For the latter, the model has a harder time fitting the peak, which is due to the high uncertainty of the  $^{137}Cs$  peaks. It is clear that the fit weights the low-uncertainty points. One of the reasons that some of the points in detector 1 have large uncertainties is due to the distance from the detector surface. The two low-energy peaks of  $^{137}Cs$  also differs in comparison to each other. The lines which were used are X-rays, which are

Detector	Distance (cm)	Relative average uncertainty (%)
1	10	2.47
	30	2.27
2	10	1.94
	30	4.0
3	53	4.80
4	32	2.33
5	40	3.01
6	25	3.34
7	5	4.49
	10	2.69
	15	2.87
	18	4.41
	22	3.95
	30	4.19
	40	2.47
	50	4.28
	60	4.79

Table 4.3: The relative averaged uncertainties for each efficiency calibration. Detector 1-6 were the p-type IDM Ortec detectors with higher relative efficiency than detector 7 which was n-type Ortec GMX detector.

difficult to fit, and are relatively low in intensity. In addition, the gamma-ray energy region has a high slope in efficiency which makes it difficult to make a good fit. All the uncertainties which are remarkably higher than others have intensities of less than 1%. This could have been avoided by excluding these low-intensity gamma-lines, but since the fit is uncertainty-weighted, the number of lines remained. On both figures, the uncertainty is higher around the peak, and for detector 7 the uncertainty is increasing with energy. Figures 4.7 shows the relative uncertainty for each detector at each distance. As we can see for all detectors, the main contributions to uncertainty is where the functional fit is extrapolated, and around the efficiency peak, where the latter is especially evident in the plot of detector 1-6. The distance from the detector affects the uncertainty, which can be seen on detectors 1-6 also. This is however not the case for detector 7 at 40 cm, which is remarkably low, which can be due to the long count (??). The relative average uncertainty in each detector at a specific distance is listed in table 4.3,**drop relative average uncertainty?** The relative average uncertainty varies from 1.94-4.80% for detectors 1-6 and from 2.47-4.79% for detector 7. The overall values for detectors 1-6 are less, because of the higher absolute efficiency. These values only indicates that the uncertainty in efficiency might be a larger contribution to the total uncertainty than other detectors.

## 4.5 The irradiation

The irradiation of the target stack took place on February 26th 2019, and the activated foils were counted on high purity germanium detectors for a total of 4 weeks after end of beam. **In addition to this experiment, two other experiments took place, irradiating strontium with deuterons and a deuteron breakup experiment.** The target stack was subject to a 33 MeV incident deuteron beam, which can be seen in figure 4.8. The beamintegrator measured the beamcurrent on the first foil to be 128.5 nA.

When a target is irradiated, the activity of the product nucleus will increase until secular equilibrium is achieved, which is when the product rate and decay rate are constant. Hence it is not necessary to irradiate a target for more than 2-3 half lives.

. WHY WAS THE STACK IRRADIATED FOR ONE HOUR???

### The tuning the beam

Before irradiation, the deuteron beam was tuned to be ca. 1 cm in diameter. In addition, the experiments taking place simultaneously demanded a precise position of the beamspot since the target size was on the order of the same order of the beamspot. The beam spot was first visualized using a ca. 2.5 cm thick borosilicate glass, painted with a mixture of phosphor powder and vacuum grease (so that the paint does not evaporate as the tube was pumped down to vacuum). When ionizing radiation strikes the phosphor, the phosphor is excited and emits light in the de-excitation, called phosphorescence. The glass was placed on the end of the beam tube. With a camera placed in cave 0, from the control room, the beam spot could be visualized, and could be steered to be centered and ca. 1 cm in diameter. The beamspot can be visualized in figure 4.9 (left), and the borosilicate glass placed on the end of the beam tube can be seen in figure 4.9 (right). Secondly, the beam had to be constant over the target stack, i.e. not diverge or converge. Gafchromic films were placed in the front and the back of the target holder, separated by the spring. The films were exposed for a brief second, and the blue spot on the developed film was evaluated. This was done until the beamspot was good both in the front and in the back of the stack. The Gafchromic films after direct exposure can be seen in figure 4.10 in the target holder.

The beam efficiency transmission was calculated by measuring the current at the Faraday cup right after the cyclotron vault (BS-02) and right before cave 0 (FC-01). BS-02 was measured to be 420 nA and FC-01 was measured to be 285 nA. This gave beam efficiency of transmission of 67%

### Irradiation of the target stack

The irradiation lasted for one hour. The number of charges collected?? was registered off the current integrator on the electrically isolated beamline, and registered evenly to ensure that the beamcurrent was more or less constant throughout the irradiation. After exactly one hour, the beam integrator read of  $I\Delta t = 2314 \text{ C}$ , with full-scale amperes being  $2 \cdot 10^{-7} \text{ A}$ . The average beam current hitting the front of the stack was thus

$$\frac{2314 \cdot 2 \cdot 10^{-7}}{3600} = 128.5 \text{ nA} \quad (4.24)$$

Before the beam was turned on, the beam tube had to be pumped down to a vacuum, to not attenuate the beam. The targetholder was placed in the end of the electrically isolated beam tube. Figure 4.11 shows how the targetholder (left) was placed in the end of the beam line (right). About ten minutes after end of beam, cave 0 was opened, and the targets were sealed in plastic bags to avoid contamination. The iridium foils was counted from 15 minutes after end of beam on detector 7, and the other foils following up shortly after. All the foils were counted for ca. four weeks following end of beam on the various detectors, with short counts in the beginning to have good statistical data for the short-lived activities, and longer and longer counts as the shorter and medium-lived activities decayed out, to have good statistics. The counts were done as jobscripts in the beginning, so that the same foil was measured multiple times, and the gamma-lines were observed multiple times over short counts rather than one long count. The reason why the foils were counted multiple times was to reduce the statistical uncertainty, and in addition make sure that the products with similar gamma-lines but different half-lives were observed independently if possible. Since the detectors were calibrated at various distances, the deadtime of the foils right after end of beam could be reduced by increasing the distance from the detector, however, as high as 16-22% deadtime was present, but reduced to less than 5% within a cooling time of ca. 1 day after end of beam double check, but on quick overview this seemed right.  $^{193m}\text{Pt}$  has one single weak gamma-line at 135.5 keV (0.11%). In addition, it is located at the shoulder of  $^{192}\text{Ir}$  at 136.39 (0.199%) [16, 53]. The half-life of  $^{192}\text{Ir}$  is long, and it was important to make sure that the two peaks were identified independently. Due to the relatively long half-life of  $^{193m}\text{Pt}$ , and the weak gamma-ray, it was made sure that the single gamma-line was observed within a few days after end of beam, when the counts were longer. In addition the short-lived monitor reactions  $^{\text{nat}}\text{Cu(d,x)}{^{62}\text{Zn}}$  ( $t_{1/2}=9.193 \text{ h}$ ),  $^{\text{nat}}\text{Cu(d,x)}{^{63}\text{Zn}}$  ( $t_{1/2}=38.47 \text{ m}$ ) and  $^{\text{nat}}\text{Ni(d,x)}{^{61}\text{Cu}}$

( $t_{1/2}=3.339$  h) [54–56] was also made sure that was observed in each single foil, in addition to the other longer-lived monitor-radionuclides.

### Intensity profile of the beam

After irradiation, Gafchromic film were attached to the activated stainless steel in the front and the back of the stack, to obtain a spatial intensity profile of the beam. The activated film attached to the Gafchromic film can be seen in figure 4.12. The radius of the activity from stainless on gafchromic film was used in the imaging process program ImageJ-1.52k, which is developed by the National Institutes of Health and the Laboratory for Optical and Computational Instrumentation [57]. The Gafchromic films were scanned alongside a ruler for scale comparison. Since the images are divided into pixels, a 3 (why 3cm?) cm line segment was drawn alongside the ruler to set the scale to pixels/cm in the program. The intensity over the developed film was obtained by inverting the scanned image, and drawing a line segment along the beam spot that created a position dependent intensity array. The intensity profile can be fitted to a Gaussian, which is shown example-wise in figure 4.13, which is the horizontal beam profile in the front and the back of the stack. In the assumption that the beam was underfilled, it was important to build confidence in that the beamspot was ca. 1 cm in diameter, which was done estimating the full width half maximum of the Gaussian profile. The FWHM over SS1 was 1.2017 cm horizontally ( $\sigma^2 = 0.2604 \text{ cm}^2$ ) and 1.1420 cm vertically ( $\sigma^2 = 0.2352 \text{ cm}^2$ ). The FWHM over SS2 was 0.6706 cm horizontally ( $\sigma^2 = 0.0811 \text{ cm}^2$ ) and 0.5783 cm vertically ( $\sigma^2 = 0.0603 \text{ cm}^2$ ).

Normally the beam broadens throughout the stack due to scattering. As we can see, this not the case, since the beam is stopped in the targetstack, and therefor we do not know how much the beam truly scatters. This gives a higher uncertainty. The stainless steel (which consist of ..) has fast decay time. However since it emits beta-particles, the radius will slightly increase, and the true beam spot is slightly smaller. Thus the estimated FWHM values for SS1 seems to be within the criterion for underfilled targets.

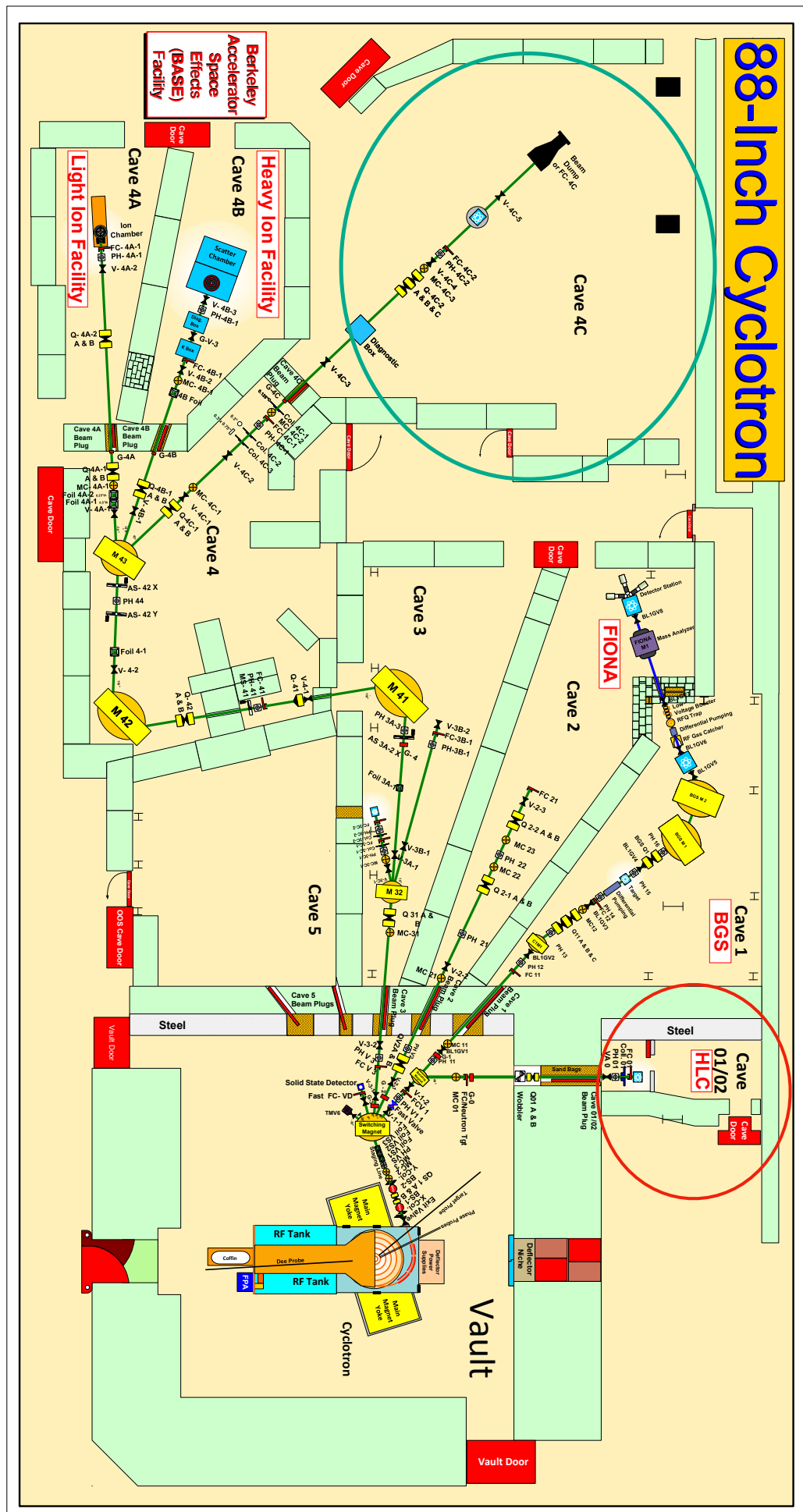


Figure 4.2: An overview of the 88" Cyclotron facility. The facility have several isolated beamlines that can be used for irradiation in the experimental caves. The irradiation of the target stack took place in cave 01/02 (red circle), while some of the detectors used in the gamma-rays spectroscopy was located in cave 4C (green circle) which is no longer used as an irradiated chamber. Bending magnets are used to steer the beam in the cyclotron vault, and focusing quadrupole magnets are used to focus the beam in the cyclotron vault.

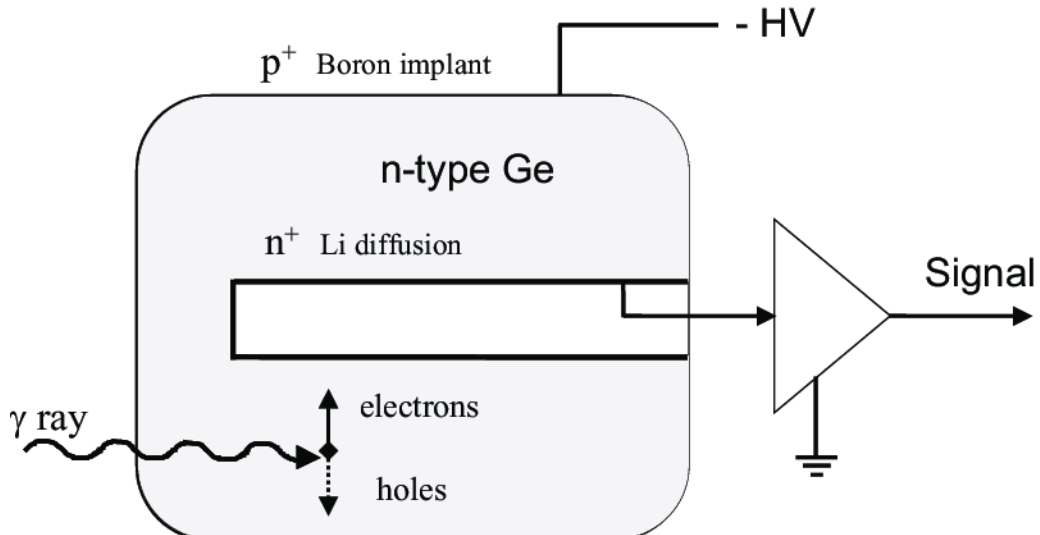


Figure 4.3: Figure shows a n-type germanium detector. Since the material is n-type, a potential arises around the boron implant (outer surface). where a p-n junction is created around the boron implant (outer surface). Figure is from [43].

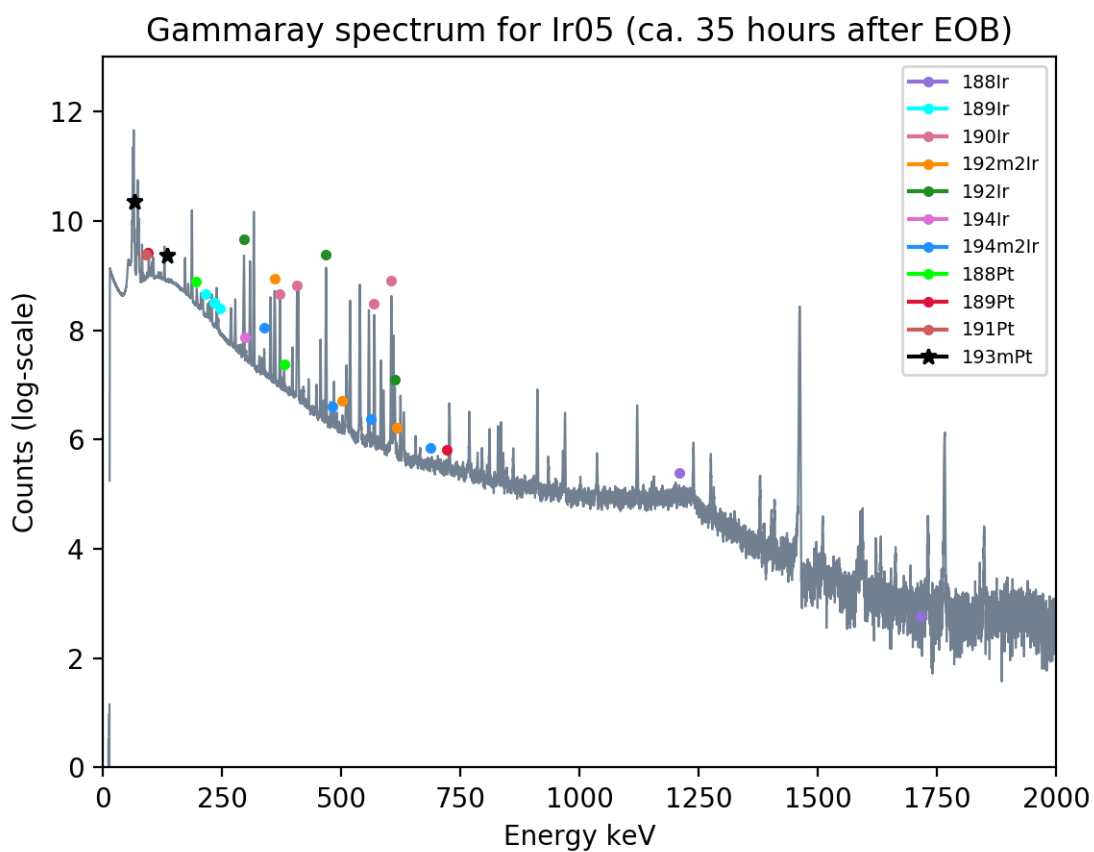


Figure 4.4: Gamma-ray spectrum for Ir05 (with deuteron energy ca. 21 MeV) taken approximately 35 hours after end of beam. Nuclei does not necessarily represent what is present in the spectrum, but where the peak would have been. Hard to include all since there are different decay times.



Figure 4.5: The calibration point sources that were used in the efficiency calibration of the detector.  
( $^{22}\text{Na}$  was later excluded because it was difficult to obtain good efficiency curves with )

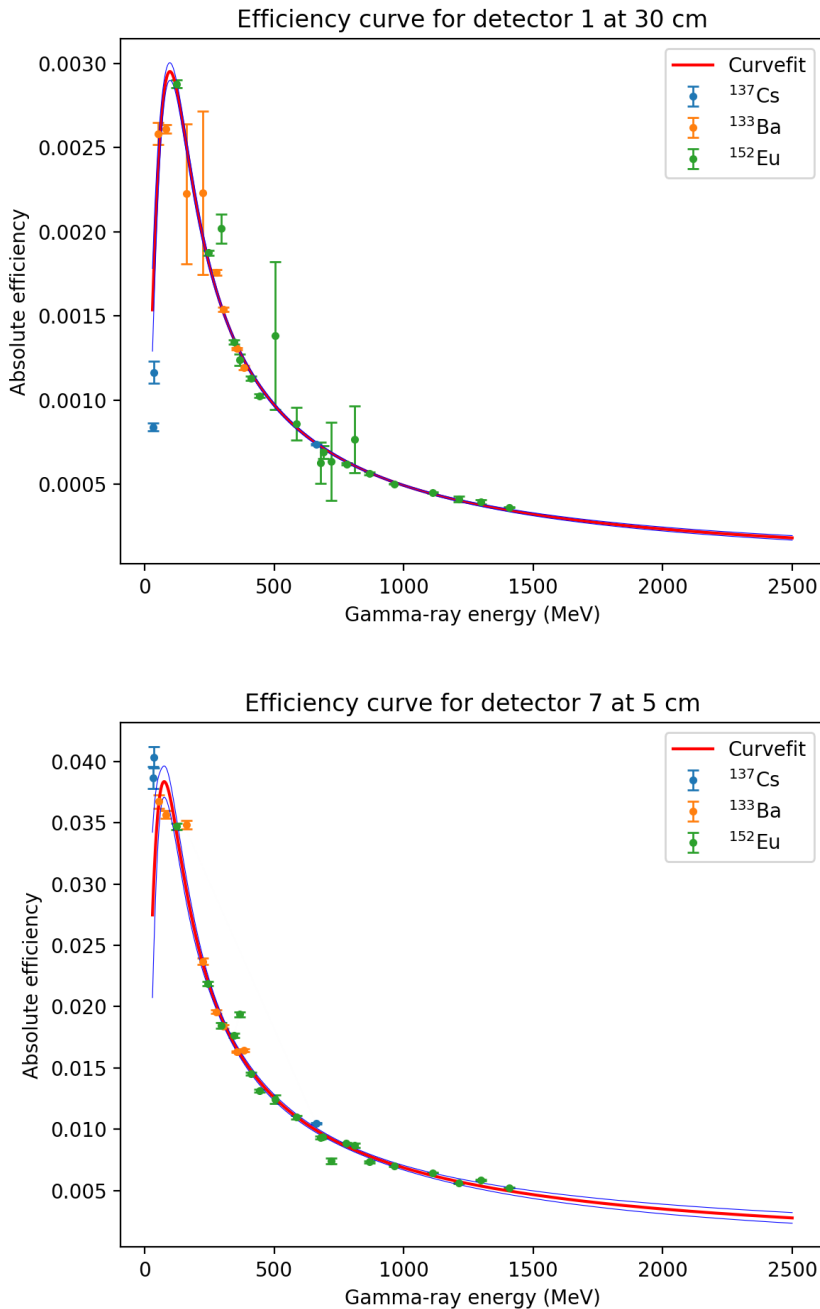


Figure 4.6: Two examples of efficiency curves. **top:** The efficiency curve of detector 1 at 30 cm which is located in cave 4C. **bottom:** The efficiency curve of detector 7 at 5 cm is located in a separate room and had led shielding.

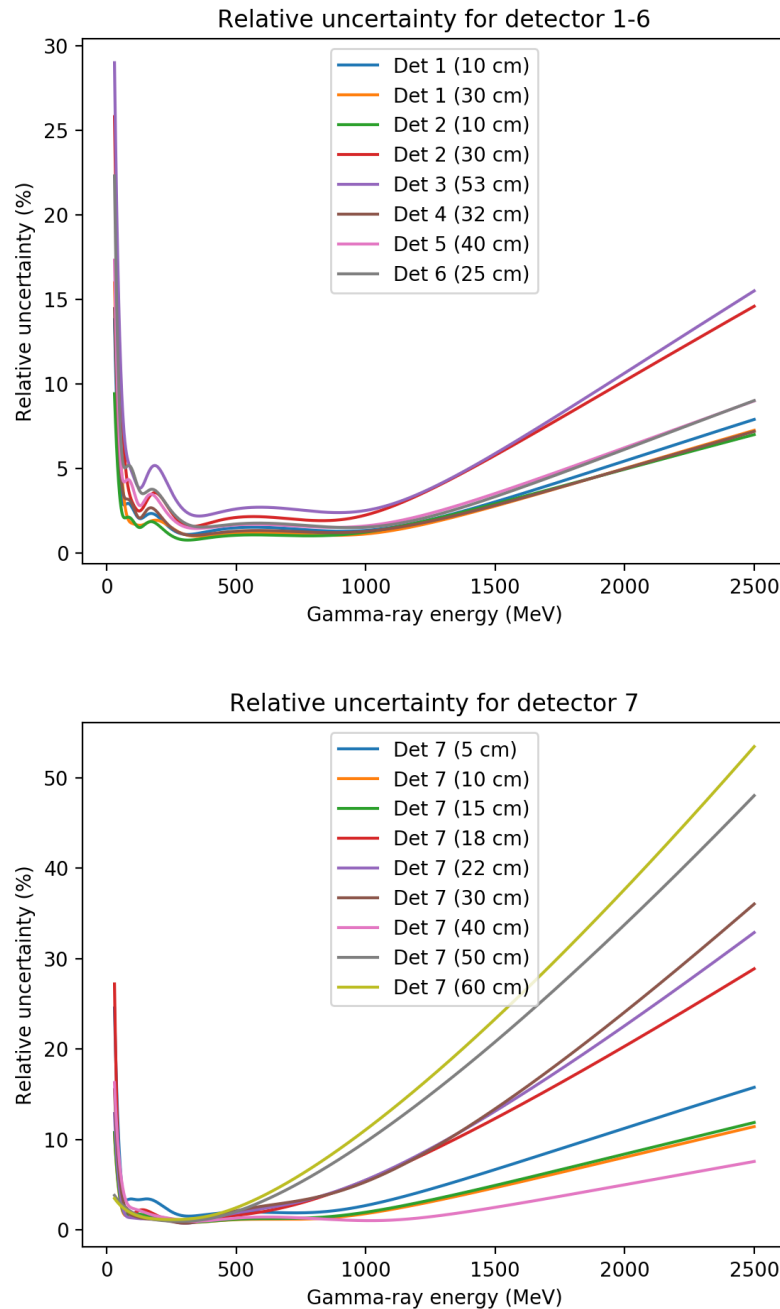


Figure 4.7: The relative uncertainty in efficiency for each detector. **Left:** Relative uncertainty for detectors 1-6 (p-type IDM ORTEC). **Right:** Relative uncertainty for detector 7 (n-type ORTEC GMX).

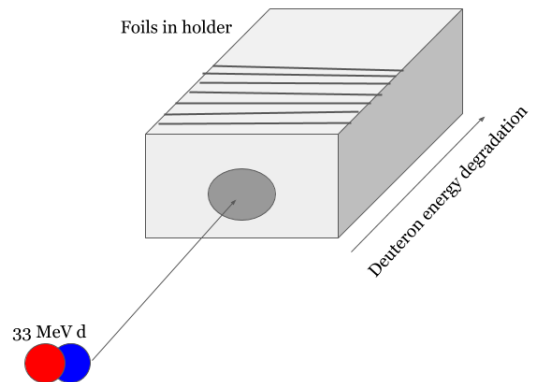


Figure 4.8: The fundamental idea of the experiment where a stack of targets are placed in a target holder, and irradiated with accelerated 33 MeV deuterons. As the energy degrades through the beam stack, it is possible to have multiple cross section measurements at different energies.

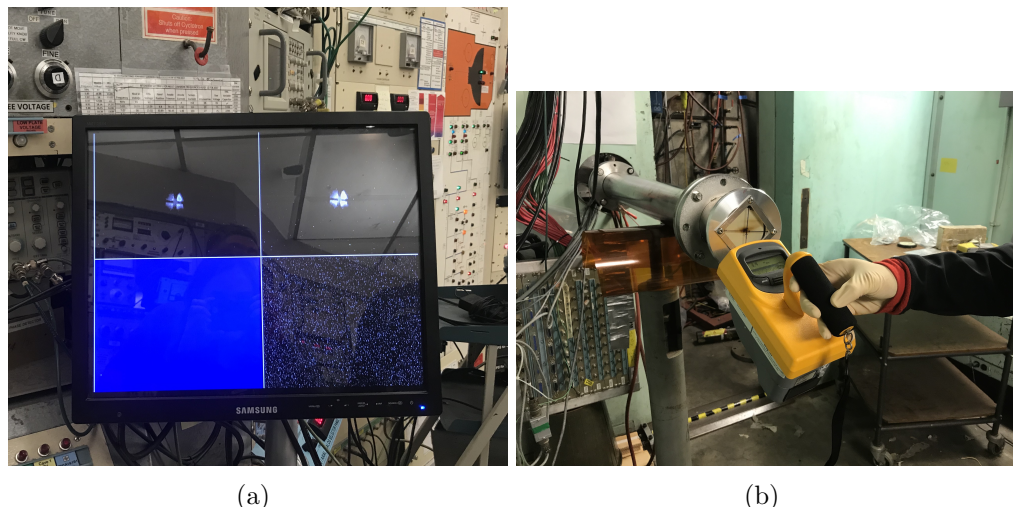


Figure 4.9: The figure shows the beamspot which could be visualized from the control room, and the borosilicate glass placed on the end of the beam tube. The dose present after the beam was on was always measured.

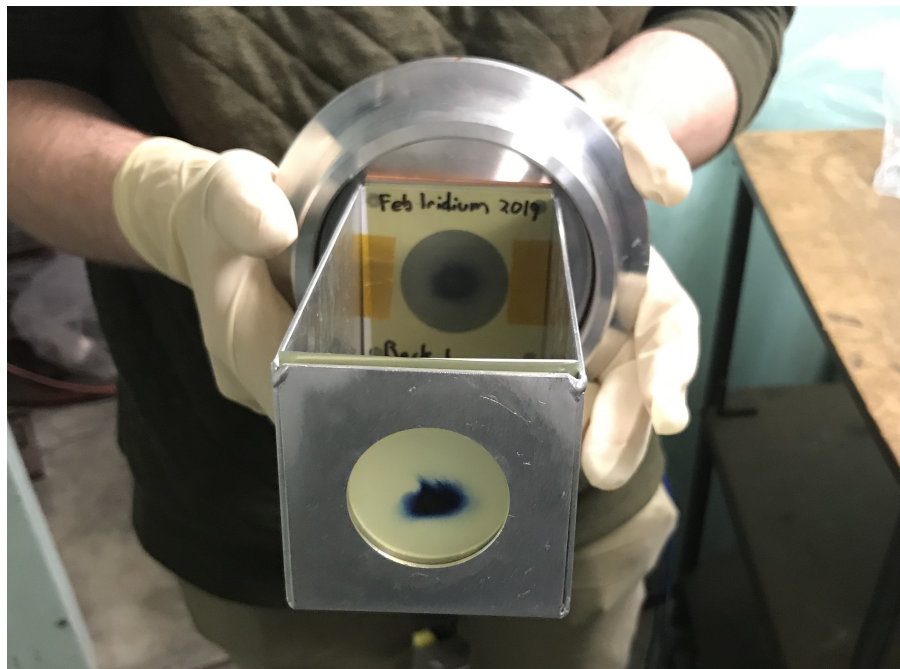


Figure 4.10: The gafchromic films were exposed for a brief second



Figure 4.11: The figure shows the target stack was placed in the beamline. **Left:** The targets were placed in a 6061 aluminum alloy targetholder with a hollow center for the beam to pass through. The hollow spring kept the targets on a finite position throughout the irradiation. **right:** The target holder was placed in the electrically isolated beamline.

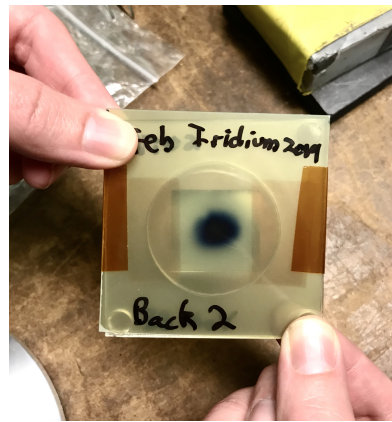
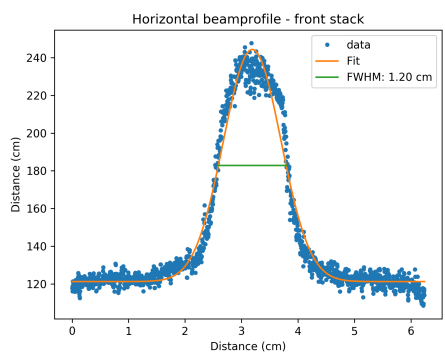
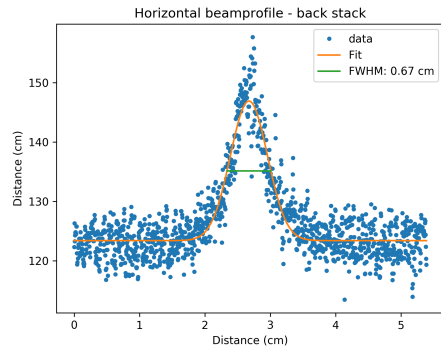


Figure 4.12: The gafchromic film on the activated SS1 foil.



(a) Horizontal intensity profile of SS1



(b) Horizontal intensity profile at SS2

Figure 4.13: Figure shows the intensity profile of the deuteron beam in the front and in the back of the stack horizontally.



# Chapter 5

## Analysis

The equation which is used to find the reaction cross section of a product nucleus is given in equation 3.6,

$$\sigma(E) = \frac{A_0}{N_T \Phi(E)(1 - e^{-\lambda t_{\text{irr}}})}$$

where  $A_0$  is the end of beam activities which are described in section 5.1,  $N_T$  is the number of target nuclei, which is calculated the areal density measured in table 4.1,  $\Phi(E)$  is the deuteron beam current which is described in section 5.4.  $(1 - e^{-\lambda t_{\text{irr}}})$  accounts for the decayed products during the irradiation time, where  $\lambda$  is the decay constant for the product nucleus and  $t_{\text{irr}}$  is the one hour long irradiation time. The final cross section results are represented in the next chapter.

### 5.1 Analyzing the gamma-ray spectra

The gamma-ray spectra were analyzed in FitzPeaks [45], as there were more than a total of 400 spectra and it would take too long time to do this independently. As described in section 4.4.3, the method in which the SAMPO80-algorithm [46] **not 100% sure about citation double check that it is the correct one** searches for peaks are through the second derivative. The peak areas were calculated by fitting **the precalibrated modified Gaussian to the data with a weighted least squares formula using a parabolic background. How was the net area calculated and the uncertainties?** The fitting parameters were determined automatically by the program, and peaks separated by less than 4 times the average full-width half-maximum are fitted together [46]. If the peaks were lying closer together, the program asked if you wanted to add another peak, in which had to be evaluated as shown in figure 5.1, where it is clear that there is an additional peak due to the high number of counts on the low energy side of the 765 keV peak.

For each spectra, a report file containing peak energy, centre channel, full width half maximum, significance, goodness of fit, peak area and uncertainty in peak area, gammas per second and uncertainty in gammas per second and a background estimation for each peak was provided. The parameters which were used in the analysis was the peak energy for identification, the peak area  $N_C$  which was used in the activity equation 4.20 and estimation of efficiency, and uncertainty in peak area. The gammas per second (also called countrate) was used to get an indication of the rate of gammas, which were used as a critical tool to evaluate background contamination in a peak, by comparement to background spectra.

Figure 5.2 shows the X-ray region (upper) and the gamma-ray region (lower) of  $^{193m}\text{Pt}$  **which spectra?** taken approximately .... hours after end of beam. From the lower figure, it is clear that 135.5 keV (0.11 %) lays on the shoulder of the long-lived  $^{192}\text{Ir}$  ( $t_{1/2}=73.829$  d) 136.39 keV (0.199%) [16, 53].

A matlabscript written by Voyles, A. (2019) was used to loop over all report files for each single spectra in each foil. Gamma-energies with less than **0.5 (doublecheck)** keV in difference were added and averaged, which can be seen on figure 5.3 where the channel number is listed on the x-axis and the gamma-ray energy is listed on the y-axis. The result is a staircase where the energies within the tolerance are averaged. This gave a list of gamma-ray energies for each target foil type, one for iridium, one for nickel, one for copper and one for iron. Each of the gamma-lines were identified

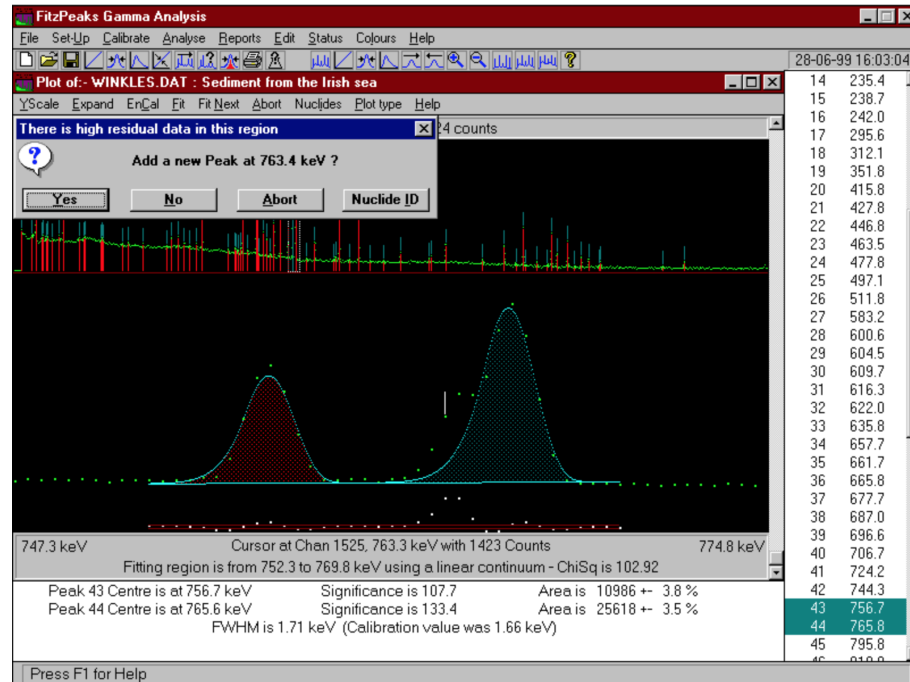
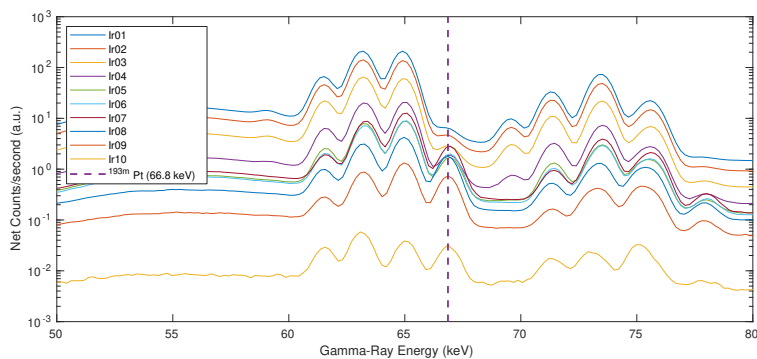
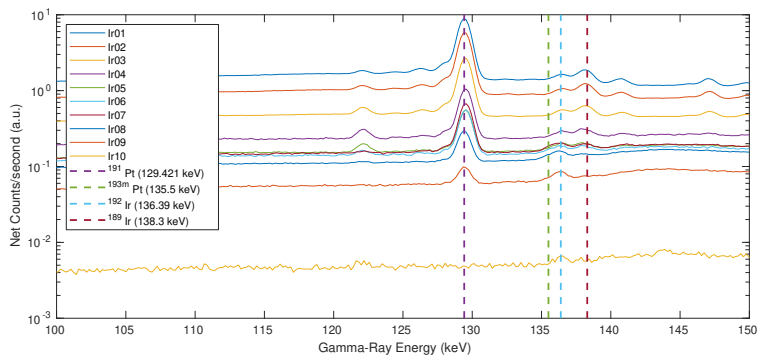


Figure 5.1: from:<http://www.jimfitz.co.uk/pk1fsz.htm>



(a) X ray plot of <sup>193m</sup>Pt.



(b) Gammalplot of <sup>193m</sup>Pt

Figure 5.2: Which spectra are these??

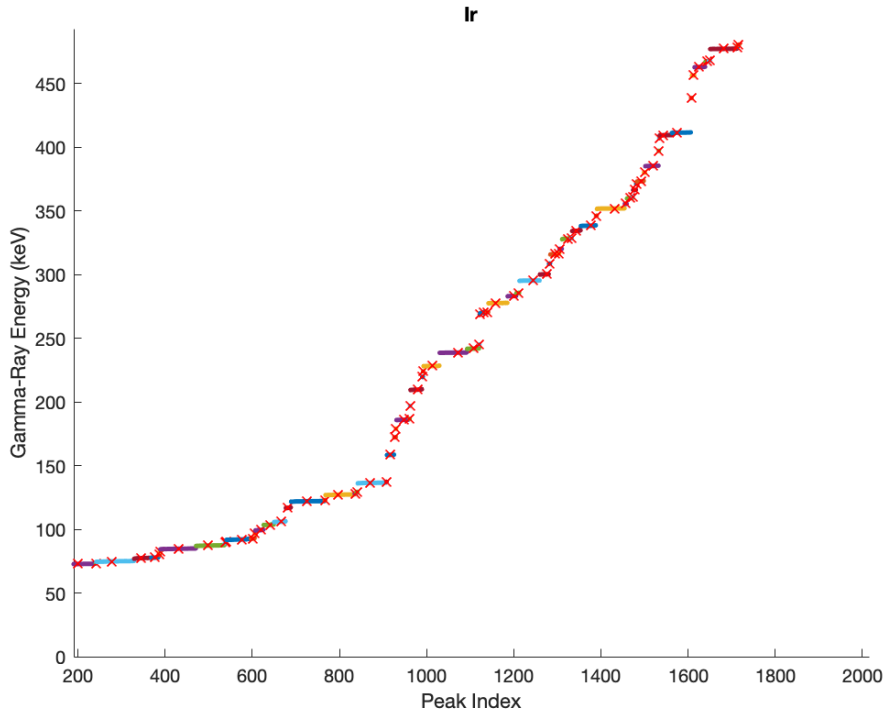


Figure 5.3: Zoomed staircase for energies between 0 and ca. 500 keV. Shows how the gamma-rays within a tolerance of 0.5 keV were averaged. Each "staircase" represents one gamma-ray energy which was used for identification.

manually using the nnndc-database (Nudat-2.8) [20], going through possible reactions based on Q-value, where the Q-value calculator from NNDC was used [58]. If more than one nucleus fed into the same gamma-ray energy within a tolerance of 1 keV, then the peak was not used if there were other possible gamma-ray energies present. If not, the half-lives were compared, and if there was a large difference, only early spectra or very late spectra were used when the activity of the other was not present. In addition, peaks which were contaminated with background radiation was also not used, unless the countrate was very small in comparison to the count-rate of the peak. If it had to be used, the method for background subtraction is described below in subsection 5.1.1.

For each nucleus identified, the gamma-rays from nnndc (listed in tables B.1, B.2, B.3 and B.4 for nickel, iron, copper and iridium respectively) along with half-life, intensity and uncertainty in intensity were gathered.

### 5.1.1 Background subtraction

In a few number of cases, background subtraction was necessary due to the presence of some nuclei in the background, which was only problematic for the detectors located in cave 4C. Nuclei of cobalt was in particular present in the background. The general rule of thumb was only to use background subtraction when all gamma-lines of the nucleus was contaminated with a count-rate of the same order, due to the raise in uncertainty. If not, the line was avoided.

The count-rate is defined as the number of counts divided by the live time of the spectrum, in units counts/second

$$C = \frac{N_C}{\Delta t_{\text{live}}} \quad (5.1)$$

The number of true counts is the sum of the true gammas and the background

$$C_{\text{true}} = C_{\text{obs}} - C_{bg} \quad (5.2)$$

The count-rate in the background spectra are constant, which here is denoted as  $C_{bg}$ . The observed count-rate is thus the number of true counts divided by the live time of the spectrum and the background count-rate on the detector. From equation 5.1, the number of counts are the count-rate multiplied by the live time, which gives

$$N_{\text{true}} = N_{\text{obs}} - (\Delta t_{\text{live}} C_{bg}) \quad (5.3)$$

## 5.2 Estimating the end of beam activities

The end of beam activities were estimated by extrapolating backwards in time with the measured activities at various time points after the end of beam. The activities measured in each spectrum as a function of time since end of beam was calculated using equation 4.19 along with a self-attenuation correction:

$$A(\Delta t_d) = \frac{N_C \lambda}{\epsilon I_\gamma (1 - e^{-\lambda \Delta t_d}) e^{-\mu \rho \Delta r / 2}} \quad (5.4)$$

where  $\mu$  is the photon attenuation coefficients from the XCOM photon cross section database [59], and  $\rho \Delta r$  is the areal density of the foil. The gammas which were used are listed in tables B.2, B.1, B.3 and B.4 for iron, nickel, copper and iridium respectively. The gamma-ray self-attenuation (which is typically less than 0.2 % [33]) correction is based on the assumption that all activity that is made is located midway in the foil thicknesses. In reality however, the activity profile will follow the same shape as the excitation function over the energy range that expands over the foil, **if we assume that the stopping power dE/dx=0 which is a good estimation for thin foils less than 100 mg/cm<sup>2</sup>??** (since activity and cross section are proportional). We do not know the excitation function ahead of time, and the excitation function does not change much either, since the foil thicknesses are so thin. So instead, this simplification is done, assuming that the average attenuation is through half of the foil thickness.

In a matlabscript written by Voyles, A. S (2020), the gamma-ray energies used, and intensity, uncertainty in intensity and half-life were assigned to each nucleus. Each foil type and foil number was looped over to see if the observed gamma-ray within a tolerance of 0.5 keV was registered, and with the number of counts, uncertainty in number of counts, the time since end of beam, the areal density and mass attenuation correction, and the efficiency which was dependent on which detector, the activity at each observed time point since end of beam was calculated according to equation 5.4. The result was an output file for each foil with the calculated activity according to equation 5.4 with hours since end of beam. The output files were read into a separate program for calculation of the end of beam activities. The uncertainty in each measured activity was the quadruple sum (calculated according to equation A.13) for the number of counts, the efficiency, the intensity and half-life (provided by the IAEA database [20]) and the uncertainty in the areal density for each foil. The main contributing factors of the uncertainty was the number of counts in the peak and the uncertainty in efficiency calibration which varied as a function of energy (figure 4.7). Some of the measured activities were nonphysically large, and error searches to find the source of high activity was done for each product nucleus. **It appeared that the efficiency for detector 2 at 30 cm had an efficiency which can be too high that contributes to those values.** If the values were larger with several orders of magnitude, than the rest of the calculated activities, and the error-search did not give any clarity of what was causing the high activities, the points were not used in the analysis.

The activity curves are based on Bateman equations [37]. The decay curve of single a radioactive nucleus takes an exponential form

$$A(t_d) = A_0 e^{-\lambda t_d} \quad (5.5)$$

where  $t_d$  is the delay time (here since end of beam),  $A_0$  is the activity right after end of beam. For multiple decay, Bateman equation is used describing the activity in nucleus n of the decay chain

$$A_n = \lambda_n \sum_{i=1}^n \left[ \left( A_{i,0} \prod_{j=i}^{n-1} \lambda_j \right) \cdot \left( \sum_{j=i}^n \frac{e^{-\lambda_j t}}{\prod_{l \neq j} (\lambda_l - \lambda_j)} \right) \right] \quad (5.6)$$

where  $A_n$  is the activity of nuclei n in the decay chain, with the corresponding decay constant  $\lambda_n$ . The equation sums over all nuclei in the decay chain.  $A_{i,0}$  is the initial activity of nucleus i, and j is the nucleus which is feeding into nucleus i. In this work, decay chains of single and two-step ( $n=1,2$ ) were sufficient. For two-step decay, equation 5.6 takes the form

$$A_d(t) = \lambda_n \left[ A_{p,0} \lambda_1 \frac{(e^{-\lambda_1} + e^{-\lambda_d})}{\lambda_p - \lambda_d} + A_{d,0} e^{-\lambda_d t} \right], \quad \text{two step decay} \quad (5.7)$$

where subletter p is shortened for parent is the parent nucleus, and subletter d is shortened for daughter. The parent activity is calculated from single step decay.

The extrapolation was done using the scipy optimize curvefit function [52], where the activities and the uncertainties in activities calculated from equation 5.4 were fitted to the decaycurve, minimizing the  $\chi^2$ , with the end of beam activity serving as optimizing parameter. The function returns the optimal parameters along with the estimated covariance matrix of the optimal parameters. For the cases where there was twostep feeding, but the parent nucleus did not emit observable gamma-rays, twostep decay with both the end of beam activities of the daughter and the parent served as optmizing parameters was used. For the two former cases, there was only one optimizing parameter, and the uncertainty was estimated using the squareroot of the covariance matrix (V).

$$\delta_{A_0} = \sqrt{V} \quad (5.8)$$

For the latter, the two optimizing parameters are correlated, and equation A.6 had to be used to estimate the uncertainty.

Figure 5.4 shows three examples of three different activity curves; one step decay for  $^{193m}\text{Pt}$  ( $t_{1/2}=4.33$  days), two step decay decay for  $^{58}\text{Co}$  ( $t_{1/2}=70.86$  days) with feeding from the isomer  $^{58m}\text{Co}$  ( $t_{1/2}=9.10$  hours), which had to be fitted using two optimizing parameters, and twostep decay of  $^{56}\text{Co}$  ( $t_{1/2}=77.236$  d) with feeding from  $^{56}\text{Ni}$  ( $t_{1/2}=6.075$  d) using the activity of  $^{56}\text{Ni}$  and the optimized parameter of  $^{56}\text{Co}$ . The uncertainty bands are large for  $^{58}\text{Co}$ , as the twostep decay with no observed parent contributes to a higher uncertainty.

### 5.3 Monitor reactions

The requirement of monitor reaction-data used to estimate beam current or flux for beam-monitor reactions is well-characterized cross sections, provided by the IAEA Coordinated research Project on "Nuclear Data for Charged-particle Monitor Reactions and Medical Isotope Production" where an international team between 2012-2017 worked to evaluate a limited number of cross section data which was in well-agreement [36] for recommended cross sections used to estimate monitor beam current. The recommended curves are interpolations over the recommended data, fit to an analytical approximation based on the ratio of two polynomials, with uncertainties obtained using the co-variance matrix, where the "full diagonal form represents a dataset in which each point possesses independent uncertainty" [36], p. 344. In addition, a systematic uncertainty of 4% was added. In addition to yielding precise cross section measurement as a function of beam energy, it was important that the neutron originating from deuteron break-up did not cause the induced activity for monitor reactions to increase, giving a higher beam energy than the true one (along with break-up protons but because of the positive charge, it is stopped quickly). For the reactions, the only possible neutron induced reactions are from  $^{56,58}\text{Co}$ , but analyzing the Ni-monitor foil in the back of the stack, there was no evidence of these two reactions, so that impact was not .....

The activity for each monitor-reaction was obtained by using the gamma-lines listed in table 5.1. More gamma-lines were included than the recommended listed [36]. In the back-propagation fit of

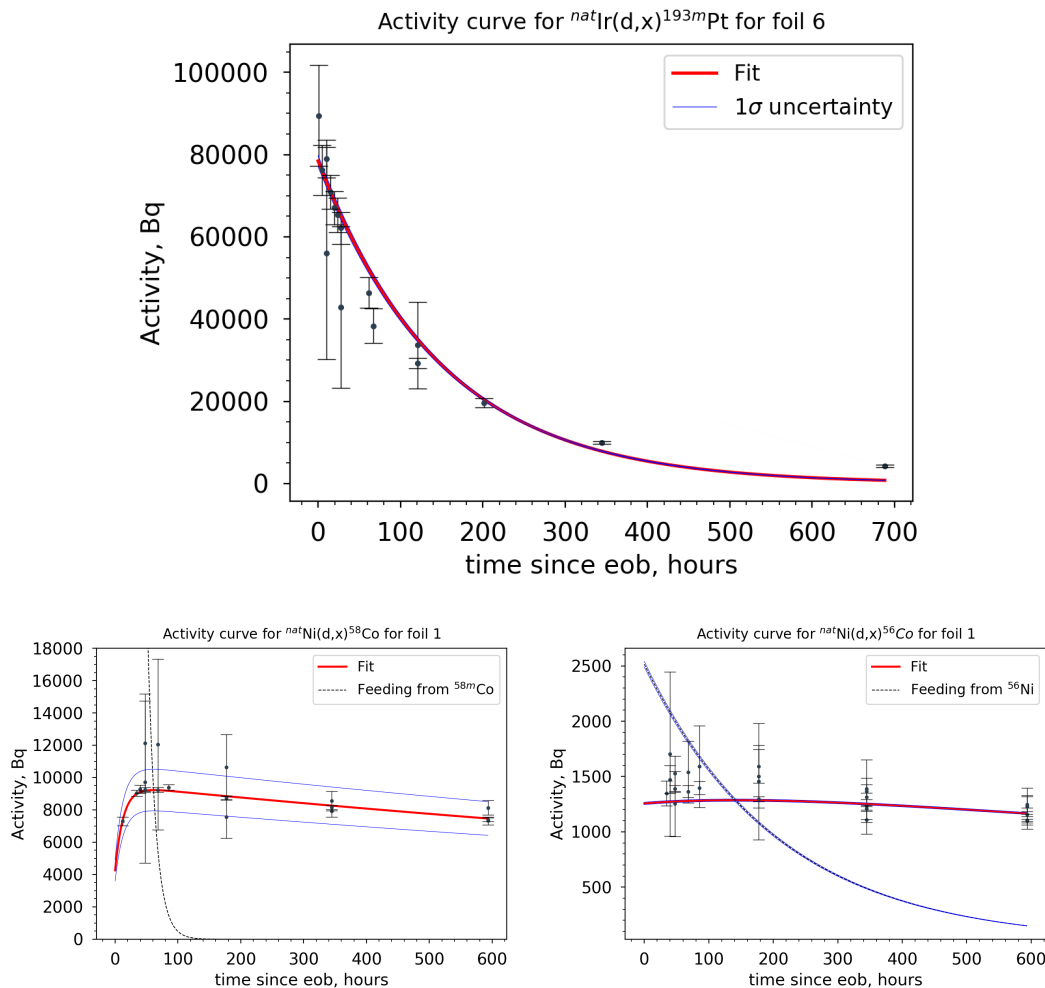


Figure 5.4: Examples of three activity curves. **Top:** Onestep decay for  $^{193m}\text{Pt}$  ( $t_{1/2}=4.33$  days), extrapolated with equation ???. **Bottom left:** Twostep decay for  $^{58}\text{Co}$  ( $t_{1/2}=70.86$  d) with feeding from the isomer ( $t_{1/2}=9.10$  h, IT:100%). The curve was extrapolated using twostep decay (equation 5.7) with both daughter and parent as optimizing parameters. **Bottom right:** Twostep decay for  $^{56}\text{Co}$  ( $t_{1/2}=77.236$  d) with feeding from  $^{56}\text{Ni}$  ( $t_{1/2}=6.075$  d,  $\epsilon$ :100%).

activities, more data gives a better statistical precision. However, some of the activities at time points after end of beam got calculated specific gamma-lines had nonphysically high activity in comparison to the other measured. These were not used and excluded from the back-propagation fit.

Table 5.1: The table shows an overview of the gamma-lines used to estimate the activation in each foil at the end of beam. Nuclear data from: [54–56, 60–62].

Monitor reaction	Half-life	Gamma-lines (keV)	Intensity (%)	Useful beam-energies(MeV) [36]
$^{nat}\text{Fe}(\text{d},\text{x})^{56}\text{Co}$	77.236 d	263.434 486.55 733.514 787.743 846.770 852.732 896.510 977.372 996.948 1037.843 1140.368 1159.944 1175.101 1198.888 1238.288 1335.40 1360.212 1771.357 1963.741 2015.215 2034.791 2212.944 2276.131 2598.500	0.0220 0.0540 0.191 0.311 99.9399 0.049 0.073 1.421 0.111 14.05 0.132 0.094 2.252 0.049 66.46 0.1224 4.283 15.41 0.707 3.016 7.77 0.388 0.118 16.97	10-50
$^{nat}\text{Ni}(\text{d},\text{x})^{56}\text{Co}$ (cum)	77.236 d	787.743 846.770 977.372 1175.101 1963.741 2015.215 2034.791	0.3111 99.9399 1.421 2.252 0.707 3.016 7.77	5-50
$^{nat}\text{Ni}(\text{d},\text{x})^{58}\text{Co}$ (cum)	70.86 d	-1823.8 6084.9 -1735.3 -12331.0 -28826.2	810.7593 863.951 1674.725	5-50

<sup>nat</sup> Ni(d,x) <sup>61</sup> Cu	3.339 h	282.956 373.050 529.169 588.605 625.605 656.008 816.692 841.211 902.294 1032.162 1073.465 1132.351 1185.234 1446.492	12.2 2.1 0.38 1.17 0.040 10.8 0.31 0.21 0.083 0.043 0.033 0.090 3.7 0.045	3-50
<sup>nat</sup> Cu(d,x) <sup>62</sup> Zn	9.193 h	40.85 243.36 246.95 260.43 304.88 394.03 548.35 596.56 637.41	25.5 2.52 1.90 1.35 0.29 2.24 15.3 26.0 0.25	15-50
<sup>nat</sup> Cu(d,x) <sup>63</sup> Zn	38.47 m	449.93 669.62 962.06	0.236 8.2 6.5	8-50
<sup>nat</sup> Cu(d,x) <sup>65</sup> Zn	243.93 d	1115.539	50.04	5-50

—c—c—c—c—c—

## 5.4 Deuteron beam current and energy assignment

The beamintegrator measured a current of 128.5 nA in front of the beam stack. However in order to have precise cross section measurements, the nominal beam current in each foil was calculated. As the beam loses energy throughout the stack via collisions, the deuteron beam will have a certain broadening due to the small angle deflections. The IAEA recommended monitor reactions <sup>nat</sup>Ni(d,x)<sup>61</sup>Cu, <sup>56,58</sup>Co, <sup>nat</sup>Cu(d,x)<sup>62,63,65</sup>Zn and <sup>nat</sup>Fe(d,x)<sup>56</sup>Co [36] were used to obtain a weighted average beam current in each foil solving equation 4.20 for beam current  $\Phi$ :

$$\Phi(E_d) = \frac{A_0}{N_T \sigma(E_d)_{\text{mon}} (1 - e^{-\lambda \Delta t_{\text{irr}}})} \quad (5.9)$$

where the units are deuterons per second,  $E_d$  is the deuteron energy (MeV),  $A_0$  is the end of beam activity (Bq) estimated from the spectra for each monitor reaction,  $N_T$  was calculated from the mass densities, and  $\sigma(E)$  is the monitor data from the IAEA database. In the assumption that the deuteron beam current should not be degraded within the same compartment, it is possible to use multiple monitor reactions to determine the average beam current in each compartment, which gives a higher probability that the true beam current is found. This is provided that the simulated energy distributions are accurate [32]. As stated by Graves et. al. (2016), this method of using multiple monitor reactions has the potential of reducing the uncertainties in the deuteron energy towards the end of the stack.

Equation 5.9 builds upon the thin target assumption, which implies that the energy degradation in the foil is zero. However, we know that there is an energy distribution, which was estimated using NPAT's (Nuclear Physics Analysis Tool) Ziegler simulation [38]. The Ziegler code simulates the deuteron transport in a Monte-Carlo based simulation, based upon the Anderson & Ziegler stopping-power mode [39]. The code was ran with  $1 \cdot 10^6$  particles with a maximal number of steps being 100. The built in uncertainty in the deuteron energy was set to 0.5 MeV. Anderson & Ziegler is an empirical stopping power model, and takes the nuclear stopping-power (inelastic and elastic collisions), the electronic stoppingpower and the effective charge of the ions into account ([63], p. 96). Bethe-Block which is known as the stopping-power equation for heavy charged particles equation 2.3 only takes the electronic stopping power into account. Since both elastic and inelastic collisions are statistical events, the range is represented as a distribution ([63], p. 126-126). The code provides the full deuteron energy and flux spectra **distribution?** in each foil,  $d\phi/dE$ , which can be visualized for the iridium foils in figure 5.5. From the figure, it can be seen that as the deuteron energy is degraded through the stack, the mean value is shifted towards the low energy side of the peak along with an increasing energy-flux profile width. Because the stopping power is inversely proportional to the charged particle energy (From Bethe-Block,  $-\frac{dE}{dx} \propto \frac{1}{\beta^2}$ ), and the increasing degree of scattering towards the back of the stack, the low energy side of the flux is more degraded than the high energy side, creating a low energy tail, and a shift of the mean value (centroid) to lower energies. The shift causes a higher uncertainty in the energy for the lower energies. The (normalized) flux-weighted average energy for each foil was calculated, which takes the slowing down of deuterons and gives the effective energy centroid in each foil [33], using the energy distributions  $d\phi/dE$  provided by the Ziegler code:

$$\langle E \rangle = \frac{\int E \frac{d\phi}{dE} dE}{\int \frac{d\phi}{dE} dE} \quad (5.10)$$

The uncertainty in beam energy is divided into low energy and high energy tale, with the FWHM split by the centroid (figure 5.5).

Likewise, the energy-dependent monitor IAEA cross-sections need to be flux-weighted over each foil. This was done using the Scipy interpolation (splrep and splev) function with the smoothing condition set to zero, and the order of derivative set to zero [52]. The energy array over each foil provided by the Ziegler simulation was spline interpolated with the IAEA recommended cross section data. Thus, the monitor cross section term in equation 5.9 is modified to

$$\sigma(\langle E \rangle) = \frac{\int \sigma_{\text{mon}} \frac{d\phi}{dE} dE}{\int \frac{d\phi}{dE} dE} \quad (5.11)$$

The estimated beam-current for each monitor reaction in each foil was calculated using equation 5.9 with the modified terms for cross section and beam energy. The uncertainty for the beam-current in each reaction was calculated as the quadruple sum of each term (equation A.13). The weighted averaged beam current was estimated **Andrew: I dont understand how you did the weighted average in your python script. You did not use the numpy function...**, and the uncertainty in each parameter was calculated according to equation A.6, since each measured beam-current was co-varianced. Figure 5.8 (upper) shows the estimated beam current for each reaction in each foil with the measured areal densities and the 33 MeV deuteron beam. However, as we can see in the figure, the spread of the predicted beam current is quite large. The measured values of the beam current, especially in the back of the stack can be due to energy bins being assigned wrongly in the energy distribution simulation done in Ziegler-code or a systematic errors in the areal density which increases further back in the stack [35]. A way to work around this was to perform a variance minimization to find the correct energybins matching to the IAEA monitor cross sections, described in the next section.

#### 5.4.1 Variance minimization for the deuteron energy assignments

In theory, the estimated beam current of a charge particle beam should be constant, until completely stopped, since the majority of the incident particles does not interact in nuclear reactions, but only

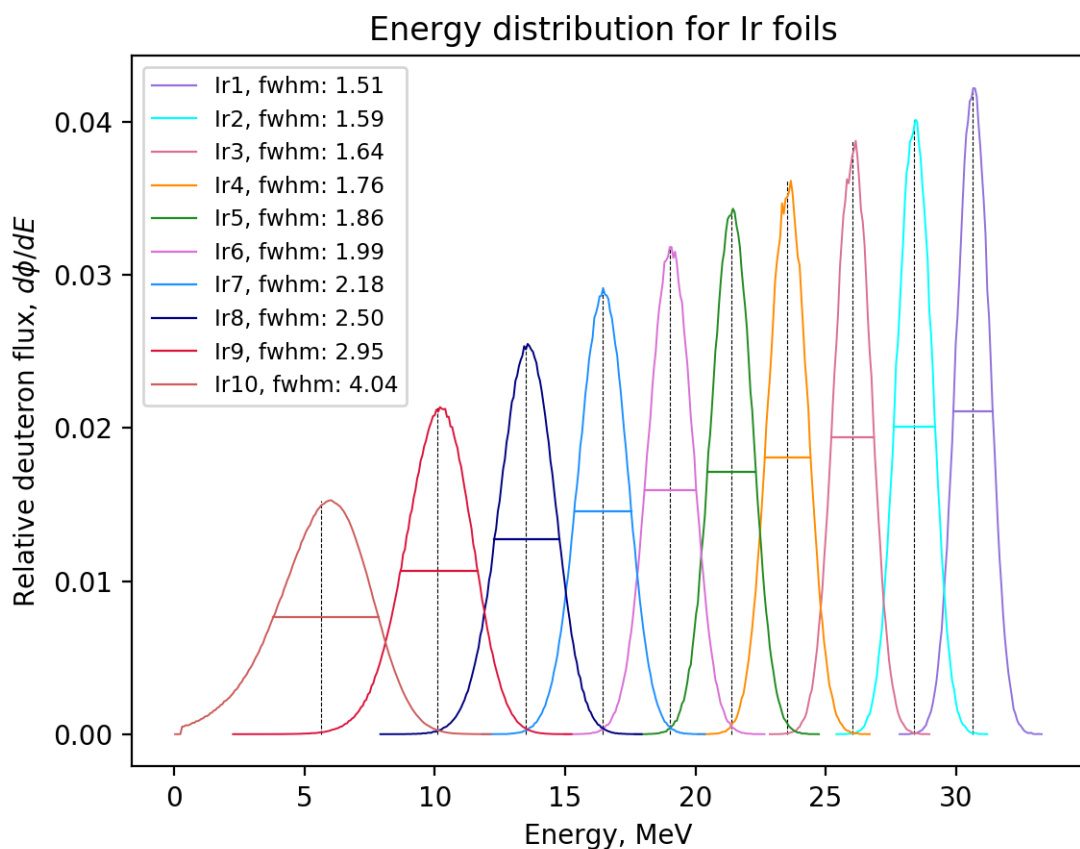


Figure 5.5: Iridium energy flux distribution over the 10 foils. As the energy degrades, skewed and larger full width half max. The vertical line in each peak is the mean value. This indicates that at lower energies, the right uncertainty is greater than the left uncertainty in the peak.

lose energy via elastic and inelastic scattering. This method has the potential to reduce the deuteron uncertainty in the foils in the back of the stack, where the effects of energy straggling ..... ??? Graves et. al. Variance minimization was performed varying the beam energy and the areal density of the foils with 20% increase and decrease systematically, and estimate the reduced  $\chi^2$  (equation A.4) over compartment 3,6 and 9. Applying changes in the areal density and the beam current does not imply that the values were wrong, but they that they were optimized to have the energy assignments correct to match the IAEA monitor cross section data [34]. This method was also performed in other similar experiments [?, 32, 33, 35], but instead of varying the density of each target foil, the density of the energy degraders which was used in those experiments was varied.

The reduced  $\chi^2$  was evaluated for Compartment 3 ( $E_d \approx 26$  MeV), compartment 6 ( $E_d \approx 19$  MeV) and compartment 9 ( $E_d \approx 10$  MeV). In compartment 3, all the seven monitor products were above threshold, and measured, so the data was good (with 6 degrees of freedom). However, since the scattering early in the foils were low, looking only on the reduced  $\chi^2$  in these foil did not evaluate the effect of scattering further back in the stack. In compartment 6, the 6 possible reactions from nickel and copper were above threshold, and gave a good estimate of how the beamcurrent was degrading through the stack, with no threshold-effects nor close to stopping. When the cross section (around threshold of the reaction), the beamcurrent increases proportionally (equation 5.9), thus leading to higher error bars. For  $^{nat}\text{Cu}(d,x)^{62}\text{Zn}$  ( $Q=-15.5$  MeV), the threshold is at ca. foil 7, and as a result, the uncertainty is very large in comparison to the other beamcurrents, which can be seen in figure 5.8. In compartment 9, all reactions except from  $^{nat}\text{Cu}(d,x)^{62}\text{Zn}$  and  $^{nat}\text{Fe}(d,x)^{56}\text{Co}$  was present. Here it is possible to see the full effect of scattering, along with the starting of decrease in beamcurrent as the particles slows down.

With the assumption that the beamcurrent loss is zero over one compartment, a linear fit-model (using the scipy optimize curvefit function [52]) with a slope equal to zero was used to estimate the beam current in each compartment, and with the estimated  $\chi^2$ . Figure 5.7 shows the different estimated  $\chi^2$  for each single Ziegler-run as a function of the flux-weighted averaged beam energy entering the compartment. There were several candidates, and all of them were small in  $\chi^2$  over all compartments, in particular over 6 and 9, and had positive areal density change and beam current, ranging from 1-2.5% in beam current and 1.25-7.5% in areal density. This implies that the average incident deuteron beam current was perhaps slightly larger. Finally, a change in beam current of 2% increase in beam current (33.7 MeV) and a change of 4.25% in areal density had the most consistent beam current over each compartment. Figure 5.6 shows the uncertainty weighted linear fit over compartment 6 using the 2% increase in beam current along with 4.25% increase in density.

Figure 5.8 shows the beam current before (upper) and after variance minimization (lower), and the weighted average beam currents are listed in table 5.2 estimated before and after the variance minimization. After variance minimization, the beam current estimated in each compartment (stabled lines) were similar, and meanwhile the weighted  $\chi^2$  was about the same in compartment 6, it has improved in compartment 3 and very visible in compartment 9. In general the points are more aligned.  $^{63}\text{Zn}$  was constantly too high. The uncertainty in beam current is affected by the activity measured which again is affected by the counting statistics, the intensity of the gamma-lines used and uncertainty in the efficiency (figure 4.7). Figure 5.9 shows the relative uncertainty in beam current in each compartment using the flux weighted average beam energies of iridium, along with the relative uncertainty in each reaction. It shows that the uncertainty increases as a function of decreasing energy, which makes sense due to the uncertainty with the scattering processes taking place back in the stack. Yet a relative uncertainty of less than 5.5% is ok. It is also clear that large uncertainties are weighted less than small uncertainties. Figure ?? shows the estimated cross sections (estimated using equation 5.9) where the estimated weighted average beam current for each target is plotted against the estimated cross section. In addition, the recommended IAEA cross sections [36] is plotted along with experimental data.

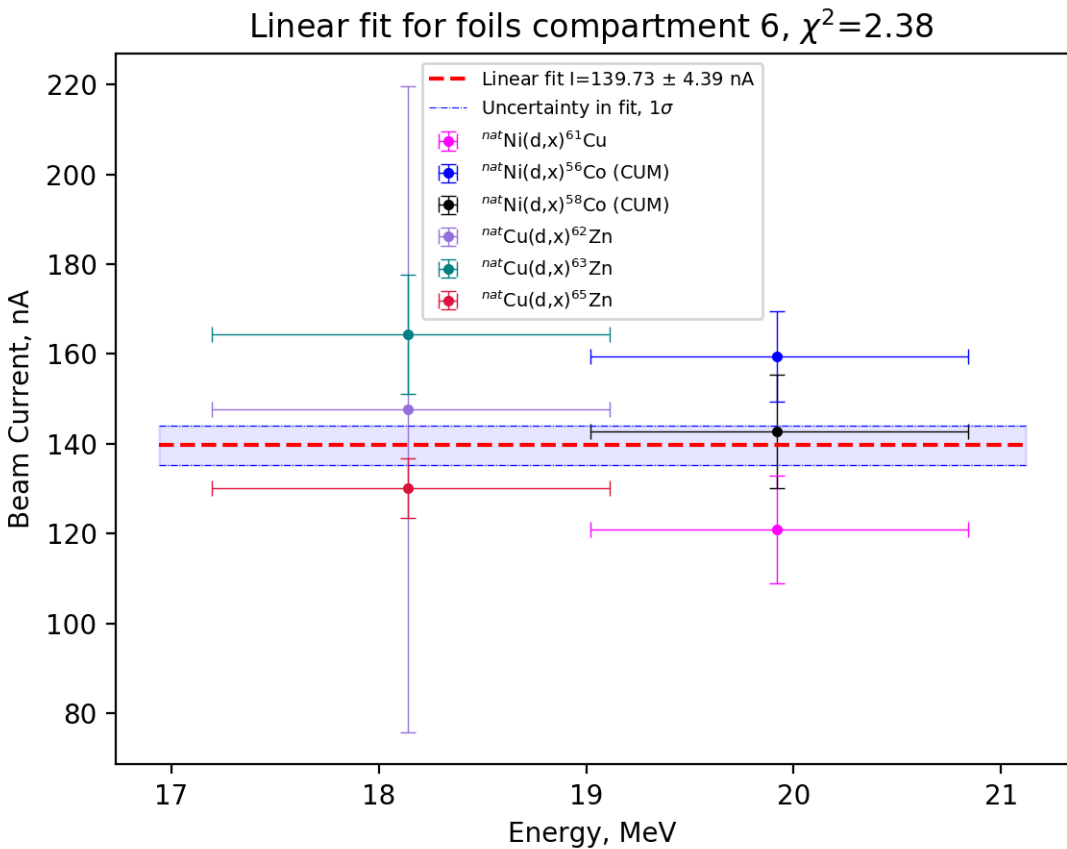


Figure 5.6: The estimated (uncertainty weighted) beamcurrent over compartment 6.

Table 5.2: The weighted average beam current before and after variance minimization in each compartment. The beam current on the 88-Inch Cyclotron beam integrator was 128.5 nA.

Compartment	Before	After
01	$131.56 \pm 3.64$	$134.08 \pm 3.70$
02	$132.23 \pm 3.74$	$136.42 \pm 3.83$
03	$133.81 \pm 3.64$	$138.02 \pm 3.75$
04	$134.89 \pm 4.21$	$138.88 \pm 4.31$
05	$136.85 \pm 4.21$	$139.67 \pm 4.29$
06	$137.40 \pm 4.53$	$138.85 \pm 4.58$
07	$139.55 \pm 4.37$	$139.77 \pm 4.37$
08	$133.60 \pm 4.27$	$134.96 \pm 4.32$
09	$133.16 \pm 5.04$	$143.59 \pm 5.67$
10	$108.49 \pm 5.80$	$121.75 \pm 6.65$

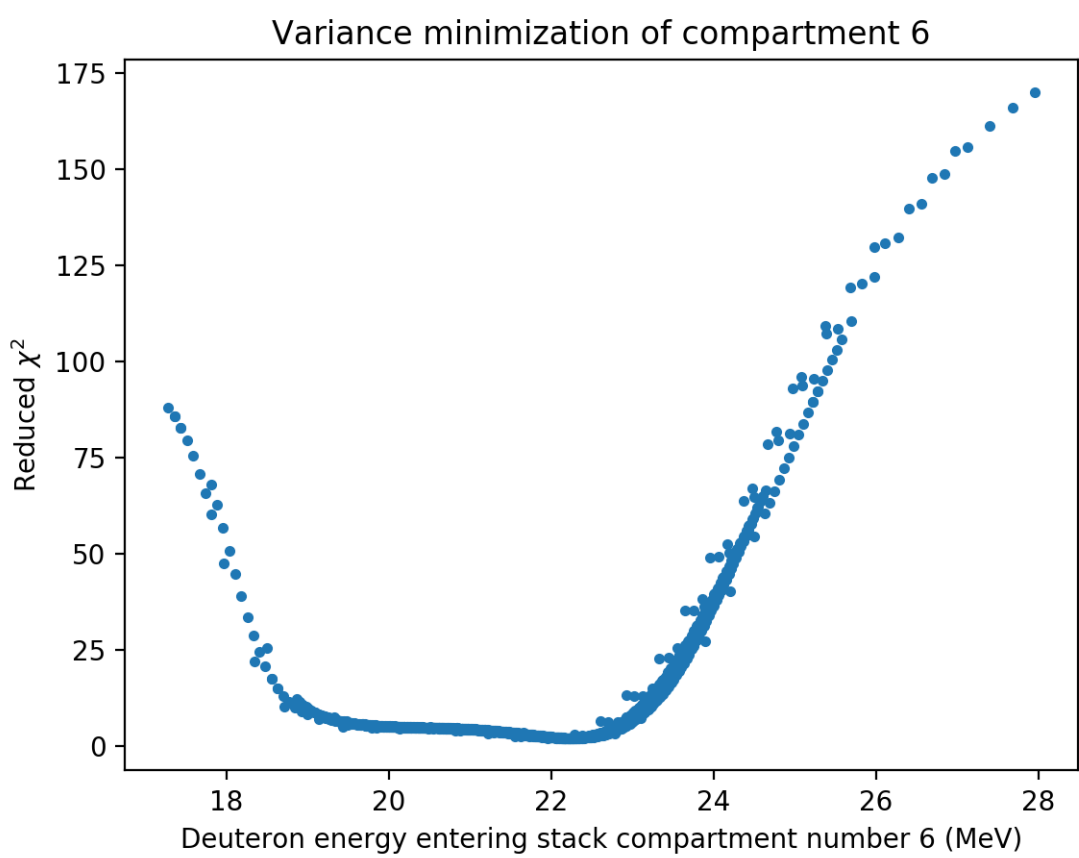


Figure 5.7: The figure shows the estimated reduced  $\chi^2$  as a function of the deuteron energy entering the stack (essentially the nickel flux weighted averaged beam energies).

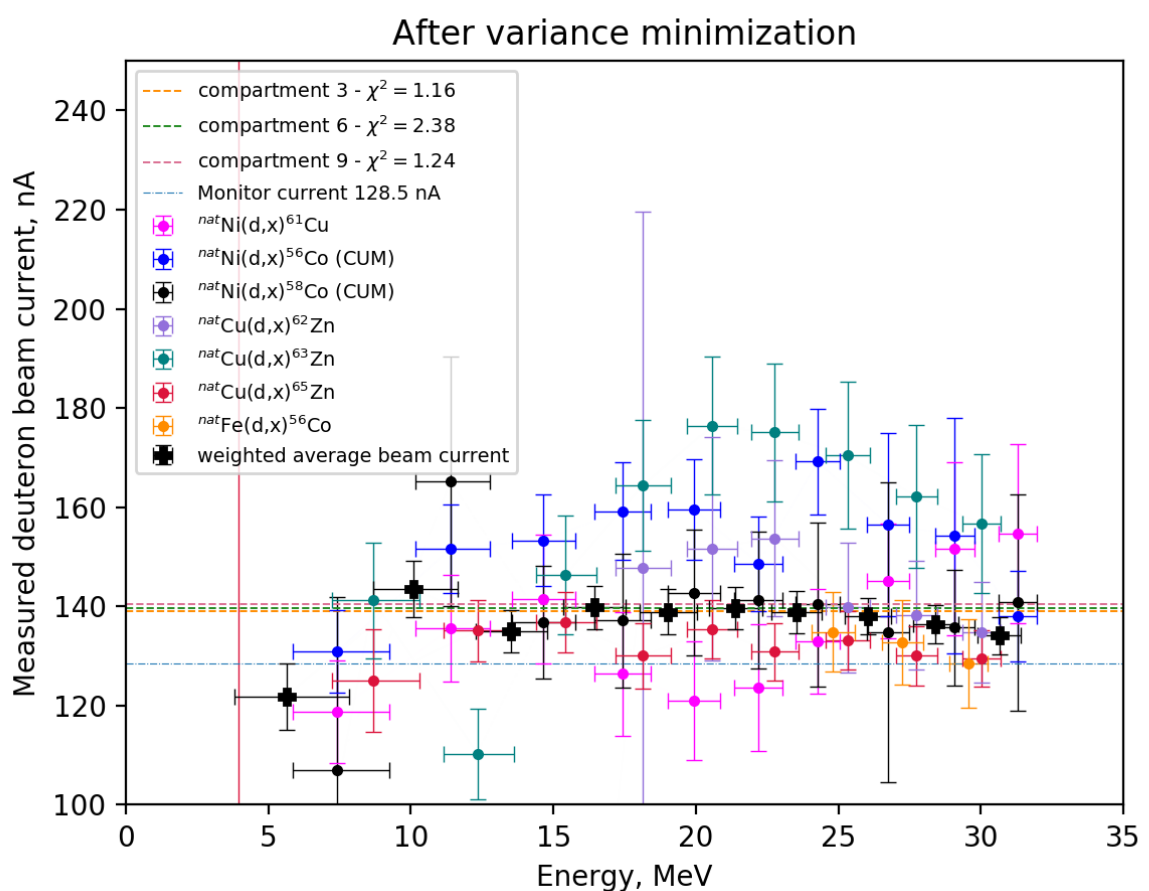
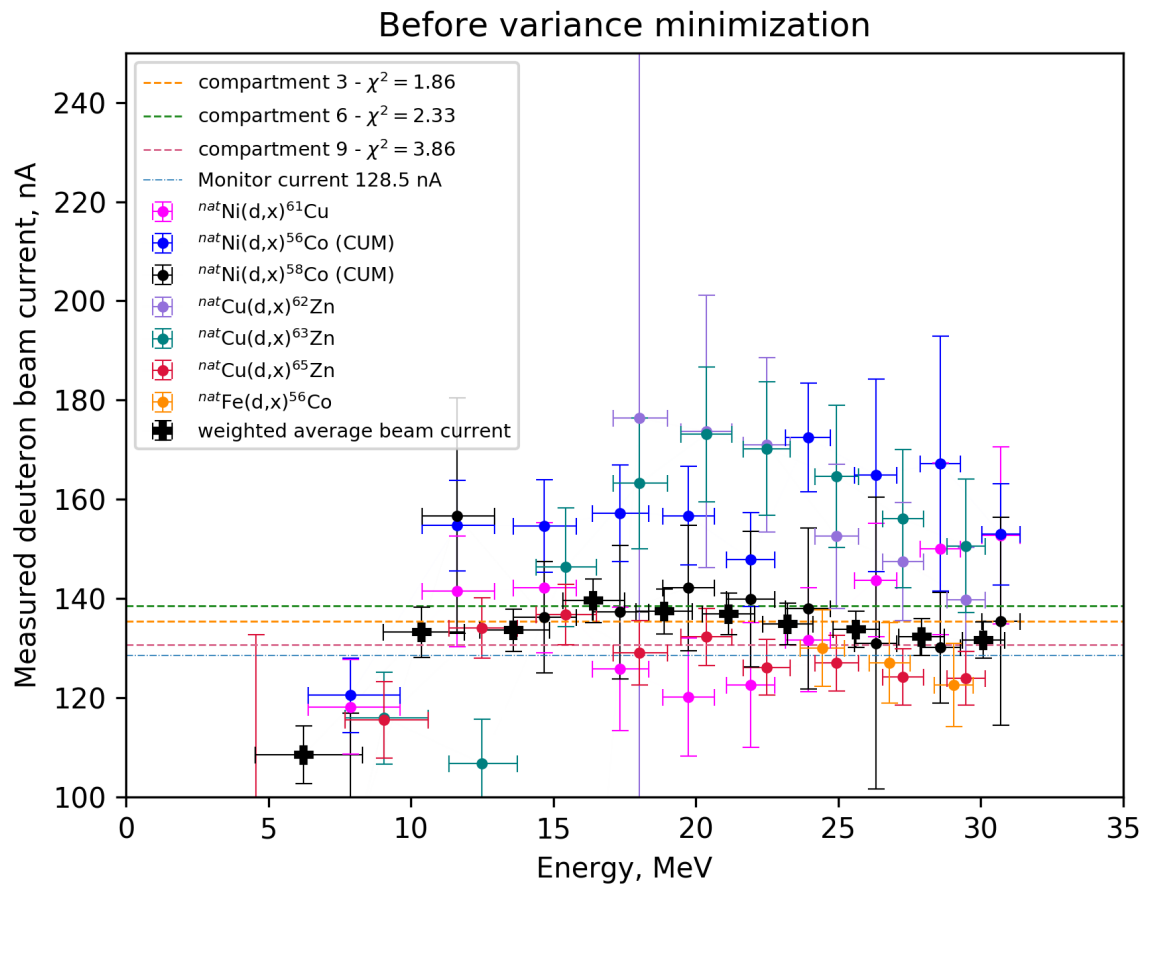


Figure 5.8: Beam current before and after variance minimization. The final cross section was performed with a 2% increase in beamcurrent and 4.25% change in target foils.

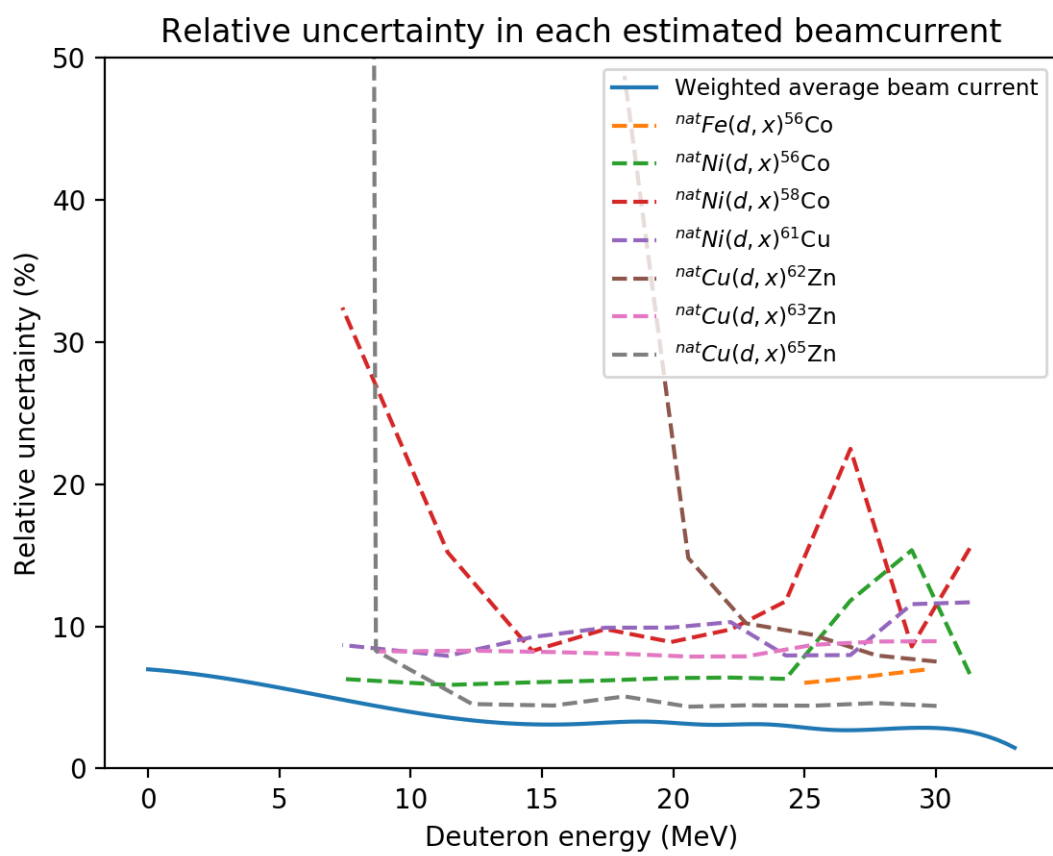


Figure 5.9: The relative uncertainty in the weighted average beam current as a function of deuteron energy in each compartment.

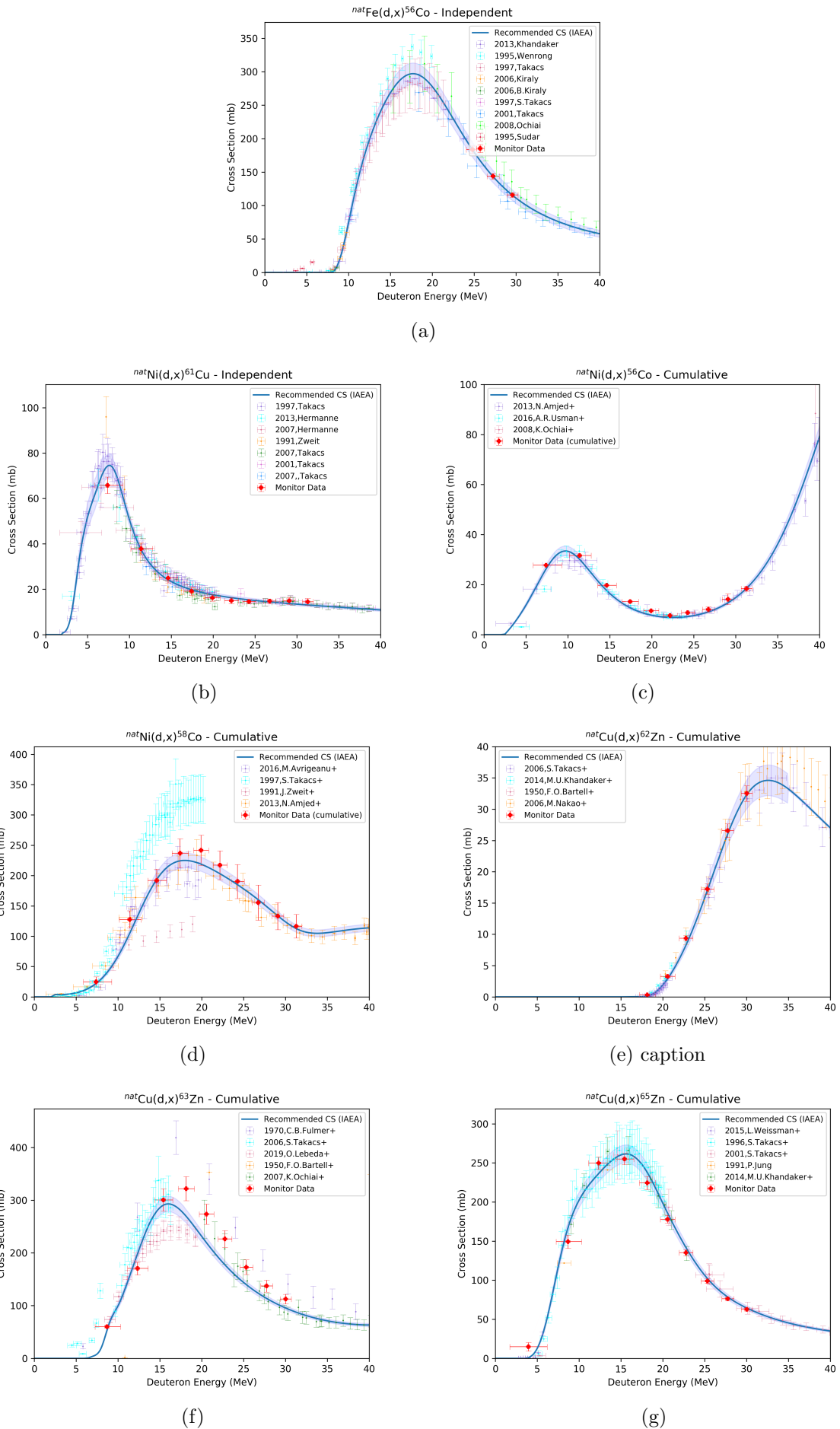


Figure 5.10: Figure shows the estimation of monitor cross section using the estimated weighted average beam current for each reaction (not the total). It is compared along with the recommended (IAEA) monitor data, and other experimental data

## 5.5 Cross sections

The cross sections were finally calculated via equation 3.6

$$\sigma(E) = \frac{A_0}{\Phi(E)N_T(1 - e^{-\lambda t_{\text{irr}}})} \quad (5.12)$$

as a function of the weighted average beam energy, the end of beam activities for the product, the number of target nuclei, the weighted average beam current, the irradiation time and the decay constant of product. The cross section results are represented in the next chapter. Nuclei with beta- or isomer feeding were reported as cumulative, as well as the first observed element in a decay chain, due to the possible feeding from short-lived activities. The remaining activities which were not subject to feeding were reported as independent. Whenever it was possible to extract parent feeding from daughter activity, both the cumulative and independent cross sections are reported.

The measured data is compared to previous experimental data from the EXFOR-database, along with nuclear reactor models TALYS-1.9, TENDL-2019, ALICE-2017 [64], CoH-3.5.3 and EMPIRE.... The theoretical models are important for several reasons, the general understanding of the reaction ([3], p. 23), and it can help to build confidence in experimental data. The default parameters for each reaction was used, so there was no change to the nuclear structure or the modeling of the reaction physics. Tuning the function will improve the local optimization, but it will not contribute to improving the code globally. Since the majority of the cross section measurements compares to the reaction models using default parameters, this is also what have been done in this work. The use of default parameters also reveals how well the code predicts the excitation function ([citation, comments from Andrew](#)). The exception was for CoH deuterons on iridium, for the exit channels alpha-particles and neutrons. The parameter *tweakSD* was set to 0.25 which adjusts the effective single-particle state density<sup>1</sup>. A 25% change of the single-particle state density for outgoing alpha-particles and neutrons is a huge change, but had to be done to get it to work.

<sup>2</sup>: Talys is a model for nuclear reactions involving neutrons, <sup>3</sup>He, protons, photons, deuterons, tritrons, alphaparticles in the 1 keV-200 MeV range for target nuclides of mass 5 and heavier. OPTICAL MODEL: represents the complicated interaction between an incident particle and a nucleus by a complex mean-field potential, which divides the reaction flux into a part covering shape elastic scattering and a part describing all the competing reaction channels. The input parameters; projectile, element, mass (natural) and the energy!

For compound nuclear reactions, the optical model, level density, gamma-ray strength function and fission transmissions coefficient as ingredients, low energy reactions. Both capture of the projectile and the multiple emission chain for the excited residual nuclides are needed.

Here write a few sentences about how each was done and the motivation behind it.

---

<sup>1</sup><http://physics.ucsc.edu/~peter/112/dos.pdf>

<sup>2</sup><https://doi.org/10.1016/j.nds.2012.11.002>

# Appendix A

## Statistics

Uncertainty in statistics refers to the standard deviation of the data, which gives a number of the spreading of the data from the mean value of the data citation. The variance is the standard deviation squared, which weights the variables to a higher degree.

$$std = \sqrt{\sigma^2} \quad (\text{A.1})$$

$$\sigma = \sqrt{\frac{1}{N} \sum_{i=1}^N (x_i - \bar{x})^2} \quad (\text{A.2})$$

where N is the number of measurements,  $x_i$  is a measurement and  $\bar{x}$  is the average over all measurements.

$\chi^2$  is an estimation of the goodness of the fit, which includes the weight of the error

$$\chi^2 = \sum_i^n \left( \frac{y_i - \bar{y}}{\sigma_i} \right)^2 \quad (\text{A.3})$$

where  $\bar{y}$  is the mean value of y and  $\sigma_i$  is the error in  $y_i$ . The reduced  $\chi^2$  is defined as the  $\chi^2$  per degree of freedom

$$\chi_\nu^2 = \frac{\chi^2}{\nu} \quad (\text{A.4})$$

where  $\nu$  is the degrees of freedom equal to the number of observations minus the number of fitted parameters. A value close to  $\chi_\nu^2 = 1$  indicates that the observations and fit is in well accordance to the error, while  $\chi_\nu^2 > 1$  indicates an underfitting and a  $\chi_\nu^2 < 1$  indicates an overfitting<sup>1</sup>.

A function  $f$  with input  $x$  and a set of variables  $\vec{\beta} = \beta_1, \beta_2, \dots, \beta_n$  and output y can be written on the following form

$$y = f(x, \vec{\beta}) \quad (\text{A.5})$$

The uncertainty in y is dependent on the uncertainty in the different input variables  $\vec{\beta}$ . The matrix expression for error propagation is (Tellinghuisen, Joel, Statistical error propagation)<sup>2</sup>

$$\sigma_y^2 = \mathbf{J} \cdot \mathbf{V} \cdot \mathbf{J}^T \quad (\text{A.6})$$

where  $\sigma_y^2$  is the variance in y, J is the Jacobian matrix

$$\mathbf{J} = \begin{bmatrix} \frac{\partial f}{\partial \beta_1} & \frac{\partial f}{\partial \beta_2} & \dots & \frac{\partial f}{\partial \beta_n} \end{bmatrix} \quad (\text{A.7})$$

and V is the variance-covariance matrix

---

<sup>1</sup>[https://en.wikipedia.org/wiki/Reduced\\_chi-squared\\_statistic](https://en.wikipedia.org/wiki/Reduced_chi-squared_statistic)

<sup>2</sup>A full derivation of the expression can be found in Uncertainty Propagation for Measurements with multiple output quantities, Dobbert, Schrijver

$$\mathbf{V} = \begin{bmatrix} \sigma_0^2 & \sigma_{0,1} & \cdots & \sigma_{0,n} \\ \sigma_{1,0} & \sigma_1^2 & \cdots & \sigma_{1,n} \\ \vdots & \vdots & \ddots & \vdots \\ \sigma_{n,0} & \sigma_{n,1} & \cdots & \sigma_n^2 \end{bmatrix} \quad (\text{A.8})$$

In the cases where the input parameters are uncorrelated, all non-diagonal elements in the variance-covariance matrix is equal to zero, and the expression for the variance is simplified to

$$\sigma_y^2 = \sum_{i=1}^n \left( \frac{\partial f}{\partial \beta_i} \right)^2 \sigma_{\beta_i}^2 \quad (\text{A.9})$$

Whenever the input parameters are correlated, which means that  $\sigma_{\beta_i, \beta_j} \neq 0$ , we have to apply equation A.6, otherwise, the simplification in equation A.9 will give wrong error propagation.

To evaluate the partial derivatives of  $f$ , the computational derivation is applicable

$$\frac{\partial f}{\partial \beta_i} \approx \frac{f(x, \beta_i + \frac{\Delta \beta_i}{2}) - f(x, \beta_i - \frac{\Delta \beta_i}{2})}{\Delta \beta_i} \quad (\text{A.10})$$

where  $\Delta \beta_i$  is a small number, like  $10^{-8} \beta_i$ .

For a function  $f = xy$ , the variance can be expressed from equation A.6, where

$$\mathbf{J} = [y \ x]$$

and

$$\mathbf{V} = \begin{bmatrix} \sigma_x^2 & \sigma_{x,y} \\ \sigma_{y,x} & \sigma_y^2 \end{bmatrix}$$

$$\sigma_f^2 = x^2 \sigma_y^2 + y^2 \sigma_x^2 + 2xy \sigma_{x,y} \quad (\text{A.11})$$

If we multiply each term so that we can collect  $f^2$  in the numerator, the variance in  $f$  can be expressed as

$$\sigma_f^2 = f^2 \left( \frac{\sigma_x^2}{x^2} + \frac{\sigma_y^2}{y^2} + \frac{2\sigma_{x,y}}{xy} \right) \quad (\text{A.12})$$

if the variables  $x$  and  $y$  are uncorrelated, the variance is further simplified, and more terms can be included easily. The simplified standard deviation of a function  $f(\bar{\beta}) = \beta_1 \cdot \beta_2 \cdots \beta_n$  with uncorrelated variables is thus

$$\sigma_f = |f| \sqrt{\left( \frac{\sigma_{\beta_1}}{\beta_1} \right)^2 + \left( \frac{\sigma_{\beta_2}}{\beta_2} \right)^2 + \cdots + \left( \frac{\sigma_{\beta_n}}{\beta_n} \right)^2} \quad (\text{A.13})$$

## Appendix B

## Tables

For all tables, the assumption is that the main particle emission is due to alpha, proton or neutron emission. However, triton,  $^3\text{He}$  and deuterons are still fed when above threshold, but from theory, the feeding is low. For triton,  $^3\text{He}$  and deuteron respectively, subtract 8.5, 7.7 or 2.2 respectively from the Q value. Alphaparticles (due to the large binding energy and spin equal to 0) will be more fed. To calculate Q value for alpha emission subtract 28.3 MeV from Q value of 2p2n-reactions. Q values from <sup>1</sup> are used. Q values below 40 MeV are included for comparison to experimental data.

## B.1 Product nuclei, Q-values and gammarays

Table B.1: Products observed on Nickel foils. Nickel has five stable isotopes:  $^{58}\text{Ni}$  (68.077%),  $^{60}\text{Ni}$  (26.223 %),  $^{61}\text{Ni}$  (1.1399%),  $^{62}\text{Ni}$  (3.6346%) and  $^{64}\text{Ni}$  (0.9255%). If the nucleus has provided energy level, the nucleus is an isomer, if nothing then ground state. **The table is inspired by Tarkanyi et al 2019 (ir paper)**

Nuclide level (keV)	Half life	Decay mode	Reaction route	Q value (keV)	$E_{\gamma}$ (keV)	$I_{\gamma}$ (%)
$^{52}\text{Mn}$ (0.0)	5.591 d 21.1 m	$\epsilon$ : 100%	$^{58}\text{Ni}(\text{d},2\alpha)$ $^{60}\text{Ni}(\text{d},2\text{n}2\alpha)$ $^{61}\text{Ni}(\text{d},3\text{n}2\alpha)$	-1235.6 -21622.6 -29442.7	744.233 935.544 1246.278 1434.092	90.0 94.5 4.21 100.0
$^{54}\text{Mn}$ (0.0)	312.20 d	$\epsilon$ : 100%	$^{58}\text{Ni}(\text{d},2\text{p}\alpha)$ $^{60}\text{Ni}(\text{d},2\alpha)$ $^{61}\text{Ni}(\text{d},\text{n}2\alpha)$ $^{62}\text{Ni}(\text{d},2\text{n}2\alpha)$	-8538.3 -629.6 -8449.7 -19045.4	834.848	99.9760
$^{59}\text{Fe}$ (0.0)	44.490 d	$\beta^-$ : 100%	$^{60}\text{Ni}(\text{d},3\text{p})$ $^{61}\text{Ni}(\text{d},\text{n}3\text{p})$ $^{62}\text{Ni}(\text{d},\text{p}\alpha)$ $^{64}\text{Ni}(\text{d},2\text{n}\text{p}\alpha)$	-12539.5 -20359.6 -2659.7 -19154.9	1291.590	43.2
$^{55}\text{Co}$ (0.0)	17.53 h	$\epsilon$ : 100%	$^{58}\text{Ni}(\text{d},\text{n}\alpha)$ $^{60}\text{Ni}(\text{d},3\text{n}\alpha)$ $^{61}\text{Ni}(\text{d},4\text{n}\alpha)$	-3559.4 -23946.4 -31766.5	385.4 520.0 803.7 931.1 1212.8 1316.6 1370.0 2177.6	0.54 0.83 1.87 75 0.26 7.1 2.9 0.29

<sup>1</sup><https://www.nndc.bnl.gov/qcalc/>

## APPENDIX B. TABLES

$^{56}\text{Co}$ (0.0)	77.236 d	$\epsilon : 100\%$	$^{58}\text{Ni}(\text{d},\alpha)$ $^{61}\text{Ni}(\text{d},2\text{n}\alpha)$ $^{61}\text{Ni}(\text{d},3\text{n}\alpha)$ $^{62}\text{Ni}(\text{d},4\text{n}\alpha)$	6522.5 -13864.5 -21684.6 -32280.4	787.743 846.770 977.372 1175.101 1963.741 2015.215 2034.791	0.3111 99.9399 1.421 2.252 0.707 3.016 7.77
$^{57}\text{Co}$ (0.0)	271.74 d	$\epsilon : 100\%$	$^{58}\text{Ni}(\text{d},\text{n}2\text{p})$ $^{60}\text{Ni}(\text{d},\text{n}\alpha)$ $^{61}\text{Ni}(\text{d},2\text{n}\alpha)$ $^{62}\text{Ni}(\text{d},3\text{n}\alpha)$	-10396.7 -2488.1 -10308.2 -20903.9	122.06065 136.47365	85.60 10.68
$^{58}\text{Co}$ (0.0)	70.86 d	$\epsilon : 100\%$	$^{58}\text{Ni}(\text{d},2\text{n})$ $^{60}\text{Ni}(\text{d},\alpha)$ $^{61}\text{Ni}(\text{d},\text{n}\alpha)$ $^{62}\text{Ni}(\text{d},2\text{n}\alpha)$ $^{64}\text{Ni}(\text{d},4\text{n}\alpha)$	-1823.8 6084.9 -1735.3 -12331.0 -28826.2	810.7593 863.951 1674.725	99.450 0.686 0.517
$^{58m}\text{Co}$ (24.88921)	9.10 h	IT:100%	$^{58}\text{Ni}(\text{d},2\text{n})$ $^{60}\text{Ni}(\text{d},\alpha)$ $^{61}\text{Ni}(\text{d},\text{n}\alpha)$ $^{62}\text{Ni}(\text{d},2\text{n}\alpha)$ $^{64}\text{Ni}(\text{d},4\text{n}\alpha)$	-1848.7 6060.0 -1760.2 -12355.9 -28851.1	-	-
$^{60}\text{Co}$ (0.0)	1925.28 d	$\beta^- : 100\%$	$^{60}\text{Ni}(\text{d},2\text{p})$ $^{61}\text{Ni}(\text{d},\text{n}2\text{p})$ $^{62}\text{Ni}(\text{d},\alpha)$ $^{64}\text{Ni}(\text{d},2\text{n}\alpha)$	-4265.0 -12085.1 5614.8 -10880.4	1173.228 1332.492	99.85 99.9826
$^{56}\text{Ni}$ (0.0)	6.075 d	$\epsilon : 100\%$	$^{58}\text{Ni}(\text{d},3\text{np})$	-24688.4	158.38 480.44 749.95 811.85 1561.80	98.8 36.5 49.5 86.0 14.0
$^{57}\text{Ni}$ (0.0)	35.60 h	$\beta^+ : 100\%$	$^{58}\text{Ni}(\text{d},2\text{np})$ $^{60}\text{Ni}(\text{d},4\text{np})$	-14440.8 -34827.8	1757.55 1919.52 2804.20	5.75 12.3 0.098
$^{65}\text{Ni}$ (0.0)	2.51719 h	$\beta^- : 100\%$	$^{64}\text{Ni}(\text{d},\text{p})$	3873.51	366.27 1481.84 1623.42 1724.92	4.81 23.59 0.498 0.399
$^{60}\text{Cu}$ (0.0)	23.7 m	$\epsilon : 100\%$	$^{60}\text{Ni}(\text{d},2\text{n})$ $^{61}\text{Ni}(2,3\text{n})$ $^{62}\text{Ni}(\text{d},4\text{n})$	-9134.9 -16955.0 -27550.7	467.3 497.9 643.2 952.4 1035.2 1110.5 1293.7 1791.6 1861.6 1936.9 2061.0 2158.9 2403.3 2687.9 2746.1	3.52 1.67 0.97 2.73 3.70 1.06 1.85 45.4 4.8 2.20 0.79 3.34 0.77 0.44 1.06

<sup>61</sup> Cu	3.339 h	$\epsilon : 100\%$	<sup>60</sup> Ni(d,n)	2575.3	282.956	12.2
			<sup>61</sup> Ni(d,2n)	-5244.8	373.050	2.1
			<sup>62</sup> Ni(d,3n)	-15840.5	529.169	0.38
			<sup>64</sup> Ni(d,5n)	-32335.7	588.605	1.17
					625.605	0.040
					656.008	10.8
					816.692	0.31
					841.211	0.21
					902.294	0.083
					1032.162	0.043
					1073.465	0.033
					1132.351	0.090
					1185.234	3.7
					1446.492	0.045
<sup>64</sup> Cu	12.701 h	$\epsilon : 100\%$	<sup>64</sup> Ni(d,2n)	-4681.3	1345.77	0.475
		$\beta^- : 38.5\%$				

APPENDIX B. TABLES

---

Table B.2: Products observed on Iron foils. Iron has five stable isotopes:  $^{54}\text{Fe}$  (5.845%),  $^{56}\text{Fe}$  (91.754 %),  $^{57}\text{Fe}$  (2.119%) and  $^{58}\text{Fe}$  (0.282%). If the nucleus has provided energy level, the nucleus is an isomer, if nothing then ground state. **The table is inspired by Tarkanyi et al 2019 (ir paper)**

Nuclide level (keV)	Half life	Decay mode	Reaction route	Q value (keV)	$E_\gamma$ (keV)	$I_\gamma$ (%)
$^{48}\text{V}$ (0.0)	15.9735 d	$\epsilon : 100\%$	$^{54}\text{Fe}(\text{d},2\alpha)$	-3490.9	944.130	7.870
			$^{56}\text{Fe}(\text{d},2\text{n}2\alpha)$	-23986.1	983.525	99.98
			$^{57}\text{Fe}(\text{d},3\text{n}2\alpha)$		1312.106	98.2
$^{51}\text{Cr}$ (0.0)	27.704 d	$\epsilon : 100\%$	$^{54}\text{Fe}(\text{d},\text{p}\alpha)$	-1381.3	320.0824	9.910
			$^{56}\text{Fe}(\text{d},2\text{n}\alpha)$	-21876.5		
			$^{57}\text{Fe}(\text{d},3\text{n}\alpha)$	-29522.6		
			$^{58}\text{Fe}(\text{d},4\text{n}\alpha)$	-39567.2		
$^{52}\text{Mn}$ (0.0)	5.591 d d	$\epsilon : 100\%$	$^{54}\text{Fe}(\text{d},\alpha)$	5163.6	346.02	0.980
			$^{56}\text{Fe}(\text{d},2\text{n}\alpha)$	-15331.6	744.233	90.0
			$^{57}\text{Fe}(\text{d},3\text{n}\alpha)$	-22977.7	848.18	3.32
					935.544	94.5
					1246.278	4.21
					1333.649	5.07
					1434.092	100.0
$^{54}\text{Mn}$ (0.0)	312.20 d	$\epsilon : 100\%$	$^{54}\text{Fe}(\text{d},2\text{p})$	-2139.1	834.8480	99.9760
			$^{56}\text{Fe}(\text{d},\alpha)$	5661.4		
			$^{57}\text{Fe}(\text{d},\text{n}\alpha)$	-1984.7		
			$^{58}\text{Fe}(\text{d},2\text{n}\alpha)$	-12029.3		
$^{53}\text{Fe}$ (0.0)	8.51 m ????	$\epsilon : 100\%$	$^{54}\text{Fe}(\text{d},2\text{np})$	-15602.9	377.9	42%
			$^{56}\text{Fe}(\text{d},4\text{np})$	-36098.1		
$^{59}\text{Fe}$ (0.0)	44.490 d	$\beta^- : 100\%$	$^{58}\text{Fe}(\text{d},\text{p})$	4356.44	1099.245	56.5
					1291.590	43.2
$^{55}\text{Co}$ (0.0)	17.53 h	$\epsilon : 100\%$	$^{54}\text{Fe}(\text{d},\text{n})$	2839.8	91.9	1.16
			$^{56}\text{Fe}(\text{d},3\text{n})$	-17655.4	477.2	20.2
			$^{57}\text{Fe}(\text{d},4\text{n})$	-25301.5	803.7	1.87
					827.0	0.21
					931.1	75
					1316.6	7.1
					1370.0	2.9
					1408.5	16.9
					2177.6	0.29
					2872.4	0.118
					2938.9	0.057

$^{56}\text{Co}$	77.236 d	$\epsilon : 100\%$	$^{56}\text{Fe}(\text{d},2\text{n})$	-7573	263.434	0.0220
(0.0)			$^{57}\text{Fe}(\text{d},3\text{n})$	-15219.7	486.55	0.0540
			$^{58}\text{Fe}(\text{d},4\text{n})$	-25264.3	733.514	0.191
					787.743	0.311
					846.770	99.9399
					852.732	0.049
					896.510	0.073
					977.372	1.421
					996.948	0.111
					1037.843	14.05
					1140.368	0.132
					1159.944	0.094
					1175.101	2.252
					1198.888	0.049
					1238.288	66.46
					1335.40	0.1224
					1360.212	4.283
					1771.357	15.41
					1963.741	0.707
					2015.215	3.016
					2034.791	7.77
					2212.944	0.388
					2276.131	0.118
					2598.500	16.97
$^{57}\text{Co}$	271.74 d	$\epsilon : 100\%$	$^{56}\text{Fe}(\text{d},\text{n})$	3802.9	122.06065	85.60
(0.0)			$^{57}\text{Fe}(\text{d},2\text{n})$	-3843.2	136.47356	10.68
			$^{58}\text{Fe}(\text{d},3\text{n})$	-13887.8		
$^{58}\text{Co}$	70.86	$\epsilon : 100\%$	$^{57}\text{Fe}(\text{d},\text{n})$	4729.7	810.7593	99.450
(0.0)			$^{58}\text{Fe}(\text{d},2\text{n})$	-5314.9		

APPENDIX B. TABLES

---

Table B.3: Products observed on Copper foils. Copper has two stable isotopes:  $^{63}\text{Cu}$  (69.15%) and  $^{65}\text{Cu}$  (30.85 %). If the nucleus has provided energy level, the nucleus is an isomer, if nothing then ground state. **The table is inspired by Tarkanyi et al 2019 (in paper)**

Nuclide level (keV)	Half life	Decay mode	Reaction route	Q value (keV)	$E_{\gamma}$ (keV)	$I_{\gamma}$ (%)
$^{59}\text{Fe}$ (0.0)	44.490 d	$\beta^-$ : 100%	$^{63}\text{Cu}(\text{d},2\text{p}\alpha)$	-8782.1	1099.245	56.5
			$^{65}\text{Cu}(\text{d},2\alpha)$	1687.0	1291.590	43.2
$^{60}\text{Co}$ (0.0)	1925.28 d	$\beta^-$ : 100%	$^{63}\text{Cu}(\text{d},\text{p}\alpha)$	-507.6	1173.228	99.85
			$^{65}\text{Cu}(\text{d},2\text{n}\alpha)$	-18334.1	1332.492	99.9826
$^{61}\text{Co}$ (0.0)	1.649 h	$\beta^-$ : 100%	$^{63}\text{Cu}(\text{d},\text{n}3\text{p})$	-19484.2	67.412	84.7
			$^{65}\text{Cu}(\text{d},\text{n}p\alpha)$	-9015.1		
$^{65}\text{Ni}$ (0.0)	2.51719 h	$\beta^-$ : 100%	$^{65}\text{Cu}(\text{d},2\text{p})$	-3580.2	1481.84	23.59
			$^{63}\text{Cu}(\text{d},3\text{np})$	-21962.9	282.956	12.2
$^{61}\text{Cu}$ (0.0)	3.339 h	$\epsilon$ : 100% $\beta^-$ : 38.5	$^{65}\text{Cu}(\text{d},5\text{np})$	-39789.4	656.008	10.8
			$^{63}\text{Cu}(\text{d},\text{p})$	5691.54	1185.234	3.7
$^{64}\text{Cu}$ (0.0)	12.701 h	$\epsilon$ : 61.5% $\beta^-$ : 38.5	$^{65}\text{Cu}(\text{d},2\text{np})$	-12135.0	1345.77	0.475
			$^{63}\text{Zn}(\text{d},3\text{n})$	-15490.0	40.85	25.5
$^{62}\text{Zn}$ (0.0)	9.193 h	$\epsilon$ : 100%	$^{65}\text{Cu}(\text{d},5\text{n})$	-33316.6	243.36	2.52
					246.95	1.90
					260.43	1.35
					304.88	0.29
					394.03	2.24
					548.35	15.3
					596.56	26.0
$^{63}\text{Zn}$ (0.0)	38.47 m	$\epsilon$ : 100%			637.41	0.25
			$^{63}\text{Cu}(\text{d},2\text{n})$	-6373.3	449.93	0.236
			$^{65}\text{Cu}(\text{d},4\text{n})$	-24199.8	669.62	8.2
$^{65}\text{Zn}$ (0.0)	243.93 d	$\epsilon$ : 100%			962.06	6.5
			$^{65}\text{Cu}(\text{d},2\text{n})$	-4358.6	1115.539	50.04

Table B.4: Products observed in Iridium foils. Iridium has two stable isotopes:  $^{191}\text{Ir}$  (37.3%) and  $^{93}\text{Ir}$  (62.7 %). If the nucleus has provided energy level, the nucleus is an isomer, if nothing then ground state. **The table is inspired by Tarkanyi et al 2019 (ir paper)**

Nuclide level (keV)	Half life	Decay mode	Reaction route	Q value (keV)	$E_{\gamma}$ (keV)	$I_{\gamma}$ (%)
$^{188}\text{Ir}$ (0.0)	41.5 h	$\epsilon$ : 100%	$^{191}\text{Ir}(\text{d},4\text{np})$	-24802.0	1209.80	6.9
					1715.67	6.2
					2059.65	7.0
$^{189}\text{Ir}$ (0.0)	13.2 d	$\epsilon$ : 100%	$^{191}\text{Ir}(\text{d},4\text{np})$	-16626.0	95.23	0.38
					216.7	0.52
			$^{193}\text{Ir}(\text{d},5\text{np})$	-30596.0	233.5	0.30
					245.1	6.0
$^{190}\text{Ir}$ (0.0)	11.78 d	$\epsilon$ : 100%	$^{191}\text{Ir}(\text{d},2\text{np})$	-10251.1	294.75	6.6
					380.03	2.03
			$^{193}\text{Ir}(\text{d},4\text{np})$	-24221.2	1036.05	2.42
$^{190m^2}\text{Ir}$ (376.4)	3.087 h	IT:8.6% $\epsilon$ : 91.4%	..	..	361.2	86.72
					502.5	89.38
					616.5	90.14
$^{192}\text{Ir}$ (0.0)	73.829 d	$\epsilon$ : 4.76% $\beta^-$ : 95.24%	$^{191}\text{Ir}(\text{d},\text{p})$	3973.55	201.3112	0.471
					295.95650	28.71
			$^{193}\text{Ir}(\text{d},2\text{np})$	-9996.6	374.4852	0.727
					416.4688	0.670
					468.06885	47.84
					489.06	0.438
					612.46215	5.34
					1061.49	0.0531
			$^{194}\text{Ir}(\text{d},\text{p})$	3842.22	293.541	2.5
					300.741	0.35
					589.179	0.140
					938.69	0.60
					1150.75	0.60
					1468.91	0.19
$^{194m^2}\text{Ir}$ (190+X)	171 d	$\beta^-$ : 100%	..	..	338.8	55
					482.6	97
					562.4	35
					687.8	3.6
$^{188}\text{Pt}$ (0.0)	10.16 d	$\epsilon$ : 99.999974% $\alpha$ : $2.6E - 5\%$	$^{191}\text{Pt}(\text{d},2\text{n})$	-26109.0	195.05	18.4
					381.43	7.4
$^{189}\text{Pt}$ (0.0)	10.87 h	$\epsilon$ : 100%	$^{191}\text{Ir}(\text{d},4\text{n})$	-19389.0	94.34	6.5
					113.82	2.5
					243.50	5.9
					317.65	2.8
					721.38	7.9
$^{191}\text{Pt}$ (0.0)	2.802 d	$\epsilon$ : 100%	$^{191}\text{Ir}(\text{d},2\text{n})$	-4017.0	178.96	12.5
					351.17	42.6
			$^{193}\text{Ir}(\text{d},4\text{n})$	-17988.0	409.44	100
					456.47	42
					538.87	181
					624.06	18.5
$^{193m}\text{Pt}$ (149.783)	4.33 d	IT:100%	$^{193}\text{Ir}(\text{d},2\text{n})$	-3063.5	66.831	7.21
					135.5	0.1145475

Table B.5: Iridium production cross sections produced from Iridium

$E_d$ (MeV)	Production cross section (mb) for iridium radionuclides				
	$^{188m1+g}\text{Ir}_{\text{cum}}$	$^{188m1+g}\text{Ir}_{\text{ind}}$	$^{189}\text{Ir}_{\text{cum}}$	$^{190m1+g}\text{Ir}_{\text{cum}}$	$^{190m1+g}\text{Ir}_{\text{ind}}$
$30.65^{+0.76}_{-0.75}$	$1.37 \pm 0.10$	$0.42 \pm 0.03$	$332.49 \pm 24.20$	$86.65 \pm 2.89$	$85.88 \pm 2.86$
$28.40^{+0.80}_{-0.79}$	$0.45 \pm 0.07$	$0.17 \pm 0.02$	$237.84 \pm 17.44$	$62.80 \pm 2.14$	$62.36 \pm 2.13$
$26.03^{+0.82}_{-0.82}$	$0.34 \pm 0.08$	$0.17 \pm 0.03$	$91.49 \pm 5.47$	$44.26 \pm 1.47$	$44.01 \pm 1.46$
$23.54^{+0.88}_{-0.87}$	-	-	$19.23 \pm 2.65$	$27.29 \pm 1.02$	$27.19 \pm 1.02$
$21.38^{+0.94}_{-0.92}$	-	-	-	$18.73 \pm 0.71$	$18.69 \pm 0.70$
$19.03^{+1.00}_{-0.99}$	-	-	-	$14.02 \pm 0.55$	$14.00 \pm 0.55$
$16.43^{+1.11}_{-1.08}$	-	-	-	$12.40 \pm 0.51$	$12.39 \pm 0.51$
$13.51^{+1.28}_{-1.22}$	-	-	-	$8.26 \pm 0.43$	$8.25 \pm 0.42$
$10.09^{+1.55}_{-1.41}$	-	-	-	-	-
$5.63^{+2.21}_{-1.83}$	-	-	-	-	-

Table B.6: Iridium production cross sections produced from Iridium

$E_d$ (MeV)	Production cross section (mb) for iridium radionuclides			
	$^{190m2}\text{Ir}_{\text{ind}}$	$^{192}\text{Ir}_{\text{cum}}$	$^{194g}\text{Ir}_{\text{cum}}$	$^{194m2}\text{Ir}_{\text{ind}}$
$30.65^{+0.76}_{-0.75}$	$8.87 \pm 0.25$	$188.43 \pm 5.27$	$50.92 \pm 2.18$	-
$28.40^{+0.80}_{-0.79}$	$5.03 \pm 0.15$	$152.55 \pm 4.39$	$51.39 \pm 2.89$	-
$26.03^{+0.82}_{-0.82}$	$2.92 \pm 0.08$	$124.33 \pm 3.42$	$61.37 \pm 2.39$	$0.74 \pm 0.17$
$23.54^{+0.88}_{-0.87}$	$1.16 \pm 0.04$	$100.03 \pm 3.14$	$69.68 \pm 2.76$	$0.68 \pm 0.26$
$21.38^{+0.94}_{-0.92}$	$0.45 \pm 0.01$	$90.41 \pm 2.80$	$86.38 \pm 3.18$	$0.65 \pm 0.13$
$19.03^{+1.00}_{-0.99}$	$0.16 \pm 0.01$	$90.65 \pm 3.01$	$97.79 \pm 3.99$	$0.60 \pm 0.14$
$16.43^{+1.11}_{-1.08}$	0.06 0.00	$99.61 \pm 3.14$	$121.54 \pm 4.54$	$0.50 \pm 0.09$
$13.51^{+1.28}_{-1.22}$	0.03 0.00	$107.41 \pm 3.48$	$143.27 \pm 5.52$	-
$10.09^{+1.55}_{-1.41}$	0.02 0.00	$64.27 \pm 2.56$	$92.78 \pm 4.21$	-
$5.63^{+2.21}_{-1.83}$	0.02 0.00	$6.67 \pm 0.37$	$6.32 \pm 0.42$	-

## B.2 Production cross sections

### B.2.1 ${}^{\text{nat}}\text{Ir}(\text{d},\text{x})$

Table B.7: Platinum production cross sections produced from Iridium

$E_d$ (MeV)	Production cross section (mb) for platinum radionuclides			
	$^{188}\text{Pt}_{\text{ind}}$	$^{189}\text{Pt}_{\text{ind}}$	$^{191}\text{Pt}_{\text{ind}}$	$^{193m}\text{Pt}_{\text{ind}}$
$30.65^{+0.76}_{-0.75}$	$0.94 \pm 0.13$	$486.47 \pm 21.86$	$597.10 \pm 16.55$	$48.11 \pm 6.33$
$28.40^{+0.80}_{-0.79}$	$0.30 \pm 0.09$	$341.24 \pm 16.64$	$483.60 \pm 13.79$	$46.78 \pm 2.19$
$26.03^{+0.82}_{-0.82}$	$0.17 \pm 0.05$	$172.11 \pm 8.03$	$353.99 \pm 9.67$	$55.68 \pm 2.17$
$23.54^{+0.88}_{-0.87}$	-	$30.72 \pm 1.48$	$165.12 \pm 5.15$	$51.79 \pm 2.12$
$21.38^{+0.94}_{-0.92}$	-	$1.04 \pm 0.07$	$71.05 \pm 2.19$	$58.31 \pm 1.96$
$19.03^{+1.00}_{-0.99}$	-	$0.09 \pm 0.02$	$77.53 \pm 2.57$	$77.98 \pm 2.89$
$16.43^{+1.11}_{-1.08}$	-	-	$128.24 \pm 4.03$	$115.33 \pm 4.09$
$13.51^{+1.28}_{-1.22}$	-	-	$137.37 \pm 4.42$	$148.98 \pm 5.54$
$10.09^{+1.55}_{-1.41}$	-	-	$53.45 \pm 2.12$	$56.18 \pm 2.85$
$5.63^{+2.21}_{-1.83}$	-	-	$1.05 \pm 0.06$	$1.56 \pm 0.12$

Table B.8: ....

$E_d$ (MeV)	Production cross section (mb) for ...				
	$^{48}\text{V}_{\text{cum}}$	$^{51}\text{Cr}_{\text{cum}}$	$^{52}\text{Mn}_{\text{cum}}$	$^{54}\text{Mn}_{\text{ind}}$	$^{53}\text{Fe}_{\text{cum}}$
$29.57^{+0.68}_{-0.68}$	$0.12 \pm 0.01$	$7.54 \pm 0.23$	$16.00 \pm 0.36$	$23.85 \pm 0.70$	$5.12 \pm 0.65$
$27.26^{+0.73}_{-0.72}$	$0.09 \pm 0.01$	$7.86 \pm 0.25$	$5.48 \pm 0.16$	$24.18 \pm 0.72$	$2.77 \pm 0.44$
$24.80^{+0.77}_{-0.76}$	$0.06 \pm 0.00$	$8.51 \pm 0.29$	$0.91 \pm 0.03$	$26.12 \pm 0.79$	$1.29 \pm 0.30$

Table B.9: ....

$E_d$ (MeV)	Production cross section (mb) for ...			
	$^{59}\text{Fe}_{\text{ind}}$	$^{55}\text{Co}_{\text{ind}}$	$^{57}\text{Co}_{\text{ind}}$	$^{58}\text{Co}_{\text{ind}}$
$0.16 \pm 0.02$	$27.15 \pm 0.80$	$35.91 \pm 1.06$	$1.50 \pm 0.05$	$29.57^{+0.68}_{-0.68}$
$27.26^{+0.73}_{-0.72}$	$0.15 \pm 0.02$	$20.44 \pm 0.60$	$38.37 \pm 1.13$	$1.62 \pm 0.05$
$24.80^{+0.77}_{-0.76}$	$0.18 \pm 0.04$	$13.82 \pm 0.40$	$42.63 \pm 1.27$	$2.05 \pm 0.07$

Table B.10: ....

$E_d$ (MeV)	Production cross section (mb) for ...					
	$^{59}\text{Fe}_{\text{cum}}$	$^{60}\text{Co}_{\text{cum}}$	$^{61}\text{Co}_{\text{cum}}$	$^{65}\text{Ni}_{\text{ind}}$	$^{61}\text{Cu}_{\text{cum}}$	$^{64}\text{Cu}_{\text{ind}}$
$30.03^{+0.67}_{-0.67}$	$0.21 \pm 0.03$	$9.49 \pm 0.52$	$1.62 \pm 0.09$	$3.42 \pm 1.76$	$4.54 \pm 0.87$	$170.76 \pm 7.76$
$27.74^{+0.72}_{-0.71}$	$0.18 \pm 0.02$	$11.38 \pm 0.51$	$0.82 \pm 0.07$	$3.84 \pm 1.94$	$2.07 \pm 0.95$	$153.78 \pm 8.20$
$25.32^{+0.77}_{-0.76}$	$0.17 \pm 0.02$	$12.02 \pm 0.51$	$0.29 \pm 0.05$	$2.89 \pm 1.48$	$1.18 \text{ pm } 0.72$	$132.56 \pm 6.93$
$22.77^{+0.83}_{-0.81}$	$0.12 \pm 0.01$	$11.36 \pm 0.43$	-	$1.92 \pm 1.14$	-	$121.54 \pm 7.12$
$20.57^{+0.89}_{-0.87}$	$0.07 \pm 0.01$	$9.27 \pm 0.41$	-	-	-	$106.07 \pm 5.81$
$18.14^{+0.97}_{-0.94}$	$0.03 \pm 0.01$	$5.65 \pm 0.26$	-	$1.46 \pm 0.95$	-	$95.92 \pm 7.14$
$15.43^{+1.08}_{-1.04}$	-	$1.53 \pm 0.12$	-	-	-	$123.79 \pm 6.62$
$12.34^{+1.27}_{-1.20}$	-	-	-	-	-	$156.65 \pm 8.20$
$8.68^{+1.62}_{-1.43}$	-	-	-	-	-	$209.38 \pm 11.27$
$3.94^{+2.25}_{-2.22}$	-	-	-	-	-	$73.54 \pm 5.70$

# Bibliography

- [1] Attila Vértes, Sándor Nagy, Zoltán Klencsár, Rezső G. Lovas, and Frank Rösch, editors. *Handbook of Nuclear Chemistry*. Springer US, Boston, MA, second edi edition, 2011.
- [2] Chai-Hong Yeong, Mu-hua Cheng, and Kwan-Hoong Ng. Therapeutic radionuclides in nuclear medicine: current and future prospects. *Journal of Zhejiang University SCIENCE B*, 15(10):845–863, oct 2014.
- [3] R. Qaim, S. M., TÁrkányi, F, Capote, editor. *Nuclear Data for the Production of Therapeutic Radionuclides*. Number 473 in Technical Reports Series. INTERNATIONAL ATOMIC ENERGY AGENCY, Vienna, 2011.
- [4] Shankar Vallabhajosula. *Molecular Imaging*. Springer Berlin Heidelberg, Berlin, Heidelberg, 2009.
- [5] Hannah. L. O. Ekeberg. Medical Radionuclides for Therapy and Diagnosis. Technical report, University of Oslo, Oslo, 2020.
- [6] Jyothi Thundimadathil. Cancer Treatment Using Peptides: Current Therapies and Future Prospects. *Journal of Amino Acids*, 2012:1–13, 2012.
- [7] Frank Rösch, Hans Herzog, and Syed Qaim. The Beginning and Development of the Theranostic Approach in Nuclear Medicine, as Exemplified by the Radionuclide Pair  $^{86}\text{Y}$  and  $^{90}\text{Y}$ . *Pharmaceuticals*, 10(4):56, jun 2017.
- [8] Michael Douglass. Eric J. Hall and Amato J. Giaccia: Radiobiology for the radiologist. *Australasian Physical & Engineering Sciences in Medicine*, 41(4):1129–1130, dec 2018.
- [9] David and others Krane, Kenneth, S., Halliday. *Introductory Nuclear Physics*. John Wiley & Sons, 1987.
- [10] William R. Leo. *Techniques for Nuclear and Particle Physics Experiments*. Springer Berlin Heidelberg, Berlin, Heidelberg, 1994.
- [11] M. Alotiby. *Accurately determining the number of Auger electrons per nuclear decay for medical isotopes*. PhD thesis, Australian National University, 2019.
- [12] C. Hillyar. *Auger electron radionuclide therapy utilising F3 peptide to target the nucleolus*. PhD thesis, University of Oxford, 2015.
- [13] Jean-Pierre Pouget, Isabelle Navarro-Teulon, Manuel Bardès, Nicolas Chouin, Guillaume Cartron, André Pèlegrin, and David Azria. Clinical radioimmunotherapy—the role of radiobiology. *Nature Reviews Clinical Oncology*, 8(12):720–734, dec 2011.
- [14] Marco Cianchetti and Maurizio Amichetti. Sinonasal Malignancies and Charged Particle Radiation Treatment: A Systematic Literature Review. *International Journal of Otolaryngology*, 2012:1–15, 2012.
- [15] Syed M. Qaim. Nuclear data for production and medical application of radionuclides: Present status and future needs. *Nuclear Medicine and Biology*, 44:31–49, jan 2017.

## BIBLIOGRAPHY

---

- [16] M. Shamsuzzoha Basunia. Nuclear Data Sheets for A=193. *Nuclear Data Sheets*, 143:1–381, jul 2017.
- [17] F. Tárkányi, B. Király, F. Ditrói, S. Takács, J. Csikai, A. Hermanne, M. S. Uddin, M. Hagiwara, M. Baba, Yu N. Shubin, and S. F. Kovalev. Cross sections of deuteron induced nuclear reactions on iridium. *Nuclear Instruments and Methods in Physics Research, Section B: Beam Interactions with Materials and Atoms*, 247(2):210–216, 2006.
- [18] Johan Areberg, Kristina Norrgren, and Sören Mattsson. Absorbed doses to patients from 191Pt-, 193mPt- and 195mPt-cisplatin. *Applied Radiation and Isotopes*, 51(5):581–586, nov 1999.
- [19] Dandamudi V. Howell, Roger W., Sastry, Kandula, S. R., Hill, Helene Z., Rao. CIS-PLATINUM-193m: Its microdosimetry and potential for chemo-auger combination therapy of cancer. In Evelyn E. Schlafke-Stelson, Audrey T., Watson, editor, *Fourth International Radiopharmaceutical Dosimetry Symposium*. Oak Ridge, Tennessee, 4 edition, 1985.
- [20] Viktor Vrapcenjak, Lidija, Zerkin. NuDat 2.8, 2015.
- [21] Roger W. Howell. Radiation spectra for Auger-electron emitting radionuclides: Report No. 2 of AAPM Nuclear Medicine Task Group No. 6. *Medical Physics*, 19(6):1371–1383, nov 1992.
- [22] Roger W. Howell, Dandamudi V. Rao, De-Yan Hou, Venkat R. Narra, and Kandula S. R. Sastry. The Question of Relative Biological Effectiveness and Quality Factor for Auger Emitters Incorporated into Proliferating Mammalian Cells. *Radiation Research*, 128(3):282, dec 1991.
- [23] K. Hilgers, H. H. Coenen, and S. M. Qaim. Production of the therapeutic radionuclides 193mPt and 195mPt with high specific activity via  $\alpha$ -particle-induced reactions on 192Os. *Applied Radiation and Isotopes*, 66(4):545–551, 2008.
- [24] A.S. Voyles, M.S. Basunia, J.C. Batchelder, J.D. Bauer, T.A. Becker, L.A. Bernstein, E.F. Matthews, P.R. Renne, D. Rutte, M.A. Unzueta, and K.A. van Bibber. Measurement of the 64Zn,47Ti(n,p) cross sections using a DD neutron generator for medical isotope studies. *Nuclear Instruments and Methods in Physics Research Section B: Beam Interactions with Materials and Atoms*, 410:230–239, nov 2017.
- [25] F. Tárkányi, A. Hermanne, F. Ditrói, S. Takács, and A.V. Ignatyuk. Measurement of activation cross sections of deuteron induced reactions on natIr in the 17–50 MeV energy range. *Nuclear Instruments and Methods in Physics Research Section B: Beam Interactions with Materials and Atoms*, 458:105–117, nov 2019.
- [26] Adisorn Ratanaphan. A DNA Repair Protein BRCA1 as a Potentially Molecular Target for the Anticancer Platinum Drug Cisplatin. In *DNA Repair*. InTech, nov 2011.
- [27] J. M. Koning, A. J., Akkermans. Pre-equilibrium nuclear reactions: An introduction to classical and quantum-mechanical models. 1999.
- [28] By Prof, Niels Bohr, and For Mem R S. Neutron capture and nuclear constitution [1]. *Niels Bohr Collected Works*, 9(C):151–156, 1986.
- [29] Antonio Moro. Models for nuclear reactions with weakly-bound systems. 2018.
- [30] IAEA. Cyclotron produced Radionuclides: Physical characteristics and production methods. *Technical Reports series*, 468, 2009.
- [31] J. Ongena. Fusion: a true challenge for an enormous reward. *EPJ Web of Conferences*, 189:00015, oct 2018.

- [32] Stephen A. Graves, Paul A. Ellison, Todd E. Barnhart, Hector F. Valdovinos, Eva R. Birnbaum, Francois M. Nortier, Robert J. Nickles, and Jonathan W. Engle. Nuclear excitation functions of proton-induced reactions ( $E_p = 35\text{--}90$  MeV) from Fe, Cu, and Al. *Nuclear Instruments and Methods in Physics Research Section B: Beam Interactions with Materials and Atoms*, 386:44–53, nov 2016.
- [33] Andrew S. Voyles, Amanda M. Lewis, Jonathan T. Morrell, M. Shamsuzzoha Basunia, Lee A. Bernstein, Jonathan W. Engle, Stephen A. Graves, and Eric F. Matthews. Proton-induced reactions on Fe, Cu, & Ti from threshold to 55 MeV. pages 1–25, 2019.
- [34] Jonathan T. Morrell, Andrew S. Voyles, M. S. Basunia, Jon C. Batchelder, Eric F. Matthews, and Lee A. Bernstein. Measurement of  $^{139}\text{La}(p,x)$  cross sections from 35–60 MeV by stacked-target activation. *European Physical Journal A*, 56(1), 2020.
- [35] Andrew S. Voyles, Lee A. Bernstein, Eva R. Birnbaum, Jonathan W. Engle, Stephen A. Graves, Toshihiko Kawano, Amanda M. Lewis, and Francois M. Nortier. Excitation functions for  $(p,x)$  reactions of niobium in the energy range of  $E_p = 40\text{--}90$  MeV. *Nuclear Instruments and Methods in Physics Research Section B: Beam Interactions with Materials and Atoms*, 429:53–74, aug 2018.
- [36] A. Hermanne, A.V. Ignatyuk, R. Capote, B.V. Carlson, J.W. Engle, M.A. Kellett, T. Kibédi, G. Kim, F.G. Kondev, M. Hussain, O. Lebeda, A. Luca, Y. Nagai, H. Naik, A.L. Nichols, F.M. Nortier, S.V. Suryanarayana, S. Takács, F.T. Tárkányi, and M. Verpelli. Reference Cross Sections for Charged-particle Monitor Reactions. *Nuclear Data Sheets*, 148:338–382, feb 2018.
- [37] Pop O.M., Simulik V.M. and Stets M.V. Nuclide Spectra of Activities of Thorium, Uranium Series and Application in Gamma-spectroscopy of Point Technogenic Samples. *International Journal of Physics*, 2016, Vol. 4, No. 2, 37-42, 2016.
- [38] T. Morell, J. NPAT: Nuclear Physics Analysis Tool, 2019.
- [39] J. F. Ziegler. Stopping of energetic light ions in elemental matter. *Journal of Applied Physics*, 85(3):1249–1272, feb 1999.
- [40] M. Kireeff Covo, R. A. Albright, B. F. Ninemire, M. B. Johnson, A. Hodgkinson, T. Loew, J. Y. Benitez, D. S. Todd, D. Z. Xie, T. Perry, L. Phair, L. A. Bernstein, J. Bevins, J. A. Brown, B. L. Goldblum, M. Harasty, K. P. Harrig, T. A. Laplace, E. F. Matthews, A. Bushmaker, D. Walker, V. Oklejas, A. R. Hopkins, D. L. Bleuel, J. Chen, and S. B. Cronin. The 88-Inch Cyclotron: A one-stop facility for electronics radiation and detector testing. *Measurement: Journal of the International Measurement Confederation*, 127:580–587, 2018.
- [41] Berkeley lab - About the lab.
- [42] 88-Inch Cyclotron.
- [43] I Y Lee, M A Deleplanque, and K Vetter. Developments in large gamma-ray detector arrays. *Reports on Progress in Physics*, 66(7):1095–1144, jul 2003.
- [44] Gilmore Gilmore Spectrometry, Practical Gamma-ray and Edition Gordon. *Practical Gamma-ray Spectrometry Practical Gamma-ray Spectrometry 2nd Edition*. 2008.
- [45] J. Fitzgerald. FitzPeaks gamma analysis and calibration software. 2009.
- [46] Markku J. Koskelo, Pertti A. Aarnio, and Jorma T. Routti. SAMPO80: An accurate gamma spectrum analysis method for minicomputers. *Nuclear Instruments and Methods in Physics Research*, 190(1):89–99, nov 1981.
- [47] E. Browne and J.K. Tuli. Nuclear Data Sheets for  $A = 137$ . *Nuclear Data Sheets*, 108(10):2173–2318, oct 2007.

## BIBLIOGRAPHY

---

- [48] Yu. Khazov, A. Rodionov, and F.G. Kondev. Nuclear Data Sheets for  $A = 133$ . *Nuclear Data Sheets*, 112(4):855–1113, apr 2011.
- [49] M.J. Martin. Nuclear Data Sheets for  $A = 152$ . *Nuclear Data Sheets*, 114(11):1497–1847, nov 2013.
- [50] William J. Gallagher and Sam J. Cipolla. A model-based efficiency calibration of a Si(Li) detector in the energy region from 3 to 140 keV. *Nuclear Instruments and Methods*, 122:405–414, nov 1974.
- [51] Lee A. Matthews, Eric F., Lewis, Amanda M., Bernstein. Significance of gamma-ray detector efficiency calibration bias on nuclear astrophysics and nuclear data evaluations. 2020.
- [52] Pauli Virtanen, Ralf Gommers, Travis E. Oliphant, Matt Haberland, Tyler Reddy, David Cournapeau, Evgeni Burovski, Pearu Peterson, Warren Weckesser, Jonathan Bright, Stéfan J. van der Walt, Matthew Brett, Joshua Wilson, K. Jarrod Millman, Nikolay Mayorov, Andrew R. J. Nelson, Eric Jones, Robert Kern, Eric Larson, C J Carey, İlhan Polat, Yu Feng, Eric W. Moore, Jake VanderPlas, Denis Laxalde, Josef Perktold, Robert Cimrman, Ian Henriksen, E. A. Quintero, Charles R. Harris, Anne M. Archibald, Antônio H. Ribeiro, Fabian Pedregosa, and Paul van Mulbregt. SciPy 1.0: fundamental algorithms for scientific computing in Python. *Nature Methods*, 17(3):261–272, mar 2020.
- [53] Coral M. Baglin. Nuclear Data Sheets for  $A = 192$ . *Nuclear Data Sheets*, 113(8-9):1871–2111, aug 2012.
- [54] BAI ERJUN and HUO JUNDE. Nuclear Data Sheets for  $A = 63$ . *Nuclear Data Sheets*, 92(1):147–252, jan 2001.
- [55] Kazimierz Zuber and Balraj Singh. Nuclear Data Sheets for  $A = 61$ . *Nuclear Data Sheets*, 125:1–200, mar 2015.
- [56] Alan L. Nichols, Balraj Singh, and Jagdish K. Tuli. Nuclear Data Sheets for  $A = 62$ . *Nuclear Data Sheets*, 113(4):973–1114, apr 2012.
- [57] Wayne Rasband. ImageJ 1.52K, 2010.
- [58] Brookhaven National Laboratory Pritychenko, B., Sonzogni, A., NNDC. Q-value Calculator (Q-calc).
- [59] M.J. Berger, J.H. Hubbell, S.M. Seltzer, J. Chang, J.S. Coursey, R. Sukumar, D.S. Zucker and K. Olsen. XCOM: Photon Cross Sections Database, 2010.
- [60] Huo Junde, Huo Su, and Yang Dong. Nuclear Data Sheets for  $A = 56$ . *Nuclear Data Sheets*, 112(6):1513–1645, jun 2011.
- [61] Caroline D. Nesaraja, Scott D. Geraedts, and Balraj Singh. Nuclear Data Sheets for  $A = 58$ . *Nuclear Data Sheets*, 111(4):897–1092, apr 2010.
- [62] E. Browne and J.K. Tuli. Nuclear Data Sheets for  $A = 65$ . *Nuclear Data Sheets*, 111(9):2425–2553, sep 2010.
- [63] Anders Bäcklin. *Treatise on Heavy-Ion Science*, volume 252. 1986.
- [64] M. Blann. New precompound decay model. *Physical Review C*, 54(3):1341–1349, sep 1996.